Operation of Offshore HVDC Systems with Grid-Forming Wind Turbines in System Energization and DC-Fault Scenarios

Von der Fakultät für Elektrotechnik und Informationstechnik der
Rheinisch-Westfälischen Technischen Hochschule Aachen
zur Erlangung des akademischen Grades eines
Doktors der Ingenieurwissenschaften
genehmigte Dissertation

vorgelegt von

Christopher Klein, M. Sc.
aus Troisdorf

Berichter: Univ.-Prof. Dr. Ir. Willem Leterme
Prof. Nicolaos A. Cutululis, Ph. D.

Tag der mündlichen Prüfung: 19.12.2025

Diese Dissertation ist auf den Internetseiten der Universitätsbibliothek online verfügbar.

Acknowledgment

This work was created during my time as a research associate at the Institute for High Voltage Equipment and Grids, Digitalization, and Energy Economics at RWTH Aachen University.

My special thanks to Univ.-Prof. Dr.-ir. Willem Leterme, who made this work possible. His trust in me, together with his constant support, encouragement, and invaluable advice, has contributed significantly to the success of this dissertation.

I would also like to thank Prof. Dr.-Ing. Nicolaos Cutululis for kindly serving as co-supervisor and for his strong interest in the topic.

My sincere thanks go to my colleagues at the institute for their collaboration and continuous support. I am especially grateful to both current and former members of the DC-Systems team for the many technical discussions that greatly contributed to the development of this work.

I also wish to acknowledge the contributions of the students who supported me through their bachelors and masters theses, as well as their work as student research assistants.

Special thanks go to my family for their support and encouragement throughout my studies.

Finally, I am deeply grateful to my girlfriend, Maria, for her patience, understanding, and emotional support during the preparation of this dissertation.

Christopher Klein,

December 2025

Abstract

The European Union foresees an installed capacity of offshore wind power of 300 GW by 2050, with 70 GW planned by Germany in the North Sea. Due to the long distances from shore, offshore wind power plant (OWPP) are generally connected via point-to-point high voltage direct current (HVDC) systems to increase efficiency of power transmission power to shore.

Given these large amounts of power, and due to the reduction in conventional power plants, OWPP have been considered for the provision of system services. In particular, OWPP could provide black-start and power system restoration services following a power system black- or brown-out. However, for an HVDC-connected OWPP to be black start capable, a paradigm shift in the control design is necessary. Current grid-following wind turbine generator (WTG) control relies upon the voltage and frequency provided by the offshore HVDC converter. To eliminate this requirement, the control of the WTG can be adapted providing their own voltage and frequency.

Further in the future, multi terminal HVDC (MTDC) systems, interconnecting multiple wind farms through multiple DC links are considered to increase redundancy and availability. To reduce the maximum loss of power, these system are planned to be protected via DC circuit breaker (DCCB). For current system requirements, it is mandatory that far fault converters do not protectively block due to overcurrent. This is mainly driven by the aspect that, as previously described, the OWPP is dependent on the offshore converter. If the WTG control were adapted and designed for black start capability, temporary converter blocking could reduce protection requirements.

This thesis contributes to a holistic understanding of using grid forming wind turbine generator (GFM WTG) in future offshore HVDC systems for different system scenarios, mainly black start and DC-side fault behavior.

First, a detailed analysis on functional and technical requirements during the start-up of an OWPP connected via an HVDC system is presented.

The required active and reactive power during the start-up process, as well as the control interactions between the WTG converters and the HVDC converter, along with the overall black start capability of the system are analyzed and evaluated. A key outcome of the investigation is that the design parameters such as the number of submodules of the HVDC converters, voltage levels at AC and DC side, and wind park design have a significant impact on the black start process and need to be considered in the design phase.

Second, benefits and requirements are analyzed, when black-start capable WTG partially reenergize the HVDC system after a DC-side fault. In a partially selective protected MTDC system, the faulted part of the system is isolated, resulting in a discharge of that system part and a disconnection of the OWPP from the HVDC converter by opening the AC circuit breaker. After maintaining a stable island, the OWPP can then reenergize the HVDC after reclosing the AC circuit breaker. A key take away is that the recovery process crucially depends on the remaining submodule charge and HVDC system post-fault topology.

Third, potential to reduce DC-side protection requirements through temporary blocking of the offshore converter in combination with various control strategy combinations is analyzed. After fault occurrence, the offshore converter protectively blocks its submodules temporarily. It is demonstrated that irrespective of the control architecture of the HVDC system, the OWPP can be disconnected and reconnected to the HVDC system while the overall system integrity is maintained. A key take away is that the required DC-side inductance can be significantly reduced compared to the state-of-the art protection designs while fulfilling fault-ride-through requirements on the offshore AC and DC side.

Lastly, it is shown that GFM WTGs are capable of flexibly adapting the load flow of the connected HVDC system avoiding DC-side overvoltages after DC-side faults.

Overall, the findings from this thesis show that GFM WTGs can increase operational flexibility of future OWPPs, while maintaining system integrity. During normal operation, active power provision is identical to the state-of-the-art, while maintaining the ability to quickly adapt to system changes and fault scenarios.

Contents

1 Introduction **1**
1.1 Motivation of the topic 3
1.2 Research context 6
1.2.1 Grid-forming WTGs with HVDC systems 6
1.2.2 Offshore HVDC architectures and topologies . . 8
1.2.3 Protection philosophies for HVDC systems . . . 11
1.2.4 Research questions and thesis structure 14

2 Technological background **19**
2.1 HVDC-connected wind power plants 19
2.1.1 Offshore system design 19
2.1.2 Type-4 wind turbine generator 20
2.1.3 Modular Multilevel Converter 22
2.2 Converter controls 28
2.2.1 Grid-following control 28
2.2.2 Grid-forming control 30
2.3 Energization of an offshore HVDC system 33
2.3.1 System energization 33
2.3.2 Hard energization 33
2.3.3 Soft energization 34
2.3.4 Energization of the MMC 34
2.4 Faults in HVDC systems 37

3 Component and system models **39**
3.1 Offshore wind power plant model 39
3.1.1 Wind turbine generator model 40
3.1.2 WTG control 42
3.2 HVDC System 45
3.2.1 MMC control 49
3.2.2 HVDC protection 49
3.3 Cable modeling 51

4 OWPP and HVDC system energization 53
4.1 Start-up methodologies 53
4.1.1 Energization of the first WTG 54
4.1.2 Offshore wind power plant energization 55
4.1.3 HVDC system energization 57
4.2 Results - Hard energization 60
4.2.1 Energization of the offshore wind power plant . . 60
4.2.2 Energization of the HVDC System 64
4.2.3 Onshore load connection 68
4.2.4 Synchronization to a pre-established AC System 70
4.3 Results - Soft energization 73
4.4 Technical requirements and sensitivity analysis 74
4.4.1 Hard vs soft energization 75
4.4.2 Black start requirement for WTGs 76
4.4.3 Requirement on system design and modeling . . 77
4.4.4 Voltage and frequency stability 78
4.4.5 Onshore grid synchronization 78
4.4.6 Required interfaces/ communication 79
4.4.7 Black start availability 80
4.4.8 General discussion on WTG requirements 81
4.5 Conclusion 82

5 Post DC-side fault HVDC system energization 83
5.1 Fault clearing and energization methodology 83
5.1.1 Fault isolation 83
5.1.2 Converter energization 84
5.1.3 System energization 86
5.1.4 Evaluation criteria 87
5.1.5 Offshore MMC re-energization 88
5.2 Analysis of the different scenarios 91
5.2.1 Fault isolation 91
5.2.2 Offshore MMC re-energization 91
5.2.3 Results for fault on L2-4 94
5.2.4 Results for Fault on L1-2 96
5.3 Conclusion 99

6 Temporary converter blocking during DC-side fault clearing . . . 101
6.1 Fault clearing methodology . . . 102
6.1.1 Dimensioning of the DC reactor . . . 102
6.1.2 Control scenarios . . . 102
6.1.3 Temporary blocking sequence . . . 105
6.1.4 Evaluation criteria . . . 106
6.2 Protection implementation . . . 110
6.2.1 Adaption to MMC control . . . 110
6.3 EMT-Studies of the different FRT-Scenarios . . . 111
6.3.1 System behavior of DC-FRT 1 . . . 112
6.3.2 Analysis of DC-FRT 2 . . . 112
6.3.3 Analysis of DC-FRT 3 . . . 114
6.3.4 Analysis of DC-FRT 4 . . . 114
6.3.5 Discussion . . . 117
6.4 Conclusion . . . 120

7 Post DC-side fault load flow control via GFM WTGs 121
7.1 Control strategy . . . 121
7.2 Post DC-side fault power flow . . . 122
7.2.1 Strong AC-grid . . . 124
7.2.2 Block load without curtailment . . . 126
7.2.3 Block load with curtailment . . . 128
7.3 Conclusion . . . 131

8 Conclusion and Outlook . . . 133
8.1 Contributions and conclusions . . . 133
8.2 Future research needs . . . 136

Bibliography . . . 139

Glossaries . . . 151
List of acronyms . . . 151
List of symbols . . . 152

List of Figures . . . 163

List of Tables . . . 169

List of publications **171**

Curriculum Vitae **173**

List of supervised theses **175**

Appendix **177**
A.1 DC cable 177
A.2 AC cable 179
A.2.1 Cable aggregation 180
A.3 WTG control parameters 181
A.4 MMC control parameters 182
A.5 Transformer parameters 183
A.6 Onshore grid parameters 184

1 Introduction

To achieve decarbonized society and meet the goals set with the 2015 Paris Agreement, the electric system is undergoing major changes [Uni18]. New-generation technologies, including solar photovoltaic and wind power, are being widely deployed to replace conventional coal and nuclear power plants. One large part of the installed and planned integration of renewable energy source (RES) in the European Union (EU) are offshore wind power plants (OWPPs). The installed capacity in the North Sea within the EU was around 20 GW in 2023 [Eur25, ENT24]. The prospective planning, including Norway and the United Kingdom, foresees an installed capacity of 300 GW by 2050 [Win19, ENT24]. In Germany, integration is primarily planned in the North Sea, with 30 GW of installed capacity in 2020 and a projected capacity of 70 GW by 2050 (cf. Figure 1.1) [Win19, Übe24, Eur24].

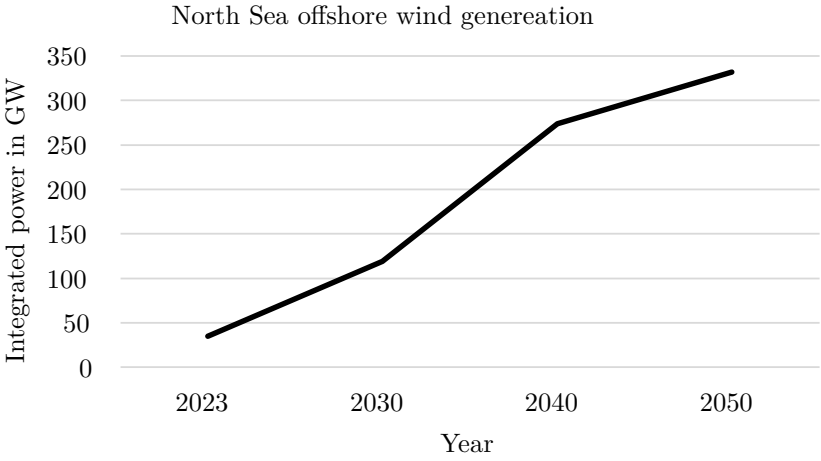


Figure 1.1: Development of the installed capacities in the North Sea [ENT24]

This massive integration of OWPPs in the North Sea is planned at distances far from shore. Over these long connection distances, AC connection is not feasible due to the cable losses. The break even distance

compared to high voltage direct current (HVDC) is generally estimated to be up to 100 kilometers [CSC22]. Therefore, HVDC is currently the connection technology for German OWPPs, since it becomes the more techno-economical connection solution [BMW25].

The OWPP design and connection to the HVDC system are influenced by multiple factors such as wind turbine generator (WTG) size, the proximity of the WTG and HVDC converter, and the maximum number of WTG per cable string. One prominent connection solution is a 33/150 kV intermediate voltage connection, where the 33 kV is used for interconnecting the WTGs and 150 kV for the connection to the converter. Windparks such as BARD Offshore 1, Nordsee One, Global Tech 1, which are connecteded to BorWin 1-3, DolWin 1-3 and HelWin 1 and 2 make use of the 33/155 kV connection [Cig15, BRM15]. A newer connection solution uses 66 kV, where the WTG and the offshore converter are connected directly. DolWin Epsilon is the first HVDC system with this connection type [Gmb24]. In the EU, HVDC systems are based on voltage source converters (VSCs), which allow for flexible power transmission. Furthermore, compared to older technologies such as the line-commutated converter (LCC), VSCs are capable of providing active and reactive power independently enabling VSCs to operate in weaker AC grids. Additionally, LCCs require a voltage source to function, whereas VSCs can operate independently, making it a possible black start unit [SHN16, vGL16]. For OWPP, the HVDC connection is traditionally built as symmetrical monopole point-to-point link, since it is a cost-efficient solution to bring wind power to shore [SHN16].

Point-to-point connections have the advantage of low control and design requirements, since their primary operating mode is unidirectional power transfer. However, a DC-side cable fault results in long system downtime due to cable repairs. During these outages, no power transfer is possible, and the WTGs have to be curtailed. As a suitable alternative to the symmetrical monopole, the bipole with dedicated metallic return (DMR) was introduced and set as a new standard for future offshore connections [AK22], (Figure 1.1, right). The bipole essentially consists of two monopoles a third cable providing the return path. Therefore, the bipole offers double the transmission capacity while requiring only one additional cable [DKW24]. In the future, point-to-point links are foreseen to be interconnected to multi terminal HVDC (MTDC) systems.

This will further increases redundancy and system flexibility, such as redispatch or demand based power transfer [Nor25]. The first VSC based MTDC system in Europe was the Caithness-Moray Link in the UK [Ene19].

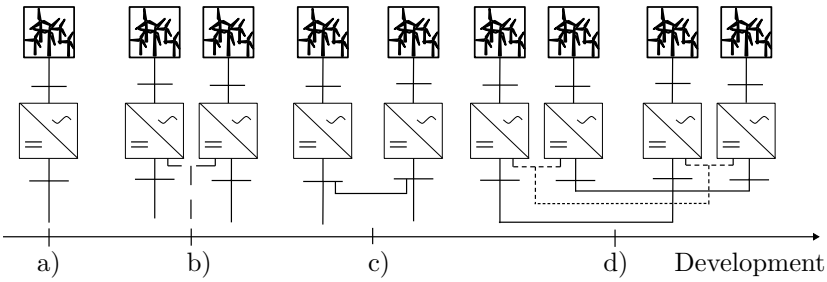


Figure 1.2: Sketch of the development of HVDC systems

The previously discussed large-scale introduction of RESs increases the share of converter-based resources, potentially affecting the stability of the onshore AC transmission grid. Additionally, the decommissioning of conventional power plants and the associated reduction of rotating masses further accelerate this process. Traditional converter controls, also known as grid following (GFL) control, rely on a voltage and frequency reference provided by the grid. The aim of the control is to inject the maximum available power into the grid. As a result, the combination of reduction in network strength and an increased converter share could lead to instabilities, stronger control interactions, and potential blackouts of the AC grid. Therefore, as of 2023, all converter-connected energy resources are required to be capable of providing grid-supporting functions in accordance with VDE 4131 [VDE19], which also applies to HVDC-connected OWPP.

1.1 Motivation of the topic

Achieving the aforementioned grid-stabilizing behavior for today's offshore HVDC systems requires significant control changes of either the HVDC system or the overall control chain, including the WTG controls within the OWPP. To achieve the envisioned AC-grid stabilizing

behavior, a transition from GFL to grid forming (GFM) converter controls (i.e., the provision of voltage and frequency reference) is required [VF20b, RLB12]. Currently, the HVDC system, specifically the offshore converter (cf. Figure 1.3, left) is required to provide the voltage and frequency reference for the OWPP since the grid-side converter of the WTGs are GFL controlled. This also requires the offshore AC system to be energized prior to starting up the WTGs. A control change for the WTGs from GFL to GFM controlled converters can be a viable solution, making the OWPP independent of the voltage and frequency provision of the HVDC system. Simultaneously, the onshore converter can provide GFM functions, fulfilling the system service requirements, leading to a control reversal compared with the state of the art (cf. Figure 1.3, right).

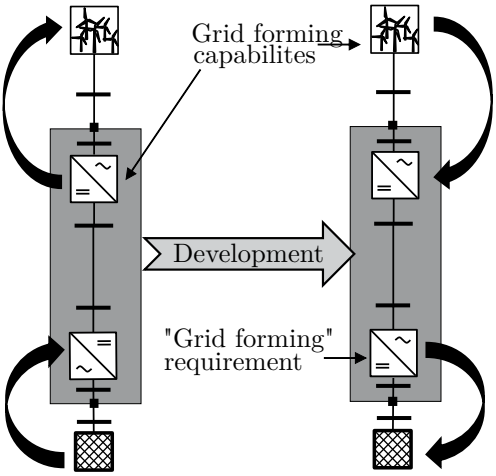


Figure 1.3: Change in controls needed to achieve operational flexibility of offshore HVDC system [Kle24]

With the control reversal, the WTGs are capable of islanding, enabling a reversal of the system's energization process. Currently, offshore systems are seen as power sinks during startup, requiring a stable AC grid connection for energization. With the reduction in AC system stability and higher fluctuation in power delivery, it is beneficial if the OWPP is capable of maintaining its system integrity without relying

on the voltage and frequency of the offshore converter or on the onshore system power supply. Especially in a black start scenario, the offshore system could either be started via the OWPP and reconnected to the onshore AC system at a specified grid strength or be used for full onshore system energization due to the large planned capacities. This prevents large OWPPs from having to be energized through an already weakened AC system. This usually requires an energization in the later stages of the black start restoration process [Gök17, JSS21a, PKH22]. Other control solutions in which both HVDC converters operate in GFM control have also been proposed [GSP22]. For interconnectors, this control approach allows for GFM provision in both connected countries and enables for black start services [RGS20]. However, for OWPPs it limits operational flexibility, since the WTGs remain dependent on the offshore converter and have no islanding or self start capabilities.

While black start services after an AC grid outage are a relevant use case for offshore systems, DC-side faults, after which reenergization is required, are much more common. Especially in bipolar or MTDC systems, fast reenergization can be beneficial since part of the system can remain in operation. As a first fault response, due to protective blocking of the converter and opening of the AC breaker, the OWPP has to maintain a stable island. Afterwards, the OWPP could aid in fast system recovery by reconnecting the converter by closing the AC breaker and reenergizing the HVDC system [SAL20]. This avoids a current issue that after DC-side faults and subsequent blocking of the converter, the WTGsmust shut down, leading to long outage times before restart.

For MTDC systems to keep the loss of infeed within permissible limits imposed by the AC system (e.g., 3 GW), selectivity at the DC-side is typically required [ENT16b, Eur17]. From a protection perspective, the most probable solution would be to install DC circuit breakers (DCCBs) on every DC line, enabling fast-fault clearing, while keeping all converters and the system, except for the faulty line, in operation. However, DCCBs are bulky components with large physical dimensions and heavy weight and are especially challenging to realize on offshore platforms. Additionally, an inductance is connected in series with the DCCB to reduce the rise of fault current [PRO17]. The size depends on two aspects, the fault-current interrupting capabilities of the DCCB

and maximum permissible rise of current inside the converters until fault clearing. The latter is usually the dimensioning aspect and can lead to large required DC reactor (DCR). However, smaller or fewer DCR are generally desired as DCR have a large impact on the DC-side control behavior, DC system stability and add to the weight and space requirements of the DCCB [DBK23, BRP20, LKD25]. With grid following wind turbine generator (GFL WTG), DCR sizing needs to ensure the continuous operation of the offshore converter, due to the dependency on a voltage and frequency reference. Converter blocking due to a fault inevitably leads to a shutdown of the OWPP and long restoration times [CEN18]. Changing to grid forming wind turbine generator (GFM WTG) could potentially allow the offshore converter to block, since the continuous operational requirement of the offshore converter does not need to be full filled. The GFM WTG could remain in islanded operation and after fault clearing reconnect with the deblocked offshore converter.

1.2 Research context

Based on the motivation, this thesis focuses on onshore AC grid energization through HVDC-connected wind farms and the benefits and requirements for using a GFM WTG control strategy in DC-side fault scenarios. To determine and evaluate the benefits of transitioning from state-of-the-art GFL WTG to GFM WTG, different system aspects need to be discussed. First, the recent developments in GFM converter controls are analyzed. Subsequently, the impact of the HVDC system architecture and protection design on the system operation is explored.

1.2.1 Grid-forming WTGs with HVDC systems

The prevalent converter control to provide the switching signals and voltage references for the converter is a GFL control in d/q coordinates. GFL-controlled converters require a stable voltage and frequency to connect to. Synchronization with the grid frequency is typically achieved via a phase-locked loop (PLL), which tracks the voltage phase angle [REL20, RWL21, RLB12]. The converter regulates voltage and injects

power by controlling its current. For an OWPP, the GFL control requires voltage provision from the offshore converter [SHN16, vGL16]. During loss of the offshore converter, for example through a DC-side fault, the OWPP would need to be shut down leading to long down and restart times. The onshore converter of the HVDC system is similarly dependent on the onshore grid strength for operation.

GFM control presents an alternative to GFL control. GFM-controlled converters do not need a PLL to synchronize with the grid but provide their own voltage and frequency, which are adapted to the system via the power difference and voltage setpoints. As a result, GFM can operate in weak grids [REL20, RWL21, UNS20]. Different GFM controls have been developed especially for microgrids. Prominent control strategies are the virtual synchronous machine (VSM) control, [DS13], the power synchronization control [ZHN10], a distributed PLL-based control [YLX18], and direct power control [NTK98].

In 2016, the ENTSO-E issued network codes for HVDC and DC-connected power park-modules, where the relevant transmission system operator can request black start and islanded operation from HVDC systems [ENT16a]. For HVDC-connected OWPP, this requires black start capable WTGs. In [JSC20, PBB20], the aforementioned GFM controls were tested for their conformity in black start and islanded operation. Both publications use simplified models to provide a general overview for each control type. [PBB20] investigates the controls within a direct AC connection, while [JSC20] investigates HVDC energization with WTG based on voltage sources and only a single transformer between the HVDC system and the OWPP. [SGB19], uses the older OWPP configuration in Figure 2.1, right but at 66 kV instead of 33 kV. It focuses on the energization of the HVDC and the OWPP is started prior to the investigation and the requirements for starting the OWPP itself are neglected. Offshore platforms have strict space and weight limitations, so adding extra equipment, such as a pre-insertion resistor (PIR) for transient mitigation, is typically avoided. Therefore, [JSS21a, JSS21b] explore alternative start-up methods to the prevalent hard-energization (i.e., interconnecting system parts at nominal voltage via breakers). [JSS21a] compares the hard-energization with the soft-energization (i.e. using a voltage ramp to energize the whole system). While it provides first insights on the advantages and disadvantages of each method, the

focus of the soft start lies mainly in the initial charging phase of the offshore converter, rather than in the full energization of the HVDC system. [JSS21b] provides an alternative solution of inserting a virtual resistance term into the control, which is suitable to mitigate the switching transients. Overall, the studies show the general black-start capability. However, due to the simplifications and adaptations, only a partial view (e.g. transients due to aggregation, effect on the WTG) is shown or underestimations in active and reactive power requirements are derived. Furthermore, the synchronization of the WTG during startup and the synchronization to an onshore system is generally neglected. This becomes especially more important with a 66 kV direct connection compared to connection with intermediate voltage step due to the energization of the two large three-winding transformers. Therefore, an in-depth analysis of the overall black start procedure for onshore grids through HVDC connected OWPP, with detailed electrical modeling is required, but presently lacking.

1.2.2 Offshore HVDC architectures and topologies

HVDC systems for offshore connections in point-to-point connections consist of two AC/DC converters (one offshore and one onshore) connected by a DC transmission line, executed as submarine cables [SHN16, vGL16]. HVDC systems are generally classified into two topologies, monopolar and bipolar. The monopolar topology is classified into two subcategories, the asymmetrical and symmetrical monopole. For offshore connections, so far, the symmetrical monopole was the connection of choice [BRM15] (Figure 1.4 b). It has the advantage, that while for both connections the system voltage is V_{DC}, the cable voltage is rated for $\frac{V_{\mathrm{DC}}}{2}$ compared to V_{DC} for the asymmetrical monopole. In light of cable developments, this allows for higher overvoltages increasing the operational freedom of the system (Figure 1.4 c). The bipolar topology essentially consists of two asymmetrical monopoles, where both halves of the system share one ground connection. The ground return can either be made with an extra cable (i.e., bipole with dedicated metallic return) or with direct grounding (i.e., rigid bipole) (Figure 1.4 d) [SHN16, vGL16]. The advantage of the bipolar topology compared to a monopole is, due to having four converters double the amount of power can be transferred, while only requiring two pole cables. In offshore

connections the bipole with DMR (leading to three cables in total for each connection) compared to the rigid bipole is preferred, avoiding a direct current return through earth but rather through the cable. In Germany, the 2 GW standard for offshore connections was introduced by TenneT TSO GmbH and is the basis for all future connections in the North Sea. The 2 GW standard essentially specifies that all future connections will be built as bipolar systems with DMR at 2 GW. Each pole will be connected to a 1 GW OWPP [Übe24, AK22]. While monopolar systems have to be shut down after a single-pole fault, bipolar systems can be operated at 50 % of the maximum power on the remaining pole cable, if the DMR is rated equal to the pole cables. For offshore wind connections this enables the use of 50 % of the available wind power after the fault. During wind conditions lower than 100 %, the system can benefit from an interconnection of the two poles of the HVDC system on the AC-side, coupling the two OWPP with both poles of the HVDC system (Figure 1.4 e) [DBT22]. This increases the transmissible power without curtailment of the WTG from 50 % to 75 % for a linear interconnected MTDC topology. As conceptually shown in [DBT22], the benefit of distributing the active power on the AC side. To enable the power transfer, a control adaptations of the HVDC converter is required. Ideally, an OWPP with GFM WTG could achieve the same post-fault states, that the converter with droop control can provide. However, the requirements and control adaptations have to be investigated.

Irrespective of the topology, different HVDC system architectures are possible. Point-to-point links offer the advantage of having a unidirectional power flow after start-up (OWPP to land), making system control simple, and reducing protection requirements. However, a DC-side fault inevitably causes a full system outage (except for the bipole with DMR), and for cable systems, leads to long downtime due to mandatory repair. As a result, point-to-point links are protected via circuit breakers on the AC side, since there is no speed requirement on the fault clearing. To increase redundancy, as well as allowing for efficient load transfer between two far points of onshore connection, point-to-point systems can be interconnected to MTDC systems. The smallest version of a MTDC system (in offshore connections) is a linear system, where the offshore converters of two point-to-point systems are connected via an additional DC transmission line connecting point-to-point 1 and point-to-point 2 (Figure 1.4a, dashed line). In case of a fault on an export connection

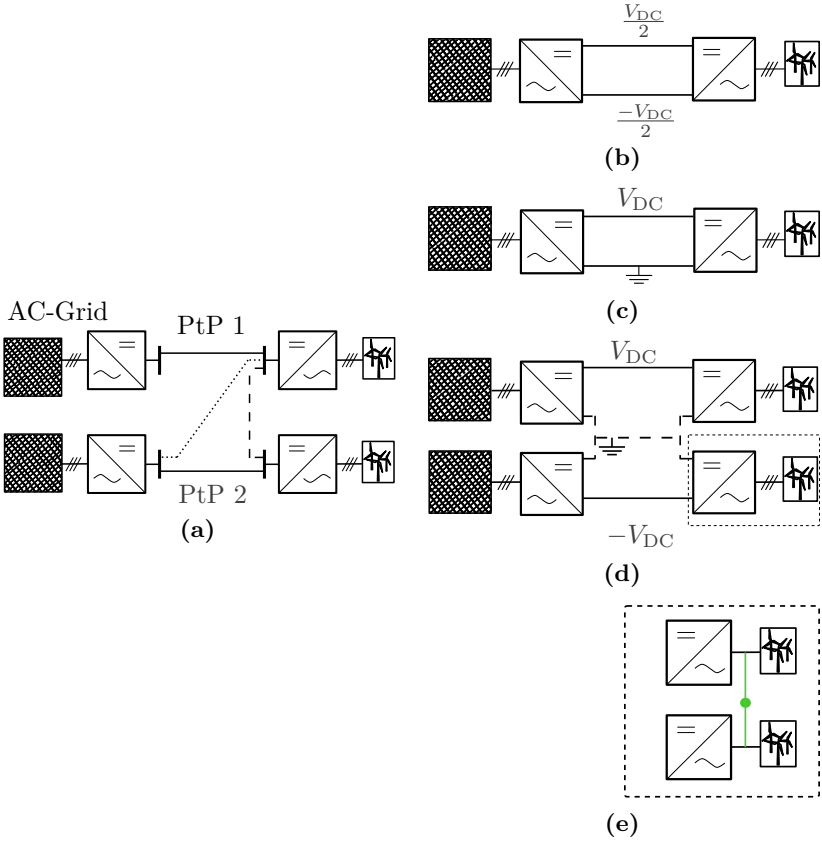


Figure 1.4: Overview of different HVDC architectures and topologies a) MTDC system, b) sym. monopole c) asym. monopol d) Bipol (DMR dashed) e) AC coupling

(offshore to onshore), the OWPP power can still be transferred via the second onshore converter as long as the offshore converter remains in operation. This is especially beneficial in low wind situations, when less than the maximum power is supplied. Each additional line leads to increased system requirements. When adding another additional line to a linear system it is referred to as a meshed system (Figure 1.4a, dotted line) [SHN16]. With every additional line, the control and protection

requirements increase and require additional analysis.

1.2.3 Protection philosophies for HVDC systems

A DC-side fault leads to a drop in DC voltage, leading to a current rise inside the connected converters. If the current rise is not limited, the converters are blocked to protect the submodules. After blocking, the converters are not actively controllable, resulting in a loss of active power transmission. In point-to-point links, the loss of transmission cable inventively leads to a system outage, regardless of the converter response. However, the aforementioned development from point-to-point links to MTDC systems for offshore connections, requires selectivity in DC-side protection to ensure security of supply. and avoid breach of the maximum permissible power outage [BKD21, AWT17, ENT16b].

To define the DC system impact on the AC point of connection during a DC-side fault, CENELEC CLC/TS 50654-1 classifies the behavior of the converter into permanent stop, temporary stop and continous operation [CEN18]. Permanent stop is defined by a full system outage and interruption of active power delivery by the HVDC system. This behavior is applicable to all point-to-point links. The duration of the outage is long enough that AC grid stability is potentially endangered and goes into alert, emergency or blackout state. A temporary stop describes interruptions of shorter duration, that are short enough, to prevent the AC system from going into the aforementioned states. For continous operation, only a transient response is permissible and protective converter blocking is not allowed.

For MTDC protection, there is yet no standard on how to fulfill the aforementioned requirements, but different protection philosophies were developed to mitigate the outages. Three different philosophies are distinguished, non-selective (cf. Figure 1.5a) , partially-selective (cf. Figure 1.5b) and fully-selective(cf. Figure 1.5c). Within an non-selective strategy, the whole HVDC system is one protection zone. Therefore, the whole HVDC system has to be shut down for fault isolation. This is done via the AC breaker at the converter terminals and the fault is separated via the disconnectors. From the AC point of coupling, this strategy is seen as permanent stop at all AC point-of-connections, and

can lead to severe AC instabilities especially for larger MTDC systems [CEN18] (cf. Figure 1.5a).

Alternatively, the use of full-bridge converters for fault clearing has been investigated [RCB19a]. It is classified as non-selective since the whole system is temporarily deenergized via the full-bridge converters to isolate the fault. However, the converters can bring the system back into operation within hundreds of milliseconds, causing only a temporary stop from an AC perspective. Since the system is temporarily deenergized, the OWPP requires GFM, to stay in operation during the interruption time. In [RCB19b] a mode switch from GFL to GFM-controlled WTG is proposed.

To limit the outage to a partial part of the MTDC system, a partially-selective or a fully-selective strategy were developed, which use breakers on the DC side [Lv15, DRB20] (cf. Figure 1.5b, 1.5c). For fully-selective, each line is protected by a DCCB. Therefore, the whole system only experiences a transient outage and overall remains in operation, with the faulty line being disconnected within milliseconds, depending on the detection time and the DCCB type (cf. Figure 1.5c). Investigated breaker technologies range from opening times of 2 ms for VSC Assisted Resonant Current DCCBs to 3 ms for hybrid DCCBs to 10 ms for mechanical DCCBs [Nor25, TRJ23].

Due to the high cost of having DCCBs on each line, partially-selective has been investigated as a suitable alternative. Especially in offshore connections based on the linear topology it is seen as a prominent solution to mitigate DC-side faults [Nor25, DBT22]. For partially-selective, the system is split into a healthy and faulty zone (cf. Figure 1.5b). For the faulty zone, the fault clearing is applied as it is in the non-selective strategy [PRO17, Cig19] leading to a permanent stop of that zone. The AC system impact for the healthy zone is currently required to be continous operation. This requires that the converter remains in operation and does not protectively block due to overcurrent in the submodules. To mitigate the overcurrent, a DCCB is combined with a series DCR to limit the rise of current until the DCCB can interrupt the fault [DBK23]. Depending on the DCCB type, cable lengths and converter overcurrent capabilities, an inductance of the DCR of hundreds of millihenries is common for setups like the linear MTDC system (cf. Figure 1.5c L_{BRK}) [DBK23, Nor25]. However, a large inductance of the DCR has an impact

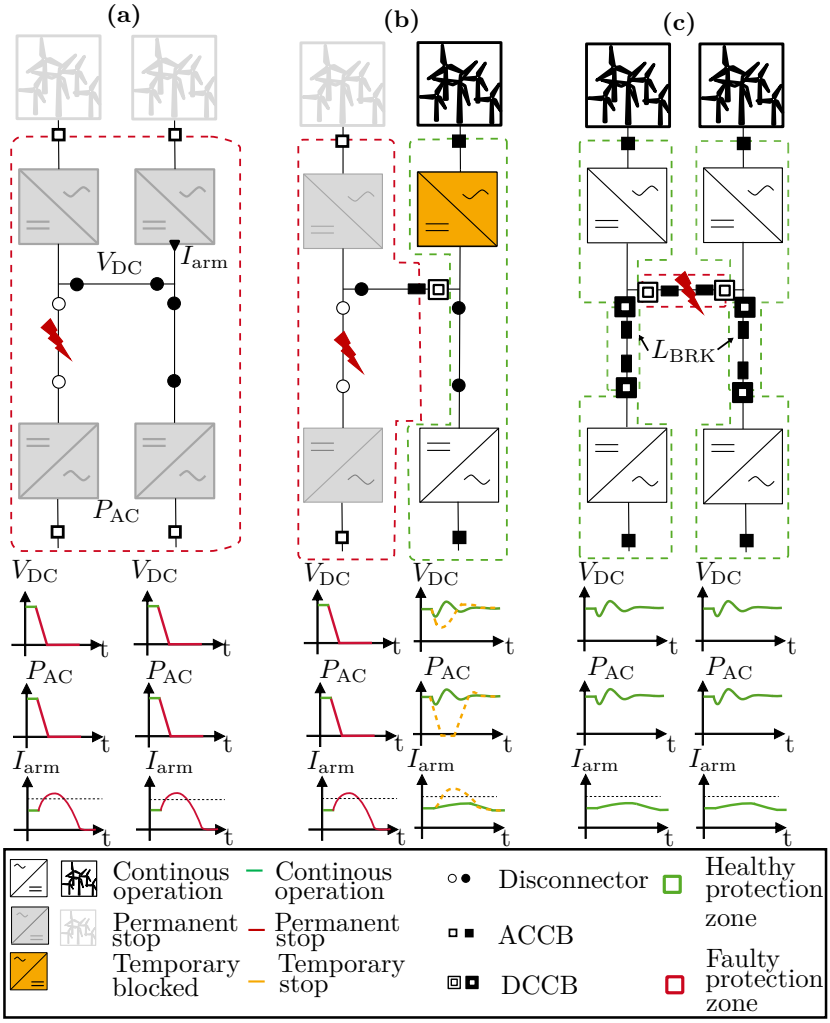


Figure 1.5: Overview of different protection philosophies a) non-selective, b) partially-selective, c) fully-selective

on control dynamics, and especially offshore, leads to increased size and cost of the platforms and is preferably avoided [RM23].

Allowing the converters to temporarily block the submodules instead of requiring continous operation can enable the use of slower breakers or significantly smaller inductances, as long as the fault current remains within the breaking limits of the DCCB [ALv20] (cf. Figure 1.5b, yellow). The possibility of using temporary blocking is also being discussed among the system operators, wind-turbine manufacturers and HVDC manufacturers [STV24]. In [ZJ19a], the implications of temporary blocking during DCCB operation are investigated for an HVDC system connected to voltage sources at each converter terminal. It analyzes the effects of temporary blocking on the breaker operation, the DC system voltage, and the AC systems. While it provides initial insights on the capabilities and requirements of temporary blocking, only a blocking duration of 12 ms together with a slow breaker is investigated. Furthermore, for offshore systems the stability of the offshore AC system plays an important role when blocking the offshore converter. Therefore, the use of GFM WTG as enabler of temporary blocking of the offshore converter needs to be investigated. The islanding capabilities of GFM WTG have been shown in [SAL21]. However, no full grid-forming control was used but rather a passive voltage support by the WTG control, limiting the active current infeed. An important aspect, the implications of different temporary blocking times on the healthy protection zone with GFM WTGs and the according protection design, have not yet been discussed. Adapting the control structure of the WTGs from GFL to GFM, also enables different control structures of the HVDC converters, such as DC voltage control of the offshore converter or GFM control of the onshore converter. As a result, temporary blocking could lead to deteriorated transient system behavior, which has to be evaluated and defined.

1.2.4 Research questions and thesis structure

The aim of this thesis is to evaluate the potential of using GFM WTG in combination with HVDC systems for energization and DC-side fault handling. Compared to GFL WTG, GFM WTG offer the potential of islanding during DC contingencies or possible offshore side energiza-

tion. This thesis has the objective to answer the following research questions:

- *What are the requirements for HVDC-connected OWPP to enable HVDC and grid energization?*
- *How can HVDC system recovery be achieved via GFM WTG after a DC-side fault?*
- *What is the impact of GFM WTG on DC-side protection design and system behavior during DC-side faults?*
- *Can GFM WTG avoid overload situations in bipolar systems with AC connected poles?*

In Chapter 2, the necessary technical considerations for evaluating the potential of GFM WTGs are presented. First, the controls are explained in detail, followed by the energization process and lastly the system behavior during DC-side faults.

Chapter 3 provides a detailed description of all models required for the investigations. For each investigation, different models are used based on the system complexity and required modeling depth. This includes an overview of the WTG model, the OWPP design, and HVDC system. Additionally, the ratings for each system part are provided. Finally, the implemented control for the converters of the HVDC system and the WTG are described.

To answer the first research question, Chapter 4 provides a detailed investigation of the black start of an onshore system through an HVDC-connected OWPP. First, the start-up of the OWPP is analyzed to derive the most stable approach for the offshore system energization based on the 66 kV direct connection topology. Afterwards, sensitivity analyses are performed for the energization of the HVDC system including different start-up methods and evaluating the impact of the system rating on the start-up process. From the results, requirements and sensitivities are derived.

In Chapter 5, the benefits of re-energizing the HVDC from the OWPP after a DC-side fault is analyzed. Depending on the fault location, the faulted part of the system is either reconnected to the healthy part of the HVDC system through the DCCB or to the onshore system. Compared

to the black start, the converters remain partially energized. Therefore, a sensitivity analysis is performed to derive the impact of remaining submodule charge depending on the chosen restart method.

Chapter 6 investigates the possibility to reduce the protection requirements with partially-selective fault clearing through temporary blocking of the offshore converter. During the temporary blocking, the OWPP will be islanded during which the AC power transfer is interrupted, which has to be mitigated by the system. Furthermore, the control structure of the system has a large impact on the system response, regarding DC-voltage, offshore system voltage and active power transfer.

In Chapter 7 the post-fault power flow control via the GFM WTGs in a bipolar MTDC system with connected AC-poles is analyzed. Fully-selective fault clearing of a DC-side fault requires to balance the active power of the poles via the AC-side coupling to avoid overloading of the DC-system. The requirements on the speed of the load flow adjustment as well as the possible curtailment of wind power are derived. The performance is compared to the load flow control provide by the converters in a state-of-the-art GFL WTG system.

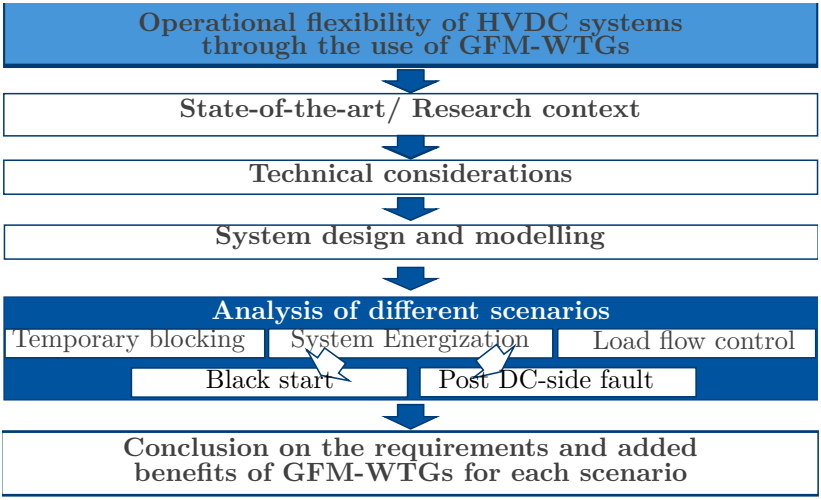


Figure 1.6: Overview of the thesis structure

Lastly, in Chapter 8, the benefits and drawbacks for each scenario will be concluded, to give a final overview of the added flexibility by using GFM WTGs.

2 Technological background

Identifying the potential of using GFM WTG in combination with an HVDC system for the energization and in DC-side fault scenarios requires an understanding of the relevant system components and system behavior. Consequently, the general design and working principle of the components and the controls have to be derived. Furthermore, the system behavior during energization and DC-side faults needs to be analyzed. Therefore, in Section 2.1.1, today's system design of the OWPP is discussed, which strongly influences the energization process. In Section 2.1.2, an overview of the most common turbine design relevant for this thesis is provided. In Section 2.1.3, the design and working principle of the modular multilevel converter (MMC) as the center component of the HVDC system are shown and derived. The differences between GFL and GFM are provided in Section 2.2.1 and 2.2.2. Lastly, the processes of energization and DC-side faults are discussed in Section 2.3 and Section 2.4, respectively.

2.1 HVDC-connected wind power plants

2.1.1 Offshore system design

As briefly mentioned in Chapter 1, the two main OWPP AC connection voltages in the North Sea are 33/155 kV and 66 kV, with 33/155 kV being used in the first HVDC-connected OWPP projects. The 33/155 kV design (see Figure 2.1b) consist of 33 kV collector platforms to cluster the WTGs in close proximity. The number of AC collector platforms depends on the overall size and geographical distances [Cig15]. However, to avoid excessive losses, large-scale HVDC-connected OWPPs require an intermediate voltage, e.g., 155 kV, to collect the 33 kV clusters before connecting to the offshore converter station.

In contrast, newer projects explore the use of 66 kV direct connection (see Figure 2.1a) to reduce costs by eliminating the AC offshore collector

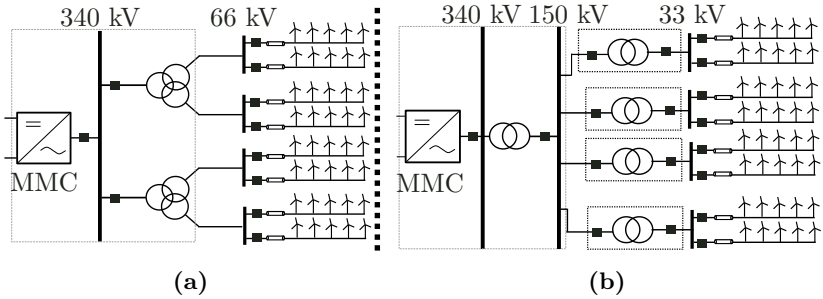


Figure 2.1: Schematic drawing of two connection topologies for an OWPP a) 66 kV direct connection, b) 33/150 kV connection with AC offshore platforms [Cig15]

platforms and additional transformers. At 66 kV, the layout usually follows a string-based system, directly connected to the offshore converter platform without the need for additional voltage transformation. On the HVDC platform at 66 kV usually two three-phase transformers are used. A possible design is four WTGs clusters, each connected to one phase of the transformers [vGL16, Cig15].

2.1.2 Type-4 wind turbine generator

Many different types of WTG designs have been developed (i.e., Fixed-speed wind turbine, doubly-fed induction generator and the variable-speed with full-scale converter) [SVS10, SS11]. While all technologies can be used to efficiently extract power from the wind the variable-speed with full-scale converter technology, also known as type-4 WTG, is the most suitable to provide grid-forming functions (cf. Figure 2.2). The full-scale back-to-back converter decouples the grid side from the machine side, allowing the permanent-magnet synchronous generator (PMSG) to operate at a frequency different from the grid. In GFM control, the grid side can provide the required grid frequency while the machine side can operate at the frequency of e.g., 30 Hz. In order to provide the maximum wind power, the rotor blade angle is adjusted by a pitch control, allowing the rotor speed and power output to be controlled. It is also possible to design the rotor blades in a way that

they are able to achieve the highest level of efficiency under optimum use [Hau17]. The mechanical power P_{m} the WTG can provide can be described with the following equation [Hau17]:

$$P_{\mathrm{m}} = \frac{1}{2}\pi R^2 \rho C_{\mathrm{p}}(\lambda,\theta_{\mathrm{pitch}}){v_{\mathrm{wind}}}^3 \tag{2.1}$$

ρ is the air density, R the radius if the blade of the WTG and v_{wind} is the wind speed. C_{p} is the power coefficient of the WTG and describes the relationship between, the mechanical power of the WTG, the tip speed ratio λ and the pitch angle θ_{pitch}.

$$\lambda = \frac{\Omega_{\mathrm{t}}}{v_{\mathrm{wind}}} \tag{2.2}$$

The tip speed ratio is calculated with Ω_{t}, the rotor angle speed. This results in multiple curves defining the relationship between the power coefficient and the pitch angle. Therefore, for a given tip speed rotation assuming constant winds, changing the pitch angle will result in different mechanical power outputs. The pitch angle can be adjusted in a way, so that the turbine rotates with zero power output. Negative values can also occur, which would result in a slowing down of the machine. Due to mechanical stress, this is preferably avoided [Hau17]. When the WTG provides GFM functions, the active power demand on the grid side changes faster than the machine side can respond. Therefore, in the DC link a capacitor is present to sufficiently decouple the grid and machine-side. For overvoltage situations in the DC link (i.e., due to a change from full power to lower power) a DC-chopper is used. When an overvoltage in the DC link is detected, due to a higher power supply than demand, the DC-chopper bridges the positive and negative pole of the DC link via a resistor. Within the resistor the energy is dissipated, requiring the resistor to be rated accordingly. For type-4 WTGs, the converters are based on VSC technology, which use insulated gate bipolar transistors (IGBTs). The converter is typically a two-level VSC (consisting of a combination of IGBTs in series to achieve the voltage rating and anti-parallel diode in series) [SVS10]. The converter control provides the switching signals for the IGBTs via pulse width modulation. Due to the switching frequency, harmonic filtering is generally required [SHN16].

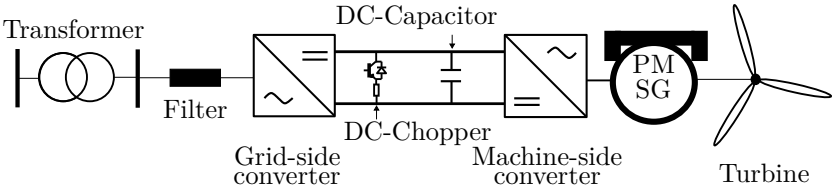


Figure 2.2: Schematic drawing of a type-4 WTG

2.1.3 Modular Multilevel Converter

As described in Section 1.2.2 different system architectures exist for HVDC systems. For every design in Europe, VSC-based systems are the preferred technology. Compared with line-commutated converter systems, which are primarily used for bulk power transmission in China and South America, the power transfer in VSC-based systems can be controlled via the current direction, allowing for an easy power-flow control. For VSC-based HVDC systems, the MMC is the prevalent converter technology. It can generate a high number of discrete voltage steps, producing a near-sinusoidal waveform with adjustable magnitude [SHN16]. The large number of voltage steps and lower switching frequency also eliminates the need for AC-filters, required for other converter technologies.

An MMC consists of three converter legs, each connected to one AC phase split into an upper and lower arm (Figure 2.3). Within each arm, there is a number of submodules (SMs) in series and an arm inductor L_{arm} to limit the rise of current within the converter arm. The DC voltage results from the sum of the inserted SMs voltages, reduced by the voltage drops across the arm resistance R_{arm} and the arm inductance L_{arm}. For the SMs, multiple concepts were developed with two main designs that are commercially developed, the half-bridge submodule (HBSM) and full-bridge submodule [Jov19, DQB15]. Since for offshore systems the HBSM is the prevalent technology, only HBSMs are considered further.

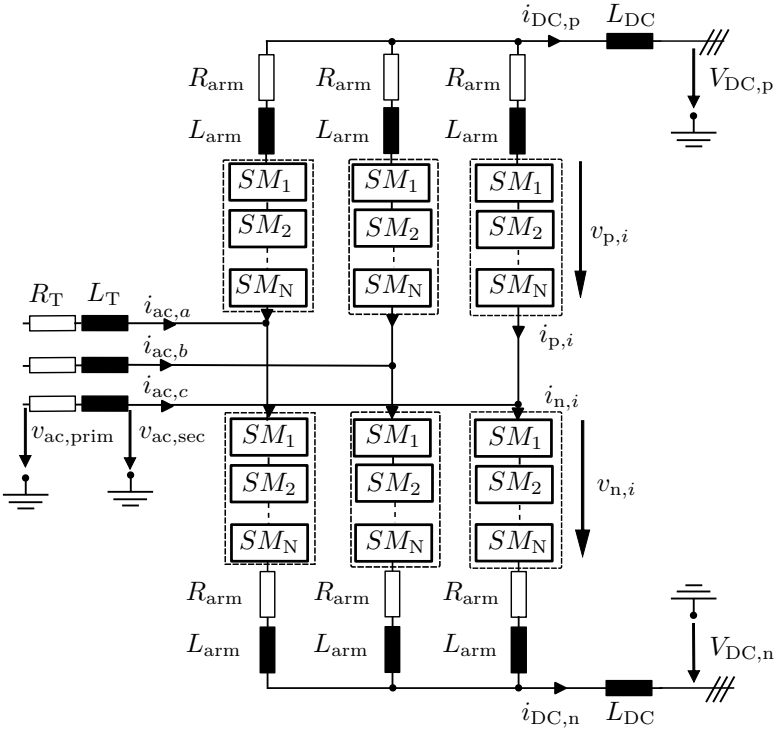


Figure 2.3: Schematic drawing of an MMC [SHN16]

Half-bridge submodule

An HBSM consists of two IGBTs T_1, T_2 with freewheeling diodes D_1, D_2. Additionally, each SM includes a capacitor C_{SM} for the energy storage to provide the voltage (Figure 2.4). Via the IGBTs, the of the SM can be controlled. HBSM can operate in three states: inserted, bypassed or blocked. In these states, the output voltage of the HBSM can either be v_{cap} or 0. In Table 2.1 the SM voltage and arm current based on the operation of the IGBTs are presented. In the inserted state, the submodule produces its maximum voltage for the given arm-current direction, whereas in the bypassed state the submodule output voltage is zero. The blocked state is an uncontrolled state, since the

IGBTs cannot be switched and the current has to flow through the anti-parallel diodes. Therefore, the SM voltage output depends on the current direction [SHN16, vGL16].

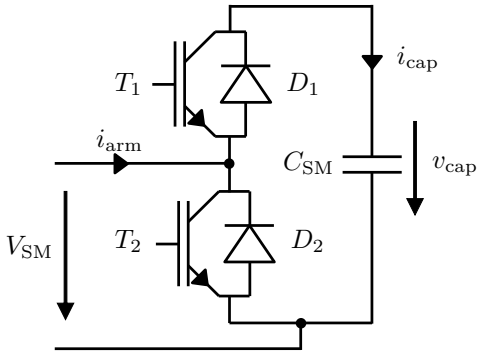


Figure 2.4: Schematic drawing of an HBSM [DQB15]

Table 2.1: HBSM operational states

State	T_1	T_2	V_{SM}		i_{cap}	
			$i_{\mathrm{arm}} > 0$	$i_{\mathrm{arm}} < 0$	$i_{\mathrm{arm}} > 0$	$i_{\mathrm{arm}} < 0$
Inserted	1	0	v_{cap}	v_{cap}	i_{arm}	i_{arm}
Bypass	0	1	0	0	0	0
Blocked	0	0	v_{cap}	0	i_{arm}	0

Working principle of the MMC

Due to the large number of SMs within the MMC, the converter behaves like a controllable voltage source. The voltage can be adjusted by changing the state of the SM (cf. Table 2.1), with the minimum voltage step equal to the capacitor voltage v_{cap}. Assuming that all SMs are actively controlled and either bypassed or inserted, the voltages of the upper- and lower-arm voltages of each phase are [SHN16]:

$$v_{\mathrm{p},i} = \sum_{j=1}^{N_{\mathrm{SM}}} T_{1,\mathrm{p},i,j}\, v_{\mathrm{cap},j} \tag{2.3}$$

$$v_{\mathrm{n},i} = \sum_{j=1}^{N_{\mathrm{SM}}} T_{1,\mathrm{n},i,j}\, v_{\mathrm{cap},j} \tag{2.4}$$

$T_{1,\mathrm{p},i,j}/T_{1,\mathrm{n},i,j}$ describe the switching states of the IGBT of each of the j-th SM and the i-th phase for the upper and lower arm, respectively. N_{SM} is the total number of SM.

The total DC voltage of the MMC, V_{DC}, is the sum of the DC voltages of the upper arm, $V_{\mathrm{DC,p}}$, and the lower arm, $V_{\mathrm{DC,n}}$. By applying Kirchhoff's voltage law to one arm and using the submodule voltages, these DC voltages can be written as follows [Lok22, Ruf20]:

$$V_{\mathrm{DC,p}} = v_{\mathrm{p},i} + R_{\mathrm{arm}}\, i_{\mathrm{p},i} + L_{\mathrm{arm}} \frac{d}{dt} i_{\mathrm{p},i} + L_{\mathrm{DC}} \frac{d}{dt} i_{\mathrm{DC,p}} \tag{2.5}$$

$$V_{\mathrm{DC,n}} = v_{\mathrm{n},i} + R_{\mathrm{arm}}\, i_{\mathrm{n},i} + L_{\mathrm{arm}} \frac{d}{dt} i_{\mathrm{n},i} + L_{\mathrm{DC}} \frac{d}{dt} i_{\mathrm{DC,n}} \tag{2.6}$$

With $i_{\mathrm{p},i}/i_{\mathrm{n},i}$ being the respective arm current of the lower and upper arm for each phase Adding (2.5) and (2.6) together, results in following equation for the DC relations.

$$\begin{aligned} V_{\mathrm{DC,p}} + V_{\mathrm{DC,n}} = {} & v_{\mathrm{p},i} + v_{\mathrm{n},i} + R_{\mathrm{arm}}(i_{\mathrm{p},i} + i_{\mathrm{n},i}) + R_{\mathrm{DC}}(i_{\mathrm{DC,p}} + i_{\mathrm{DC,n}}) \\ & + L_{\mathrm{arm}} \frac{d}{dt}(i_{\mathrm{p},i} + i_{\mathrm{n},i}) + L_{\mathrm{DC}} \frac{d}{dt}(i_{\mathrm{DC,p}} + i_{\mathrm{DC,n}}) \end{aligned} \tag{2.7}$$

The sum of the arm currents and the arm voltages in (2.7) can be written as the difference current $i_{\mathrm{diff},i}$ and difference voltage $\epsilon_{\mathrm{diff},i}$:

$$i_{\mathrm{diff},i} = \frac{i_{\mathrm{p},i} + i_{\mathrm{n},i}}{2} \tag{2.8}$$

$$\epsilon_{\mathrm{diff},i} = \frac{v_{\mathrm{p},i} + v_{\mathrm{n},i}}{2} \tag{2.9}$$

results in:

$$V_{\mathrm{DC,p}} + V_{\mathrm{DC,n}} = \epsilon_{\mathrm{diff},i} + R_{\mathrm{arm}}(i_{\mathrm{diff},i}) + R_{\mathrm{DC}}(I_{\mathrm{DC}}) + L_{\mathrm{arm}}\frac{d}{dt}(i_{\mathrm{diff},i}) + L_{\mathrm{DC}}\frac{d}{dt}I_{\mathrm{DC}} \tag{2.10}$$

Due to slight voltage differences $\epsilon_{\mathrm{cc},i}$, defined as the difference between the DC voltage and the difference voltage, circulating currents $i\mathrm{cc},i$ occur. These current are the sum of a third of a DC current and the difference currents. They can be expressed as:

$$\epsilon_{\mathrm{cc},i} = \epsilon_{\mathrm{diff},i} - \frac{\epsilon_{\mathrm{dc},i}}{2} \tag{2.11}$$

$$i\mathrm{cc},i = i_{\mathrm{diff},i} - i_{\mathrm{dc},i} = i_{\mathrm{diff},i} - \frac{I_{\mathrm{DC}}}{3} \tag{2.12}$$

With ϵ_{dc} being the equivalent voltage of the submodules.

With (2.11) and (2.12), (2.10) can be separated into its circulating current and DC components, resulting in [HAN13]:

$$V_{\mathrm{DC}} = \epsilon_{\mathrm{dc},i} + (\frac{2}{3}R_{\mathrm{arm}} + 2R_{\mathrm{DC}}) + (\frac{2}{3}L_{\mathrm{arm}} + 2L_{\mathrm{DC}})\frac{d}{dt}I_{\mathrm{DC}} \tag{2.13}$$

$$\epsilon_{\mathrm{cc},i} = -2L_{\mathrm{arm}}\frac{d}{dt}i\mathrm{cc},i - 2R_{\mathrm{arm}}i\mathrm{cc},i \tag{2.14}$$

The AC phase voltage $V_{\mathrm{AC,i}}$ is given by the voltage difference between the upper- and lower-arm voltages, $v_{\mathrm{p},i}$ and $v_{\mathrm{n},i}$, respectively, where i denotes the phase index. Hence, the AC phase voltage can be expressed as [HAN13]:

$$V_{\mathrm{AC,i}} = \frac{v_{\mathrm{p},i} - v_{\mathrm{n},i}}{2} - \left(R_{\mathrm{T}} + \frac{R_{\mathrm{arm}}}{2}\right) i_{\mathrm{ac,i}} + \left(L_{\mathrm{T}} + \frac{L_{\mathrm{arm}}}{2}\right) \frac{d}{dt} i_{\mathrm{ac,i}} \tag{2.15}$$

Here, $i_{\mathrm{AC},i}$ denotes the current flowing in phase i. R_{T} and L_{T} denote the transformer resistance and inductance (cf. Figure 2.3).

The voltage difference between the positive- and negative-arm submodules can be represented by an equivalent internal AC voltage $\epsilon_{\mathrm{ac},i}$ as defined in (2.16), leading to the simplified form in (2.17):

$$\epsilon_{\mathrm{ac},i} = \frac{v_{\mathrm{p},i} - v_{\mathrm{n},i}}{2} \tag{2.16}$$

$$V_{\mathrm{AC,i}} = \epsilon_{\mathrm{ac},i} - \left(R_{\mathrm{T}} + \frac{R_{\mathrm{arm}}}{2}\right) i_{\mathrm{ac,i}} + \left(L_{\mathrm{T}} + \frac{L_{\mathrm{arm}}}{2}\right) \frac{d}{dt} i_{\mathrm{ac,i}} \tag{2.17}$$

The three derived equations (2.13), (2.14) and (2.17) can be used to independently control the DC voltage, the circulating current and the AC-side quantities of the converter. A general control approach is the cascaded vector control,in which these three quantities are controlled separately and used to generate submodule switching commands [Cig14].

The relation of the AC- and DC-side voltage in the simplest case is given by $\hat{v}_{\mathrm{ac,sec}} = \frac{V_{\mathrm{DC}}}{2}$. However to achieve a higher operation flexibility usually a slightly differing arm voltage is used leading to the following relation.

$$M = \frac{2\hat{v}_{\mathrm{ac,sec}}}{V_{\mathrm{DC}}} \tag{2.18}$$

The modulation indexs M is defined as above. For HBSM modulation index can have values from $0 \leq M \leq 1$. An M larger than 1 would

require temporary negative arm voltages, which cannot be produced via HBSM (cf. Table 2.1). This constraint also limits the controllability of the MMC. For example, if the DC voltage drops due to a fault, the AC-side voltage may exceed the available DC voltage. As a result, the current will be fed into the fault [DBK23].

2.2 Converter controls

2.2.1 Grid-following control

Grid following control is the most common control strategy for power converters in today's grids. The main goal of the GFL control is to provide maximum active power into the grid by controlling the injected current [RLB12]. The converter receives setpoints for active power P^* and reactive power Q^*, which translate to the required power exchange between DC and AC system (P_{GFL} and Q_{GFL}). The current references for the inner current-control loops are calculated on basis of the reference and the measured power (cf. Figure 2.5).

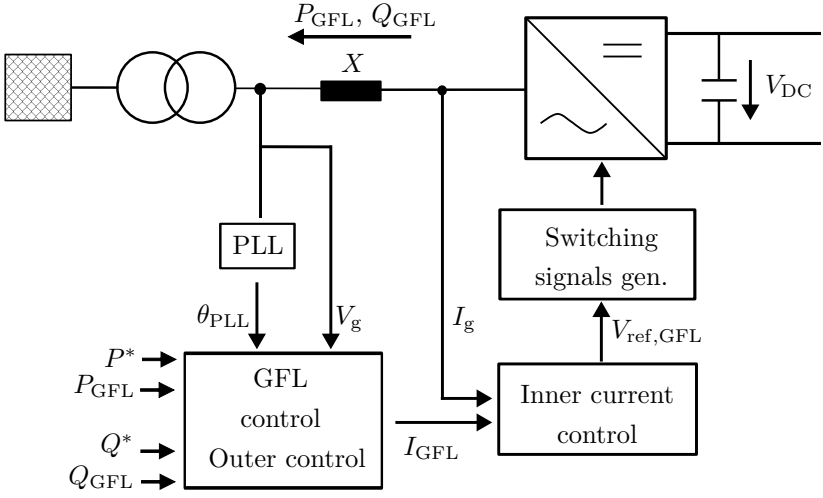


Figure 2.5: Block diagram GFL controlled VSC [RLB12, RWL21]

The physical relation between AC voltage, AC current and active power transmission can be written as [CW18]:

$$P = \sqrt{3} V_{\mathrm{g}} I_{\mathrm{g}} \cos(\phi) \tag{2.19}$$

The grid voltage V_{g} is assumed constant since it is provided by the AC grid. Therefore, the active power can be controlled by adjusting the supplied current I_{g}. Furthermore, this shows that the grid angle ϕ has to be tracked in order to align the voltage with the current. For the phase tracking, a phase-locked loop is most widely used. The PLL tracks the voltage angle of the grid to provide the angle θ_{PLL} for the abc/dq transformation. The control then operates in the synchronous reference frame (dq frame), which allows the usage of PI-controllers. The relationship between the active/reactive power, voltage and current in dq-coordinates can be written as [TLR11, WTW20]:

$$P_{\mathrm{AC}} = \frac{3}{2}(V_{\mathrm{g}}^{d} I_{\mathrm{g}}^{d} + V_{\mathrm{g}}^{q} I_{\mathrm{g}}^{q}) \tag{2.20}$$

$$Q_{\mathrm{AC}} = \frac{3}{2}(V_{\mathrm{g}}^{q} I_{\mathrm{g}}^{d} - V_{\mathrm{g}}^{d} I_{\mathrm{g}}^{q}) \tag{2.21}$$

To achieve an independent control of active and reactive power via the the p and q components of the current, the V_{g}^{q} component can be tuned to 0, by aligning the grid angle with the angle of the PLL [CLX22]. By controlling V_{g}^{q} to 0, (2.20) and (2.21) can be simplified to [RLB12]:

$$P_{\mathrm{GFL}} = \frac{3}{2}(V_{\mathrm{g}}^{d} I_{\mathrm{g}}^{d}) \tag{2.22}$$

$$Q_{\mathrm{GFL}} = -\frac{3}{2}(V_{\mathrm{g}}^{d} I_{\mathrm{g}}^{q}) \tag{2.23}$$

As a result, the active power can be controlled via the d-component of the current and the reactive power via the q-component. To provide the correct d- and q-axis currents, an inner current-control loop is used. The converter current I_{g} is compared to the reference value I_{GFL}, which consist of the reference values for the d-currentI_{d}^{*} and q-current I_{q}^{*}.

The output of the current control is the voltage reference $V_{\mathrm{ref,GFL}}$, to generate the switching signals for the converter.

Since the injected current I_{g} is kept constant to provide constant active power, the behavior of a GFL-controlled converter can be described as a current source with a high parallel impedance Z_{c} (Figure 2.6a). During a grid disturbance and subsequent change in grid voltage V_{g}, the converter current I_{g} is held to remain constant with the voltage drop across the grid impedance Z_{g} constant as well. This leads to a change in the output voltage of the converter V_{c}, since the new phase angle of the grid voltage has to be determined first to derive the new current set point. The resulting phase shift can cause instabilities. (Figure 2.6b [RLB12].

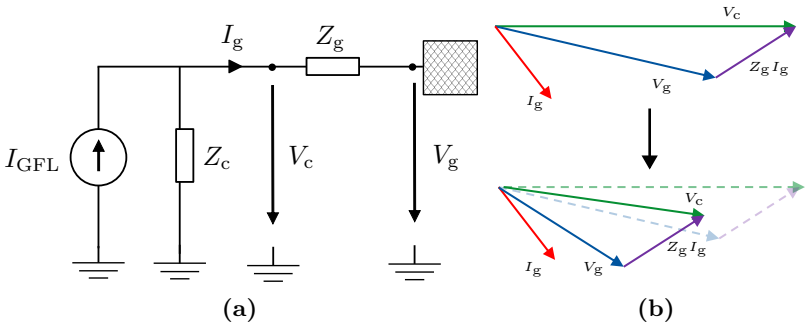


Figure 2.6: Working principle GFL controlled VSC [RLB12, RWL21]

2.2.2 Grid-forming control

Contrary to the GFL controlled converter, GFM control does not require a PLL to synchronize to the grid and aims to work as an ideal AC voltage source. A GFM control has two main control adaptions compared with GFL control. A voltage-control loop is added to provide the required output voltage and a synchronization loop to provide the angle for the dq-transformation (Figure 2.8a, Outer Control Loop). For two rotating systems that are coupled by an inductive reactance, for converter systems usually the transformer reactance X_{T} and/or the filter reactance X_{F}

(depending on the converter type) the active- (2.24) and reactive-power (2.25) relations can be derived [RLB12, UNS20]:

$$P_{\mathrm{GFM}} = \frac{V_{\mathrm{GFM}}}{X}(V_{\mathrm{g}} \sin \theta_{\mathrm{GFM}}) \tag{2.24}$$

$$Q_{\mathrm{GFM}} = \frac{V_{\mathrm{GFM}}}{X}(V_{\mathrm{GFM}} - V_{\mathrm{g}} \cos \theta_{\mathrm{GFM}}) \tag{2.25}$$

Usually, the power angle θ_{GFM} is considered small, so that $sin(\theta_{\mathrm{GFM}}) \approx \theta_{\mathrm{GFM}}$ and $cos(\theta_{\mathrm{GFM}}) \approx 1$, resulting in the simplified expressions (2.26) and (2.27) [RLB12, LSK05].

$$\theta_{\mathrm{GFM}} = \frac{X P_{\mathrm{GFM}}}{V_{\mathrm{GFM}} V_{\mathrm{g}}} \tag{2.26}$$

$$V_{\mathrm{GFM}} - V_{\mathrm{g}} = \frac{X Q_{\mathrm{GFM}}}{V_{\mathrm{GFM}}} \tag{2.27}$$

(2.26) shows a direct connection between the angle and the power injected into the grid. Therefore, the power angle θ_{GFM} can be determined by the injected power into the grid.

Since a GFM-controlled converter aims to keep the output voltage constant, the current deviates during a grid disturbance (see Figure 2.8b). Therefore, the GFM control is can maintain its grid-forming capability only as long as the current remains within the converter's limits. The limitation is usually maintained via an inner current-control loop (Figure 2.8a, Inner Control Loops) [WTW20].

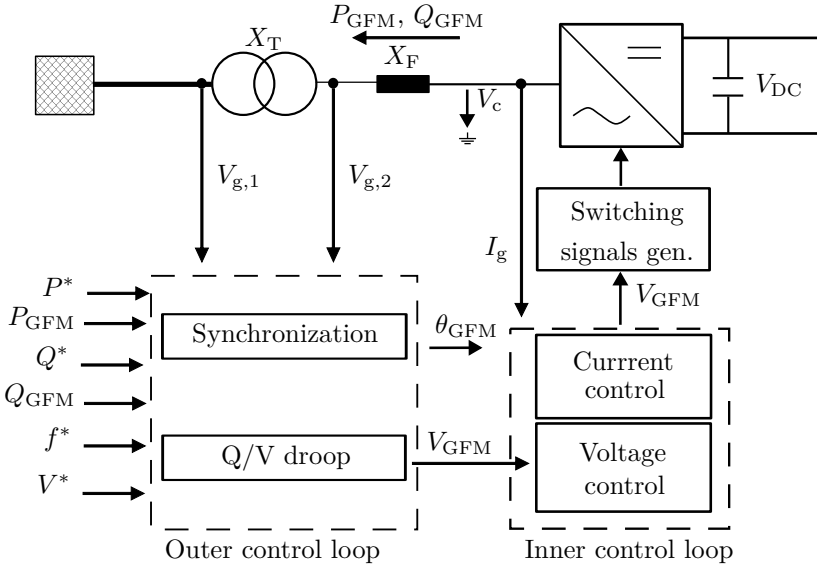


Figure 2.7: Block diagram of a GFM controlled VSC [RLB12, RWL21]

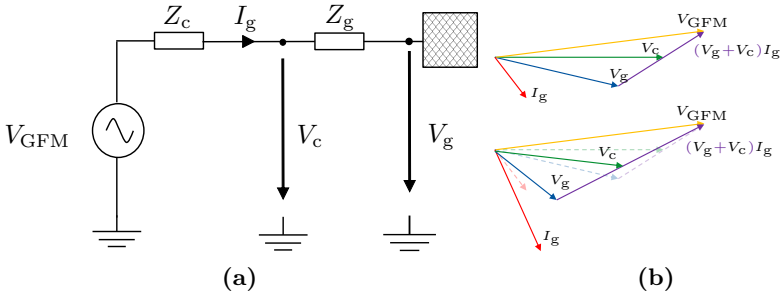


Figure 2.8: Working principle of GFM controlled VSC [RLB12, RWL21]

2.3 Energization of an offshore HVDC system

2.3.1 System energization

Energization in transmission systems describes the process of applying voltage to the system. The system generally consists of inductive and capacitive components, for which the corresponding magnetic and electric fields must be established as voltage is applied and current begins to flow. In offshore HVDC systems, the components that strongly influence the transient behavior are the transformer, the MMCs, and cables. Hard and soft energization are the two main approaches used for power system energization.

2.3.2 Hard energization

The prevalent method for energizing AC transmission systems is the hard energization. Within the hard energization, the system components are separated by circuit breakers and connected stepwise at rated system voltage. From a system operation point of view, this allows for distinct control of the timing between the steps, ensuring system stability and proper protection operation. However, connecting at rated voltage leads to large inrush currents, especially when energizing inductive or capacitive components (e.g., transformers, cables). For transformers, the inrush current reaches its maximum in the first few milliseconds after being connected and slowly decays until the transformer is fully magnetized. As power electronics can withstand only a limited overcurrent before being damaged, it is important to limit these inrush currents. Otherwise, the converters would either lose their controllability due to being in the current limitation or shut down due to overcurrent protection. Common solutions to reduce the inrush currents within the hard energization are, point-on-wave switching or the use of PIRs [AAE23, TV07, Cig04]. Both methods have been proven to be effective. The pre-insertion resistor is inserted during AC breaker closing and then bypassed once the component is energized and the inrush current is decayed. The point-on-wave switching requires measurements of each phase and knowledge of the remanent flux of the transformer as well as

independent switching of each breaker phase. Within this thesis, the method with PIR is considered, since it reduces complexity and has been proven for OWPP energization [JSS21a].

Similarly, when energizing the MMC, the submodule capacitances lead to an inrush current due to the large number of capacitors connected in series. During the uncontrolled charging phase, all of the submodules are in the blocked state and the converter control is deactivated. During this stage, the charging of the MMC, while more complex, can be approximated by charging an RC circuit. Since $\tau_{\mathrm{C}} \ll \tau_{\mathrm{L}}$. The required active power depends on the applied voltage, the total resistance in the capacitor path, and the energy already stored in the submodules. In order to increase the charging time and flatten the initial inrush current a PIR can be used to increase the charging time based on $C_{\mathrm{SM,tot}} \cdot (R_{\mathrm{arm}} + R_{\mathrm{PIR}})$.

2.3.3 Soft energization

Alternatively, the soft energization is seen as a viable solution to reduce inrush transients. For the soft energization, all breakers between components to be energized are closed before applying voltage. The voltage is then gradually increased to rated level, and the resulting currents are dependent on the applied ramp rate. For the soft energization, no PIRs are required, because the voltage across all inductive and capacitive components increases proportional to the system value. The downside is, there are no separating boundaries between the components since all breakers are closed prior to the start up, which could be a challenge in fault handling and require a separate investigation for sensitizing protection for these low-voltage situations. [JSS21a].

2.3.4 Energization of the MMC

Independent on the charging method the energization of the MMC has to be investigated separately since its charging follows two distinct steps, namely the uncontrolled energization and the controlled energization. The uncontrolled energization, is described as the state, when the breaker is closed and the SMs are charged without an active control. During this step, the charging curve can be adjusted via the two aforementioned

methods, to reduce the inrush current since it is a purely capacitive charging process. During the uncontrolled energization, the charging depends on the direction of charging the MMC, i.e. via the AC or DC side.

AC-side energization

During the uncontrolled energization, the submodules are blocked, so the only current path is through the freewheeling diodes and not through the IGBTs. Therefore, the charging state is dependent on the direction of the current flowing through the arm (cf. Table 2.1), which is dependent on the voltage potential between the three phases. If the arm current is negative, it flows through the diodes. If the arm current is positive, it flows through the capacitor, charging the submodules (cf. Figure 2.9). As a result, depending on the voltage level of each phase, two of the three upper and lower arms simultaneously charged (cf Figure 2.9). The current flows from the higher potential in phase a, with the potential v_a, to the lower potentials v_b and v_c. The largest difference occurs if $v_\mathrm{a} = \hat{v}_\mathrm{av}$ and $v_\mathrm{b} = -\hat{v}_\mathrm{av}$. This leads to a total voltage difference of the arm of $2\hat{v}_\mathrm{av}$. Accordingly, the following equation for the maximum achievable voltage level prior to controlled operation of the SMs can be derived [LXZ15, SLW15]:

$$V_\mathrm{SM,pre,AC} = \frac{V_\mathrm{AC,rms}\sqrt{2}}{N_\mathrm{SM}} \tag{2.28}$$

DC-side energization

If the converter is energized from the DC side, the DC voltage is applied evenly over the submodules within each arm. Since the lower and the upper arm are each connected to half of the DC voltage, the following equation can be derived [LXZ15, SLW15]:

$$V_\mathrm{SM,pre,DC} = \frac{V_\mathrm{DC}}{2N_\mathrm{SM}} \tag{2.29}$$

(2.28) and (2.29) show that the energization of the MMC is initially dependent on the system ratings. Therefore, the startup has to be

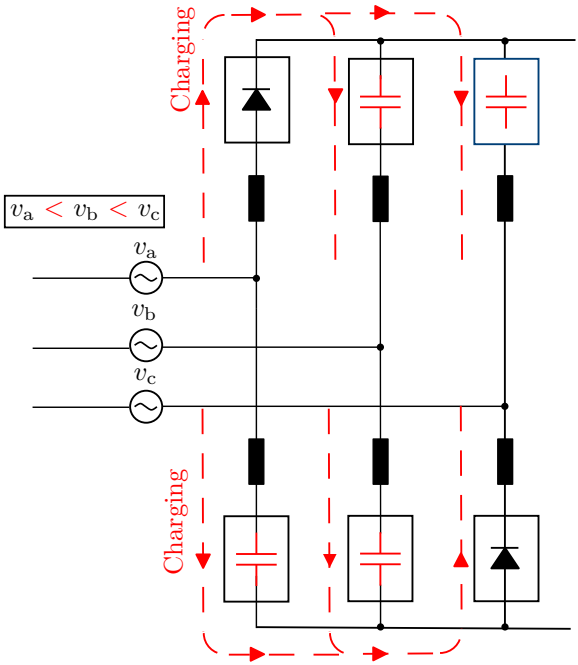


Figure 2.9: Schematic drawing of the initial AC-side energization of the MMC [LXZ15]

evaluated for planned systems independently. Especially, the number of SMs has a large impact on the achievable state of charge prior to activating the converter controls. As a result, accurate controller tuning is required.

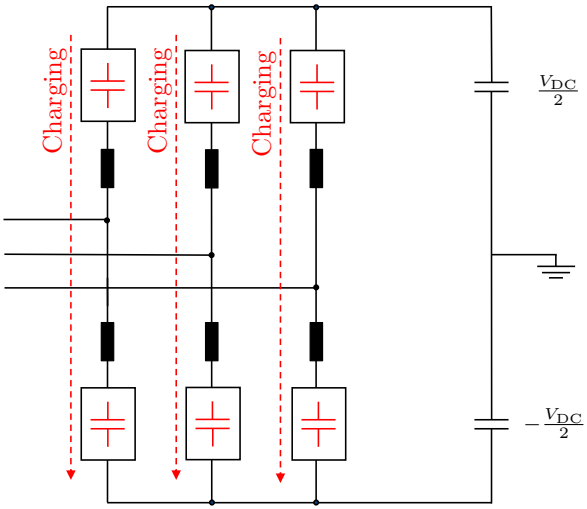


Figure 2.10: Schematic drawing of the initial DC-side energization of the MMC [LXZ15]

2.4 Faults in HVDC systems

HVDC systems for offshore connections are usually connected via submarine or underground cables. In contrast to overhead lines, faults in cables occur less frequent, but are usually permanent and require the cable to be repaired. Fast fault separation of the cable from the rest of the network is required by means of the in Section 1.2.3 described protection philosophies. Typical fault causes are production or installation errors, material fatigue or accidents cause by e.g., ship anchors. The most probable fault in cable systems is the pole-to-ground (PG) fault. Depending on the grounding design, the fault behavior is either dominated by a high overvoltage or high overcurrents. Submarine cables are usually laid as single cables making pole-to-pole-to-ground faults less frequent. However, they are more serious than PG faults due to high overcurrents [PRO16b, PRO16a]. In contrast to AC-side faults, DC-side faults have high current gradients due to the lack of inertia in the system and a missing current zero crossing. The current amplitude is system design dependent and changes based on a lot of factors, e.g.,

submodule type, cable length and design, fault location and resistance, grounding scheme, and the system inductance [BF13].

In HVDC systems, the fault current contribution can be separated into three stages, the capacitive discharge, AC transient infeed and AC steady-state infeed [BPS18, BF13, CWM18]. The capacitive discharge consist of the discharge of the submodules and the DC cables into the fault. For the operation of the converter, especially the continuous operation described in Section 1.2.3, the capacitive discharge of the submodules is the relevant factor that leads to blocking of the converter. The other three aspects are relevant for the interruption capabilities of either the DCCB or AC breaker operation. The DC-side voltage drop, leads to a discharge of the SM resulting in a sharp current rise within the submodules within a few milliseconds after fault occurrence. This current rise continues until either the fault is interrupted by the protection system or the protective blocking threshold of the converter is reached. This leads to a blocking of the converter and loss of transmission. Therefore, DCCB and/or current-limiting inductors have to be chosen accordingly to limit the rise in internal current and avoid blocking of the converter if continuous operation of the system is required by the system operator [DBK23].

3 Component and system models

This chapter provides an overview of the system models, implemented controls and ratings for the following investigations. First, Section 3.1 provides a general overview of the OWPP model. To increase simulation speed while maintaining accuracy, different simplifications are applied throughout the investigations. In Section 3.1.1, the implemented WTG model is described together with its ratings. Additionally, the controls for the WTG are described. This includes the standard GFL control as well as the implemented GFM control for the grid-side converter. Section 3.2 gives an overview of the implemented HVDC designs which are required for the different investigations. Based on the in Section 2.1.3 derived equations, Section 3.2.1 provides an overview on the implemented MMC control. In Section 3.2.2 the simplified protection design for DC-side fault clearing is described. Lastly, in Section 3.3 the implemented frequency-dependent cable model and the π-section approximation is provided. All investigations are carried out within electromagnetic transient analysis. In all investigations, a time step of 20 μs is used.

3.1 Offshore wind power plant model

As described in Section 2.1.1, a possible layout for the OWPP is a string-based, direct-connected layout, leading to four clusters, each connected to one phase of the transformers. During the energization process, the aim is to analyze the requirements at WTG, OWPP, and HVDC level. However, electromagnetic transient (EMT) simulation at WTG level for more than 100 WTGs is computationally infeasible. Therefore, a partially aggregated modeling approach is chosen. During the first stage of the energization process, two strings are modeled in detail, allowing the impact of energization on the first WTG to be analyzed explicitly. After the energization of these two detailed strings, it is assumed that the requirements on each individual WTGs are sufficiently low. Therefore, aggregation of the remaining strings is a suitable approximation, while still enabling the analysis of interactions between the WTG clusters (cf. Figure 3.1a). Especially since the clusters

are sufficiently decoupled via the transformers. In order to aggregate a WTG, the current is multiplied by the number of aggregated WTG. Since the current is amplified, the cables have to be aggregated as well to account for current rating and losses. Each cable section is parallelized by the number of strings. The detailed calculation can be found in Appendix A.2.1. For the DC-side investigation, the focus lies on the interaction with the converter and the DC-side behavior. Furthermore, since an MTDC system with two offshore terminals is considered, the number of WTG is doubled. Therefore, all strings are equally aggregated to increase simulation speed while maintaining the required accuracy for the investigation (cf. Figure 3.1b).

OWPP rating

The total power of the OWPP is rated at 1 GW. A string based layout with 28 strings with 5 WTGs each is chosen. This results in four clusters (A,B,C, and D), each connected to one transformer phase. Each cluster comprises of 7 strings. Since the first two strings are modeled in detail, the rest of the 5 strings are aggregated to represent 25 WTGs. All other clusters (B,C and D) are fully aggregated with 35 WTGs each (cf. Figure 3.1a). For the DC-fault analysis, cluster A is also fully aggregated, making all four clusters identical (cf. Figure 3.1b). The cable length $l_{\text{cable,AC}}$ is set to 15 km and each π-section segment l_{Pi} is 1 km long.

3.1.1 Wind turbine generator model

The WTG model is identical for all investigations and is a type-4 WTG with two back-to-back converters based on the standard type-4 WTG design (cf. Section 2.1.2). The two converters are modeled as two-level VSCs. The can be operated as detailed or average converter model. Within the detailed model, the switching of the IGBTs is modeled, significantly increasing simulation time. Alternatively, the average model eliminates the switching, while the signal generation remains identical. This significantly improves simulation speed, while maintaining the systems response behavior [Man18, ASM19]. For the switching, two LC filters are implemented on the machine and grid side. A three-phase Y-δ transformer is used to match the WTG voltage V_{GS} to grid voltage V_{G}. A DC-link chopper is implemented to reduce

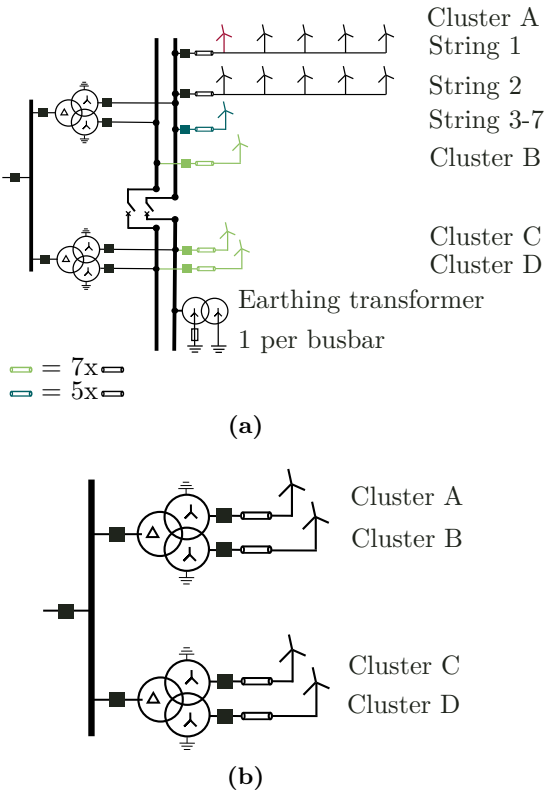


Figure 3.1: Schematic drawing of the OWPP models with a) full aggregation green: 25 WTG aggregation, blue: 35 WTG aggregation, b) partial aggregation

the DC-link voltage during DC-link overvoltages (cf. Figure 3.2) This might occur if the grid-side reduces the power output to zero while the machine side still produces active power. After a power adjustment by the grid-side converter, the machine side must follow; however, this adaptation generally reacts slower than the demand change on the grid side. To partially decouple the machine and grid side, a DC capacitance is implemented in the DC-link. The machine side is fully modeled with a PMSG and WTG controller adjusting the pitch angle according to power output and rotor speed, providing the torque reference T^* for

the PMSG (cf. Figure 3.2).

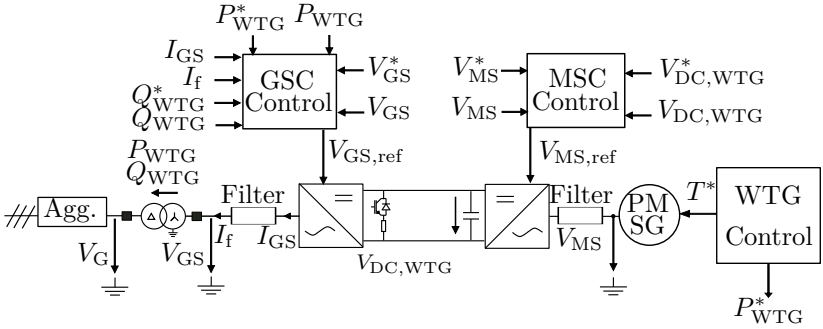


Figure 3.2: Schematic drawing of the WTG model

WTG ratings

The DC-link voltage is set to 1.45 kV and is operated within the voltage band from 1.35 kV - 1.55 kV, which limits the extractable energy from the DC link. Therefore, a DC-link capacitor of 0.15 F is used to sufficiently decouple the grid and machine sides. Each WTG is rated at 8 MVA (cf. Table 3.1). The AC voltage level of the WTG is 0.69 kV on both the grid and machine sides of the converter (V_{GS} and V_{MS}). The transformer model includes saturation to investigate the start-up requirements, when energizing the WTG.

3.1.2 WTG control

Grid-forming control

To enable islanding and energization, a suitable GFM control for the WTG is required. Various grid-forming controls have been developed and investigated for different applications. In literature, GFM controls have been compared for their general functionality in [UNS20] and for black-start application in [JDG18, PBB20, AAE20]. All references show a variation of the VSM that was first explicitly mentioned in [BH07] and since then developed for various applications such as microgrids or WTGs [BSC18, OTO24].

Table 3.1: WTG parameters

Parameter	Symbol	Value
Rated power rating	$S_{\mathrm{r,WTG}}$	8 MVA
Transformer primary voltage	V_{G}	66 kV
Transformer secondary voltage	V_{GS}	0.69 kV
Transformer generator voltage	V_{MS}	0.69 kV
Transformer inductance	$X_{\mathrm{trafo,WTG}}$	0.1 p.u.
GSC switching frequency	f_{SW}	3 kHz
DC-link nominal voltage	$V_{\mathrm{DC,WTG}}$	1.45 kV
DC-link capacitance	C_{DC}	0.15 F

Therefore, for the grid-forming control of the grid-side converter a VSM representation based on [DSF13] is implemented. As discussed in Section 2.2.2, a GFM control has a dedicated synchronization control loop to provide the angle. Within a VSM control the angle is determined by the swing equation, which is based on the traditional behavior of synchronous generators [UNS20, DSF13]. The swing equation is given in (3.1). The original equation is based on the torque difference between two rotating systems. For the control design the equation is multiplied by the angular frequency ω resulting in the active power P representation [RWL21, JDG18, DSF13].

$$P_{\mathrm{m}} - P_{\mathrm{e}} - P_{\mathrm{D}} = P_{\mathrm{m}} - P_{\mathrm{e}} - D\omega = J\omega_0 d\omega/dt \tag{3.1}$$

From the swing equation, the control is derived by using the relationship between the power difference, inertia J, and damping D to obtain the system frequency. The phase angle for the dq transformation is determined by integrating the frequency (cf. 3.3, pink).

To enable reactive power sharing among the WTGs during the startup process, a Q/V droop is used to provide the voltage reference V^* for the lower-level control (cf. 3.3, yellow). Within the lower level controls a cascaded control with a voltage and current control is implemented. The current controller subtracts the Q/V droop value from the reference

voltage V_{GS}^{*} to provide the current reference which is compared with the output current I_{GS} (cf. Figure 3.3, blue). Within the current controller, the filtered current is subtracted to provide the voltage compared with the output voltage V_{GS}, providing the voltage reference $V_{\mathrm{GS,ref}}$ for the switching signal generation via the PWM (cf. Figure 3.3, green). In order to sufficiently decouple the d and q axes, two decoupling terms are used $j\omega C_{\mathrm{f}}$ and $j\omega L_{\mathrm{f}}$, with L_{f} as the filter inductance and the C_{f} filter capacitance and inductance respectively. To limit the current to the maximum permissible output, when both active and reactive power are supplied, the sum of i_{d} and i_{q} is limited to 1.1 p.u.

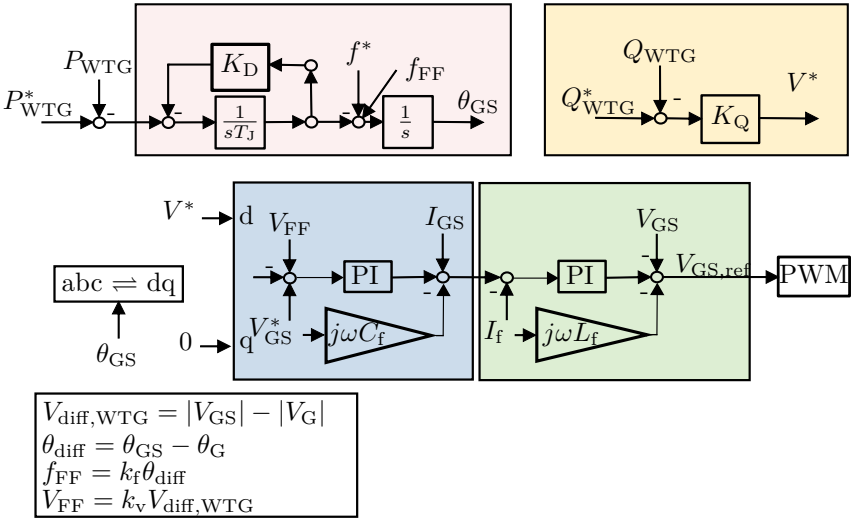


Figure 3.3: Block diagram of implemented VSM control [KDO23]

Connecting two GFM controllers requires prior synchronization, especially when their respective phase angles are shifted due to prior energization. A large angle difference between two GFM controls upon connection can lead to instabilities or make the system start-up impossible. Therefore, a synchronizing unit is implemented which tracks the phase, voltage and frequency on each side of the circuit breaker at the WTG terminal. With the tracked values a voltage V_{FF} and frequency feedforward f_{FF} are determined, which are supplied into the control. The f_{FF} inside the synchronization loop and the V_{FF} in the voltage

control loop. (cf. Figure 3.3). As a result, the phase angle and voltage between the two GFM is matched. Additionally, the matching greatly reduces the active power requirement, which would normally result due to the angle difference in the synchronization loop. The control parameters can be found in the Appendix A.3.

Machine-side control

In a state-of-the-art control architecture, the grid-side converter controls the DC voltage, while the machine-side converter provides the power reference providing the maximum power, depending on the wind conditions. In a grid-forming design, the DC voltage controller has to change from the grid-side converter to the machine side converter [BVB13]. A change in active power by the GFM control has an immediate impact on the DC-link, providing feedback via the machine-side control, that a power adjustment of the turbine is required. To avoid overloading of the WTG in various wind conditions, the pitch-control is maintained by the rotational speed of the permanent-magnet synchronous generator (PMSG), to reduce the power by adjusting the pitch if required.

For the GFL WTGs, a standard EMT model is used, with the control architecture as described before [Man18].

3.2 HVDC System

For the HVDC system, different interconnections and topologies are considered adapted to the complexity of each investigation based on the descriptions in Section 1.2.2. The model used for the energization investigations is a point-to-point monopolar link (see Figure 3.4 a). Since the focus lies on the interactions within the OWPP and the charging of the offshore converter, this level of complexity is chosen. The topology allows for deriving a set of requirements for the energization process without adding uncertainties through added complexity such as having control interactions between the P-pole and N-pole converters of a bipolar system. For the DC-side fault investigations, the HVDC system is expanded to a linear MTDC system interconnecting two point-to-point links via an interconnection at the offshore side. On one converter platform a DCCB is implemented to investigate the

system behavior and DC-side fault response with partially-selective fault clearing see Figure 3.4a, dashed lines). As a last step, the system is changed to a bipolar configuration with fully-selective fault clearing and interconnected poles on the AC side. This setup has the highest requirements on immediate post-fault load transfer, requiring adaptation of the controls Figure 3.4b, AC coupling dotted).

The converters are modeled with half-bridge submodules, as it is the prevalent technology for offshore connections (see Figure 3.4c). The submodule representation is a type-4 representation as specified in [Cig14]. Although electrically the submodule is modeled as a single voltage source, each submodule voltage is calculated individually. This is especially important to analyze the charging process of the MMC during the re-energization and investigate the impact of the remaining submodule voltage on the system behavior. On the offshore platform, two three-phase transformers are modeled, being the standard design for direct offshore connections. The transformers are modeled with saturation, in order to accurately model the energization and inrush currents (cf. AppendixA.5). At the AC-POC, two onshore connection designs are considered depending on the investigation. One design modeled the AC system as variable load R_{var} in order to perform distinct load steps investigating the response of the OWPP. Alternatively, the AC system is modeled as a voltage source emulating different grid strengths by adjusting the inner resistance and inductance values R_{i} and L_{i}. The respective parameters can be found in Appendix A.6

HVDC ratings

The parameters for the HVDC systems within the investigations are based on state-of-the-art systems as well as derived from discussion with industry partners. For both setups (monopole and bipole), the AC-voltage ratings are identical. The DC voltage for the monopole is $\pm 320\,\mathrm{kV}$, the bipole operates at $\pm 525\,\mathrm{kV}$.

The other relevant parameters are listed in Table 3.2. The maximum arm current is based on currenlyt available IGBT datasheets. Generally, a factor of 1.35 - 2 p.u. of the maximum DC current is used. Since within the investigations protection requirements are tested which rely on the blocking times of the converter the lowest rating is chosen [DDM23,

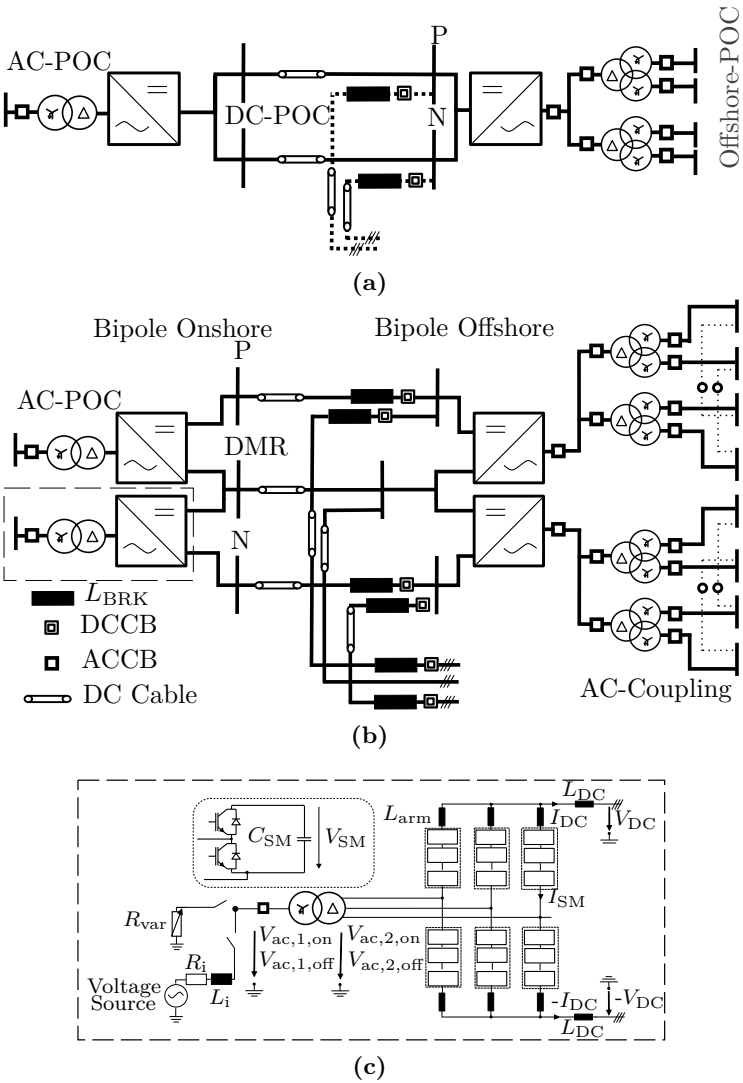


Figure 3.4: Schematic drawing of the a) monopolar system b) bipolar system c) MMC model

Table 3.2: HVDC system parameters

Parameter	Symbol	Monopole	Bipole
Rated power	P_{r}	900 MW	2 GW
Rated reactive power	Q_{r}	300 MVAr	667 MVAr
Rated DC voltage	V_{DC}	±320 kV	±525 kV
Nominal DC current	I_{DC}	1.4 kA	1.874 kA
Nr. of submodules	N_{SM}	300	270
Nominal submodule voltage	$V_{\mathrm{SM,nom}}$	2.4 kV	2.7 kV
Maximum submodule voltage	$v_{\mathrm{SM,nom}}$	2.4 kV	2.7 kV
Submodule capacitance	C_{SM}	8.8 mF	8.8 mF
DC terminal inductor	L_{DC}	25 mH	40 mH
Arm inductor	L_{arm}	50 mH	50 mH
Maximum arm current	$i_{\mathrm{arm,max}}$	2.7 kA	2.7 kA
Rated transformer power	S_{r}	1065 MVA	1065 MVA
Nominal AC primary voltage (onshore grid)	$V_{\mathrm{ac,1,on}}$	400 kV	400 kV
Nominal AC secondary voltage (onshore conv.)	$V_{\mathrm{ac,2,on}}$	350 kV	350 kV
Nominal AC primary voltage (offshore system)	$V_{\mathrm{ac,1,off}}$	66 kV	66 kV
Nominal AC secondary voltage (offshore conv.)	$V_{\mathrm{ac,2,off}}$	340 kV	340 kV

Inf21, ABB25]. The cables for each interconnection within the systems is set to 300 km.

Given the values in Table 3.2, the uncontrolled charging values for the submodules within the monopolar configuration can be calculated with (2.28) and (2.29). If the MMC charged from the AC side, the resulting submodule charge level is 0.67 p.u. (3.3). For charging from the DC side a submodule pre-charge level of 0.45 p.u is achieved (3.5).

$$V_{\mathrm{SM,pre,AC}} = \frac{V_{\mathrm{AC,rms}} * \sqrt{2}}{N_{\mathrm{SM}}} = \frac{340\,kV * \sqrt{2}}{300} = 1.6\,kV \tag{3.2}$$

$$V_{\mathrm{SM,pre,AC,pu}} = \frac{1.6\,kV}{2.4\,kV} = 0.67\,p.u. \tag{3.3}$$

$$V_{\mathrm{SM,pre,DC}} = \frac{V_{\mathrm{DC}}}{2 * N_{\mathrm{SM}}} = \frac{640\,kV}{2 * 300} = 1.07\,kV \tag{3.4}$$

$$V_{\mathrm{SM,pre,DC,pu}} = \frac{1.07\,kV}{2.4\,kV} = 0.45\,p.u. \tag{3.5}$$

3.2.1 MMC control

The implemented control for the MMCs is an energy-based cascaded vector control. Based on the equations in Section 2.1.3, the DC, AC, and circulating currents can be controlled individually [RCB19b, Lok22, Cig14]. Accordingly, the control consists of three decoupled current-control loops, i.e., the DC-side, AC-side and circulating current control (Figure 3.5). In an energy-based control the overall converter energy is always maintained by either the DC-side or the AC-side, depending if the converter maintains the DC voltage or controls the AC-side quantities (Figure 3.5, yellow). These latter quantities can be either active power in grid-following mode (Figure 3.5, light green) or a V_{AC}/f droop as grid-forming control (Figure 3.5, dark green). Within this study, the control aims to limit the DC fault current contribution by lowering the DC-side voltage and allows for fast DC voltage tracking, with a DC voltage feed-forward inside the current control loop [DDM23, RCB19b]. The circulating current control balances the internal energy between the arms of the converter. The resulting current references of each control are then processed via the respective current controls, resulting in the three voltage references for the submodules.

3.2.2 HVDC protection

Since HVDC system protection is not the main focus of this dissertation but required to investigate fault scenarios, a simplified detection and breaker representation are used throughout the studies. In [ZJK20], a generic circuit breaker model is proposed, which is sufficient to represent

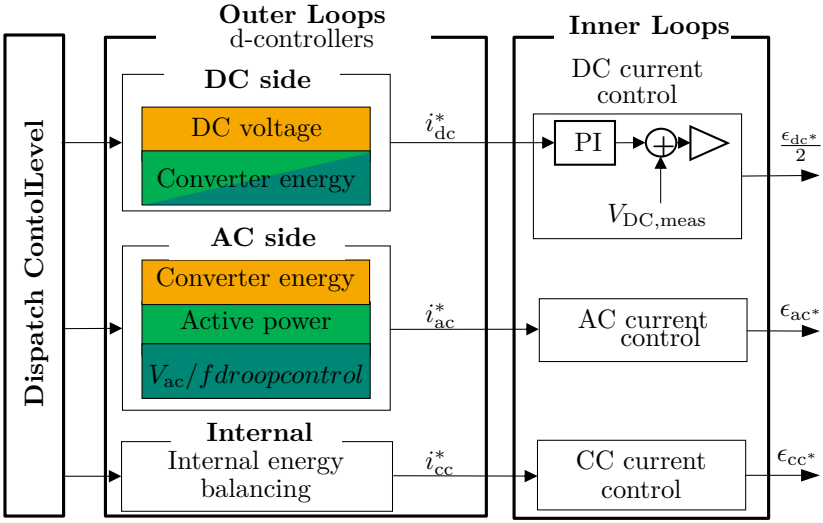


Figure 3.5: MMC cascaded control architecture (orange: V_{DC}, green: P, dark green: V_{AC}/f droop (GFM))[Ruf20]

DC-side fault interruption for system level studies. The implemented breaker topology is shown in Figure 3.6. The breaker consists of two switches the main switch responsible for interrupting the fault current and the residual current breaker, which is used to interrupt any leakage currents that are still running through the breaker through the energy absorption path. During the opening of the main switch, the energy absorption path will provide a counter voltage, to suppress the current to zero. The DCR is used to limit the rise of current, so that it stays within the opening limits of the DCCB The inductance of the DCR for the DCCB L_{BRK}, will is initially set to 300 mH to ensure continuous operation. However, the inductance value will be variable in the blocking investigation. The breaker opening time t_{DCCB} is based on available breaker designs and dependent on the investigation.

For the DC-side fault detection a simplified traveling wave detection is used, since fault direction and location are known in EMT-type simulation models. The detection is triggered by a DC undervoltage

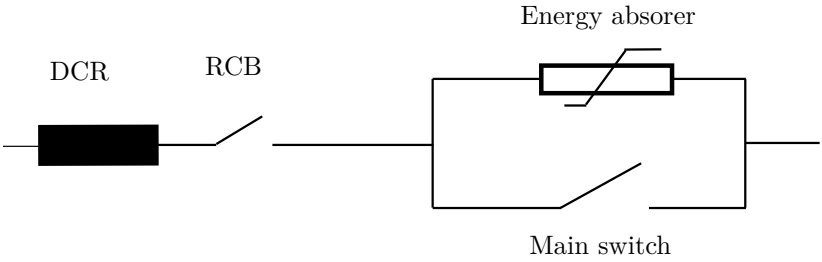


Figure 3.6: Schematic drawing of the implemented breaker topology [ZJ19b]

criterion $V_{\mathrm{DC,min}}$, set to 0.95 p.u., based on the lower voltage criterion of the dynamic DC voltage band [Cig16]. This detection criterion eliminates the parameterization of relays, such as current deviation, which are reliant on changing parameters such as the inductance value of the DCR [KDL25].

3.3 Cable modeling

Three different cable models are used within this research, i.e., one for the DC submarine cable and two for the AC connection of the OWPP depending on the distance between the WTGs and MMC. Generally, frequency dependent phase models are used for the DC and AC cables as these are the most accurate models available in EMT-type software [BB14]. If the line lengths become too short, which is the case for the interconnections between the WTGs, the frequency dependent models are replaced by PI-sections. For the submarine cables cross-linked polyethylen cables are used.

The parameters for the DC cable and AC cable are taken from [PRO16a]. The parameters and designs for the AC cables can be found in Appendix A.2 and for the DC cables in Appendix A.1.

4 OWPP and HVDC system energization

This chapter provides an in-depth analysis of the overall energization procedure of HVDC-connected offshore OWPP including energization of an onshore load. First, the energization of the OWPP is analyzed. Two start-up approaches are investigated for stability and system requirements. Second, a sensitivity analysis on the HVDC system energization is performed, determining required additional components or control adaptations. From the results, a set of requirements posed on the OWPP, the HVDC system and the onshore AC system are derived to provide recommendations for future offshore systems designed for black start. The full system design for the study is shown in Figure 4.1 with its components based on the system parameters introduced in Chapter 3.

This chapter is based on the publication: HVDC system energization via grid-forming offshore wind turbines: sensitivity analysis and technical requirements published in IET Renewable Power Generation [KDO23, KDO25].

4.1 Start-up methodologies

In the preliminary analysis, the benefits and drawbacks of all combinations of start-up methods for the HVDC link and the OWPP are discussed, and two methods are selected for further investigations. In total, this gives three distinct sequences to energize system under study (Table 4.1), which are applicable for future offshore systems. For the hard energization of the OWPP two start-up choices can be made, i.e., a synchronized option, where all turbines start simultaneously, and a sequential start-up, where start-up originates from a single turbine and the remaining part of the OWPP is started sequentially (Table 4.1, 1 and 2). The start-up for the HVDC system is identical for both options the offshore converter being energized in a hard start manner through a PIR. Since soft energization lacks a clear boundary between HVDC

and OWPP, it is considered only in a single investigation for OWPP and HVDC system (Table 4.1, 3).

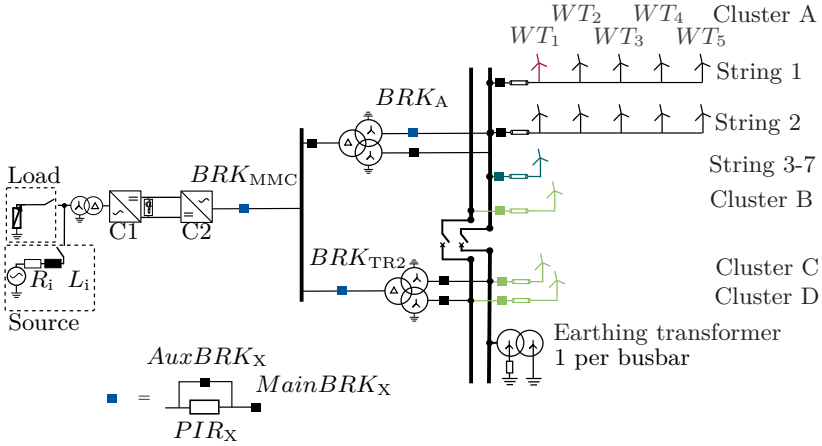


Figure 4.1: System overview for the energization study, red: Initial black started WTG, black: Single WTG, green: 25 WTG aggregation, light green: 35 WTG aggregation [KDO25]

Table 4.1: Start-up methods

System start-up	Start-up method OWPP	Start-up method HVDC
1	Hard energization (synchronized)	Hard energization of offshore MMC Soft energization of HVDC system
2	Hard energization (sequential)	
3	Soft energization	

4.1.1 Energization of the first WTG

The available grid-forming capabilities of each turbine directly depend on the energy available in the DC-link of the WTGs back-to-back converters, as well as the available wind for type-4 WTGs. To avoid a

high impact on the machine side or draining the DC voltage too quickly, an adequate capacitor in the DC-link or a battery storage, as studies like [HWZ23] suggest, should be used. The drawback would then be, higher costs for the turbines, as well as additional space requirements. Similarly, a large DC-link capacitor would be required. To achieve the requirements for charging the different system parts, the impact on the machine side is investigated (Figure 4.2). It is found that for the required grid-forming capability a larger capacitor is required, during the black start. This requires higher energy, either from the turbine generator or auxiliary systems to charge the DC-link upon the black start process. The final chosen DC-link capacitance is 0.15 F, enabling sufficient grid-forming capabilities, which would be higher than current state-of-the-art WTGs. This ensures sufficient decoupling and grid-forming capabilities throughout the start-up process. In this study, all WTGs are inherently black start capable to investigate synchronization transients between the WTGs. However, as shown in Figure 4.2a, the charging of the DC-link requires the machine side around 1 MW and subsequently, the energization of the WTGs requires similar power. Afterwards, since the power is shared between the turbines, the required power is less than 1 MW. As a result, with the provided design and start-up method, only the first turbine would be required to be black start capable; however, each turbine would require the same DC-link capacitance to ensure grid-forming capability throughout the process.

4.1.2 Offshore wind power plant energization

To investigate the applicability of each start-up method for the given test setup, a preliminary analysis is performed. In the analysis, the HVDC system is omitted, to investigate the influence of the AC-busbar setup depending on the start-up method. A full start-up sequence was emulated using this setup, while only the connection of the four subsystems through the transformers is shown. As stated in Section 4.1.1 two start-up methods can be considered for the OWPP: Sequential energization of all strings originating from string 1-WTG 1, or simultaneous energization of each subsystem with synchronization upon transformer connection (cf. Table 4.1). The analysis leads to the conclusion that a synchronous start-up is not feasible in the considered test setup and also

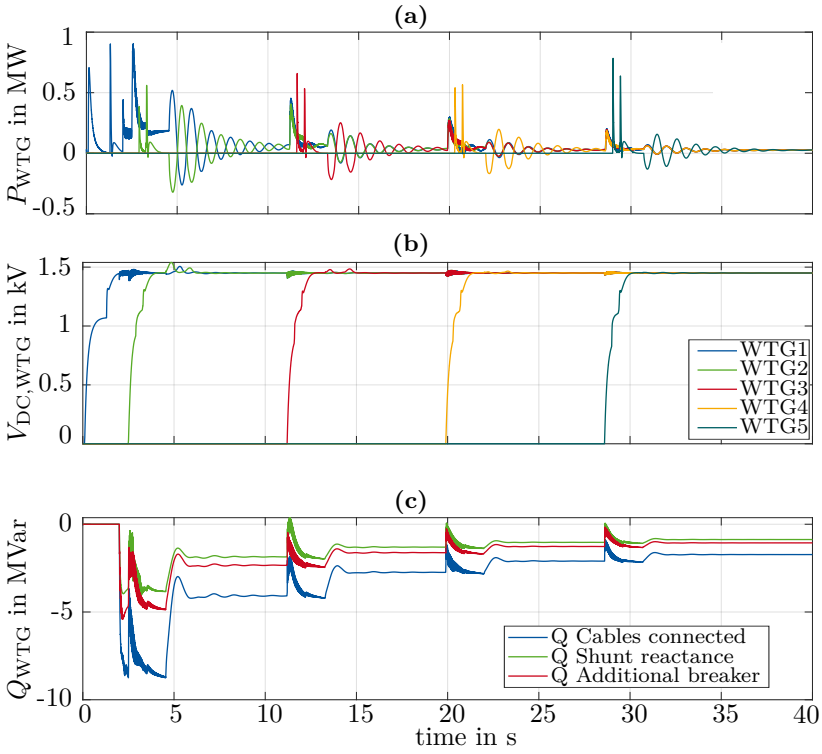


Figure 4.2: Charging of all downstream turbines via WTG 1. a) Machine side power; (b) DC-link voltage; and (c) Reactive power

might be challenging for real life systems. The results of the analysis showed that the transformer connection and the subsequent bypass of the PIR results in active power transients, leading to power transferred from Subsystems B-D into Subsystem A due to the difference in voltage and stronger individual grid-forming control from the aggregation. This is clearly visible by considering the voltage and power for subsystems A-D in Figure 4.3 (a) at $t = 5.3\,s$. This leads to the assumption that due to the different degree of detail and the resulting elongation of energization, a phase shift additionally to the visible voltage difference

occurs. Therefore, in a real-life application for a synchronized start-up, the phase angle and voltages would have to be accurately tracked and fed back to each of the WTG in order to avoid transients. Especially since a voltage difference of 2 kV leads to around 40 MW of power transfer. Additionally to the transients, the synchronized start-up leads to higher requirements on multiple turbines, since for each subsystem one turbine is required to be black start capable. As a consequence, the more stable but elongated sequential start-up sequence, here named sequential energization, is chosen for the investigations. The start-up originates from WTG1 in string 1 (cf. Figure 4.4, red) and subsequently energizes all WTGs of the string and the subsystem A. Via the PIR_{A}, the upper transformer TR1 will be energized via subsystem A in order to subsequently energize Subsystem B. Both Subsystems then in turn energize the lower transformer TR2 and the Subsystems C and D via PIR_{TR2}. Once all WTGs are in operation, and the inrush transients have decayed, the OWPP is operated in islanding mode and will remain in that state until the breaker $MainBRK_{\mathrm{MCC}}$ to the MMC is closed. It is assumed that each WTG is capable of black starting without external supply and synchronizes onto the phase angle set by the first WTG with the feed-forward loop described previously in Section 3.1.2 [KDO23]. This presents an alternative to the black start originating from one WTG in Section 4.1.1, where only one WTG is black start capable. For the PIR a resistance of 100 Ω with a pre-insertion time of 100 ms was chosen, providing sufficiently reduced inrush currents without adding a to large resistor.

4.1.3 HVDC system energization

As described in Section 2.3, the submodule voltage directly depends on the secondary side AC voltage and the number of submodules. The values calculated from (2.28) and (2.29) result in $V_{\mathrm{SM,pre,AC}} = 1.6\,\mathrm{kV}$ and $V_{\mathrm{SM,pre,DC}} = 1.1\,\mathrm{kV}$. Therefore, the voltage difference from the uncontrolled charging level to nominal submodule level is 20 % higher than in academic studies using 390 kV and 225 submodules, which could lead to a different transient behavior during energization [SGB19, JSS21a]. For the DC side, the charging level is around 50 %. As a result, the impact of the chosen values should be investigated and possible mitigations have to be taken to reduce the power requirement during

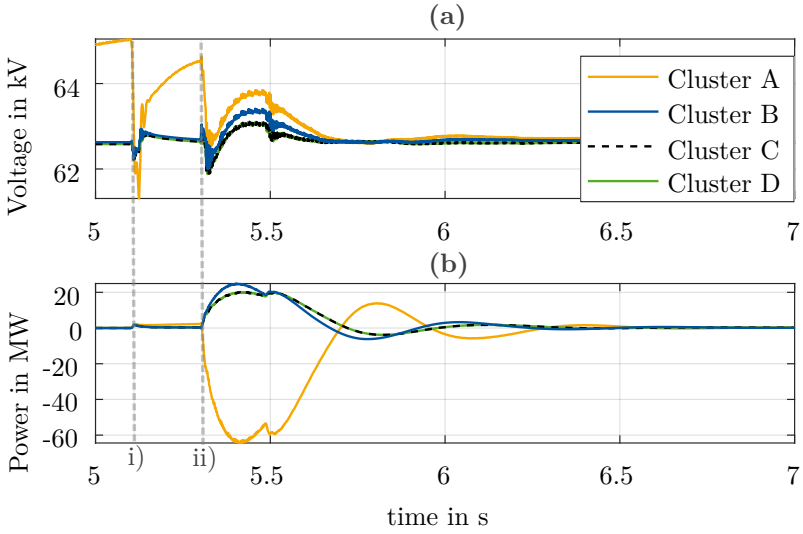


Figure 4.3: Transient behavior of subsystems A-D upon transformer connection and bypass of PIR (i) Connection through AC breaker ii) Bypass of PIR [KDO25]

energization for both converters [KDO23]. The HVDC system will always be started in a soft energization method (i.e. DC voltage ramp) to eliminate any DC-PIR, which otherwise would be required to charge the DC cables and during uncontrolled charging of the onshore MMC. To achieve the ramp the voltage reference for the submodules is reduced to the achievable 60 % ($V_{\mathrm{SM}} = 1.6\,\mathrm{kV}$) of the uncontrolled charging and ramped with different ramp values to 100 % ($V_{\mathrm{SM}} = 2.4\,\mathrm{kV}$). The aim of the ramp is to smoothen the transition to the control state, reducing the setpoint step for the PI-controller of the MMC-control. As a result, the power demand can be reduced significantly and improve the voltage stability within the OWPP. The soft or hard energization of the OWPP has however, an impact for the system design of the offshore converter. For the hard energization the PIR_{MMC} is required to eliminate the transients occurring during the uncontrolled charging of the offshore converter. It will be inserted during the whole charging process and its sizing will determine the active power peak occurring during the inrush into the offshore converter. For the analysis of the soft energization,

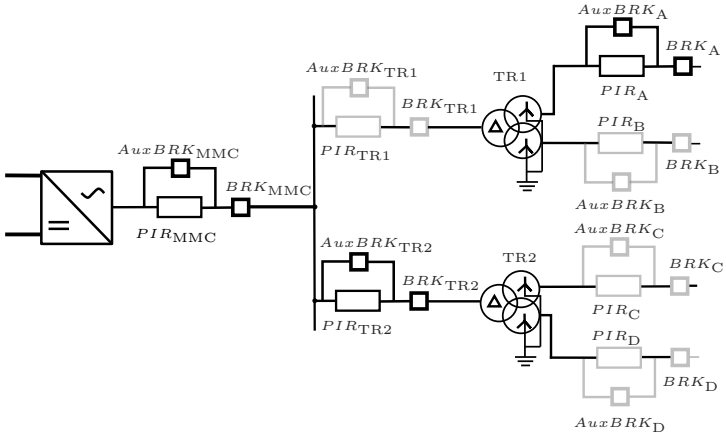


Figure 4.4: PIR placement in the offshore system, grey + black) Full redundancy, black) minimum PIRs for sequential hard start

the PIRs depicted in Figure 4.4, were eliminated and all breakers are closed from the start of the process. For the soft start it is expected that the voltage ramp used to energize the offshore converter, has a significant impact. Therefore, different voltage ramps of the OWPP will be investigated and analyzed. To allow for comparison between soft and hard energization, the soft energization ramp of the HVDC system will remain at one value for both investigations. Table 4.2 shows the required energization steps for the hard and soft energization. It becomes evident that the main difference between the two lies in the first three steps until the offshore converter is fully charged.

Table 4.2: Start-up methods

Step	Action: Hard Energization	Action: Soft Energization
1	WTGs are sequentially energized and operated in grid-forming mode	Closing of all breakers prior to start
2	Closing of $Main_{\mathrm{BRK,MMC}}$ uncontrolled energization of offshore MMC C2 via PIR_{MMC}	Start of voltage ramp-up of WTGs Simultaneous charging of MMC C2
3	Bypass of $\mathrm{PIR_{MMC}}$ and deblock of MMC C2 Full charging of MMC C2	Deblock of MMC C2 Full charging of MMC C2
4	Deblock of MMC C1 after uncontrolled energization	Deblock of MMC C1 after uncontrolled energization
5	Full submodule charging of onshore MMC C1	Full submodule charging of onshore MMC C1
6	Connection of the onshore load (soft energization)	Connection of the onshore load (soft energization)

4.2 Results - Hard energization

4.2.1 Energization of the offshore wind power plant

The OWPP is energized via a hard energization method, and the first subsystem (here: A) is used to sequentially energize all other parts of the OWPP. For short delays between turbine energization, voltage instability and inadequate sharing of reactive power occur due to WTG transformer saturation (Figure 4.5). In Figure 4.5, delays between turbine energization have been set to 12 ms, showing severe transients between consecutive breaker closings. To avoid WTG transformer saturation and ensure proper decay of the inrush transients, delays between

the turbine connections have been set to 1.5 s, resulting in a more distinguished startup, in a sense that the next turbine is connected after the inrush is fully decayed. The charging process of the WTG transformers and the subsequent sharing of reactive power is clearly visible in the bottom graph of Figure 4.6, showing the reactive power of the first turbine, without the synchronization transients interfering as seen in Figure 4.5.

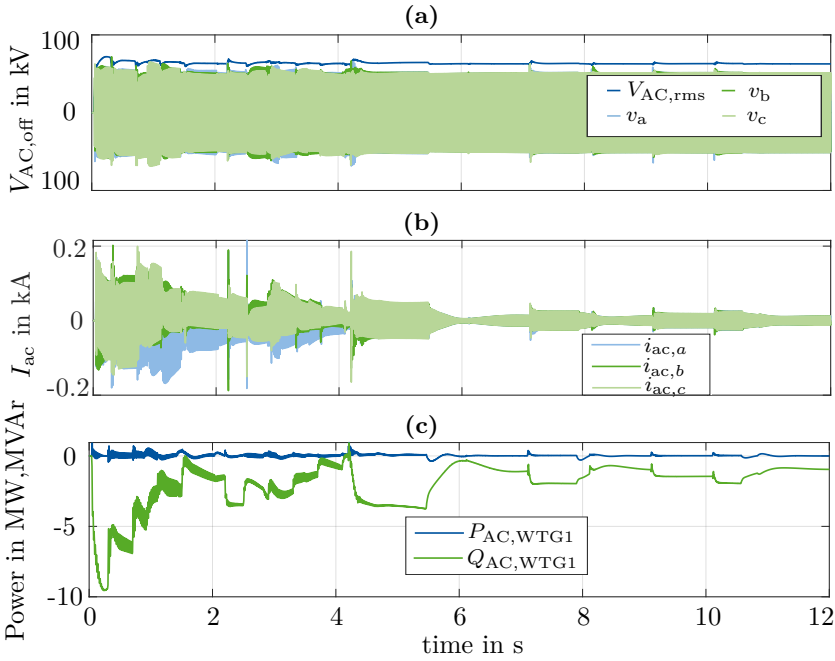


Figure 4.5: Start-up sequence of the OWPP with values of WTG 1[KDO23]

This leads to an overall higher system stability, especially for the energization of the first two strings, as seen in the voltage of WTG 1 (cf. Figure 4.6). The reactive power is continuously shared between the turbines, visible in the reactive power curves of WTG 1 - WTG 5, which approach identical values after initial synchronization and decay of the transformer inrushes. Each connection of the WTGs transformer

results in a jump in reactive power, due to the transformers provision of reactive power, with the synchronization of the reactive power between the turbines taking around a second after control activation (e.g., Figure 4.6, t in [2-17] s). The reactive power jump is gradually reduced with each connected turbine (e.g. Figure 4.6, t in [18-35] s), leading to an overall higher system stability. The connection of string 3 in subsystem A has a larger effect on the reactive power output compared to the previous string connections (cf. Figure 4.6, $t = 38$ s). This is due to the aggregation of the turbines to one single turbine representation, where also the cables are aggregated as parallel cable sections increasing the capacitance by a factor of 3, (cf. Section 3.1). As a result, reactive power has to be provided for 25 turbines and their corresponding aggregated cables simultaneously. In a non-aggregated system, the reactive power sharing continues in the same connection manner as seen at around 17 s with the connection of string 2, since each turbine and its cables are connected subsequently. The black start of the first turbine and energization of directly connected cables require the largest amount of reactive power due to it being the only connected turbine at the start. With the presented layout, the reactive power required to energize all the adjacent cables amounts to approximately 10 MVar until the second turbine is connected. On the LV side of the WTG, due to the inductance of the WTG transformer, this results in an approximately 8 MVar output requirement for WTG 1. As a consequence, WTG 1 must be able to output $Q_{\mathrm{AC,WTG1}} = 1$ p.u. at near zero active. This may be above turbine specifications even considering operating the system at voltages lower than $V_{\mathrm{GS}} = 1$ p.u considering the P/Q capability curve [EJT16]. However, the development towards 15 MW or larger turbines in the future significantly reduces this stress on the turbine since 8 MVar would only be 0.53 p.u., which should be well in the turbine specifications. Another mitigation method exists by using additional breaker between the WTG and the export cables in the strings, to connect turbines together prior to large cable connections or employing a shunt reactor into the offshore system (cf. Figure4.2c. As with the additional breaker or the shunt reactor, the reactive power can be reduced by 40 % with the additional breaker and by 50 % with the shunt reactor.

The energization of the three remaining subsystems follows a similar behavior to the connection of string 3, with the connection of subsystem D leading to a similar value required previously for string 3

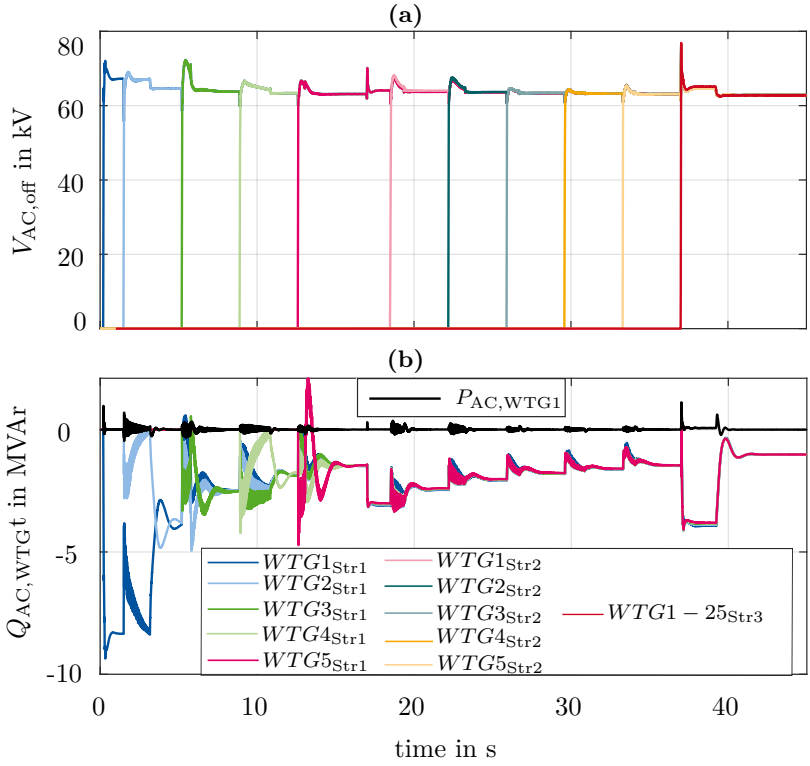


Figure 4.6: Start-up sequence of subsystem A, a) RMS voltage of the WTG at HV-side, b) Reactive power of the WTG at HV-side [KDO25]

(Figure 4.7b, t = 50 s). Additionally, the connection of the second transformer leads to the largest jump in positive reactive power during the inrush before decaying towards the values determined by the cables (Figure 4.7b at t = 55 s BRK for the transformer energization). Afterwards the two subsystems B and C are connected leading to even lower demands in reactive power as for subsystem D with the reactive power equally shared at about $Q_{AC,WTG1} = 1$ MVar after synchronization. At t = 70 s, a load is connected with an initial load of $P_{Load} = 150$ MW. The load is then increased in 50 MW load steps up until 300 MW. The WTG

follows the load steps quite quickly providing the new power within a few hundred ms.

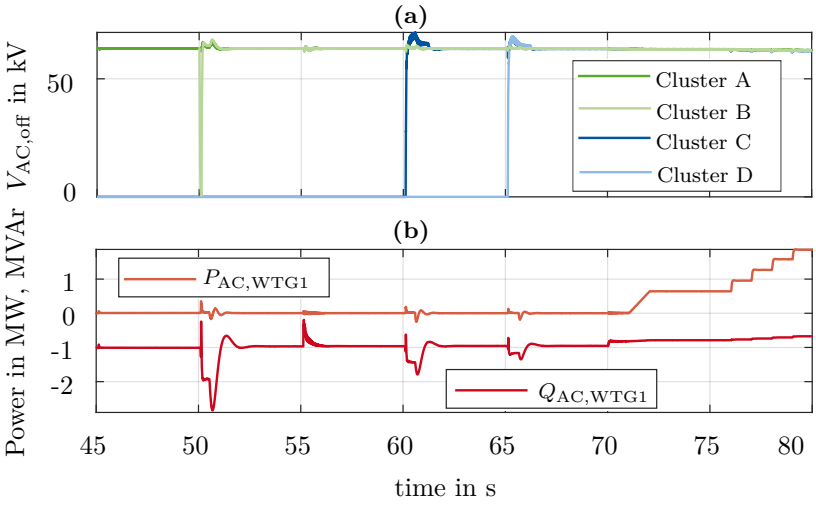


Figure 4.7: Start-up sequence of the subsystems B-D a) RMS voltage measured at the transformer of Cluster A-D, b) Active and reactive power HV-side WTG 1

4.2.2 Energization of the HVDC System

After the OWPP is energized, the charging process of the HVDC system is initiated. The figures in this chapter start at 0 s (for readability), assuming a fully started and stable OWPP (i.e., t > 12 s, Figure 4.8). The highest power demand, not considering supplying the load, occurs first during the uncontrolled charging of the offshore MMC being around 50 MW and then during its deblock for around 70 MW. This can be seen in Figure 4.8 (g) at t = 0 s for the uncontrolled energization and at t = 1.5 s for the deblock. The offshore MMC is energized via PIR_{MMC} and the submodules are charged passively for around 1 s (cf. Figure 4.1). Since the breakers within the HVDC system are already closed, the onshore converter is partially charged to 0.66 kV, as the DC voltage is not at

nominal voltage. This power is mainly dependent on the chosen PIR values (cf. [JSS21a]) and the system parameters in eq. (2.28). Larger PIR result in lower drawn power, but require a larger space and more weight on the offshore platform. Therefore, the PIR has to be chosen according to the trade-off of power vs. infrastructural requirements. After the deblock at $t = 1.5\,s$ the voltage of the submodules is ramped from its uncontrolled charging level at 1.6 kV to the desired voltage of 2.4 kV. After 2.7 s, the offshore MMC is fully charged and the DC voltage reaches 640 kV. This results in converter C2 reaching its passive charging level of 1.1 kV and the converter is deblocked. After the deblocking, the submodule voltage is ramped to the target value in the same manner as the offshore MMC reaching 2.4 kV after 4.6 s. The required power for the charging of the onshore MMC amounts to 50 MW. With the deblock signal, its grid-forming control is activated and the block load of 300 MW is energized [KDO23].

Sensitivity analysis of the charging process

Different aspects influence the energization process of the HVDC system, and especially the converter charging results in significantly different power demands of 50 MW 600 MW depending on the energization method used. To compare the energization process the resulting power demand for different approaches were investigated and displayed in Figure 4.9 for:

- PIR offshore and submodule voltage ramps offshore and onshore (Figure 4.8, 0.3 pu/s, 0.8 pu/s) (Blue + Magenta)
- Without coordinated transition from uncontrolled to controlled charging (green)
- Active pre-charging onshore (the onshore MMC is pre-charged in a block wise manner (orange) (cf. [JSS21a, LXZ15])

Without additional methods the active power by simply energizing the system large oscillations in power occur up to 600 MW (Figure 4.9 (green), t in 1.6 s and 3.5 s). This is due to the voltage control trying to achieve the voltage reference for the submodules as quickly as possible, leading to a peak in active power for the offshore and onshore converter. Within the other methods all achieve a significant active power reduction

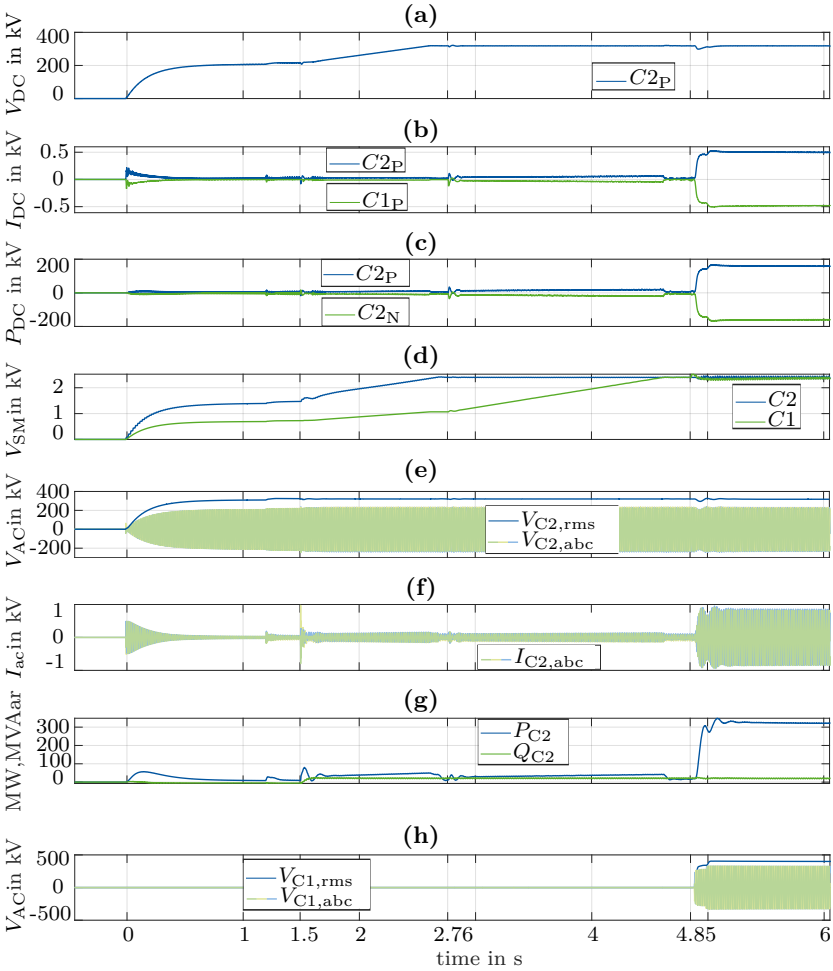


Figure 4.8: Overall energization process of the HVDC link: (a) DC voltage, (b) DC current,(c) DC active power, (d) Average submodule arm voltages (e) AC voltage secondary side, (f) AC current, (g) AC side power, (h) AC voltage [KDO23, KDO25]

compared to simply black starting the system, the method using the 0.3 pu/s ramp rates achieving the lowest power requirement [KDO23]. The AC-side PIR (cf. Figure 4.4 PIR_{MMC}) is connected throughout

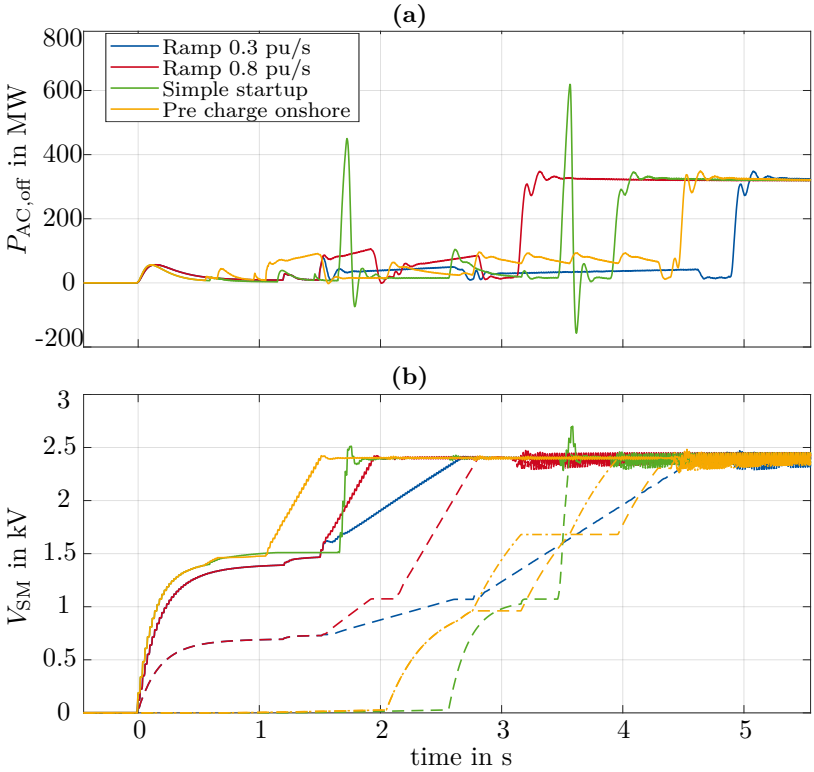


Figure 4.9: Start-up sequence of the subsystems B-D a) RMS voltage measured at the transformer of Cluster A-D, b) Active and reactive power HV-side WTG 1 [KDO25]

the whole uncontrolled charging of the offshore converter, leading to lower active power requirement and lower voltage drops for higher PIR during bypassing of the PIRs. In [JSS21a], where specific pre-insertion times (PITs) were used to bypass the PIR, it resulted in large voltage dips during bypassing due to the converter being not fully charged.

Contrarily, keeping the PIR inserted up until the full charge of the offshore converter reduces these voltage dips significantly, similar to the insertion time of 0.3 s proposed in [SGB19]. Small voltage drops of 1 kV occur (t > 0.3 s) for either of the PIR values (Figure 4.10 a)). Keeping the PIR inserted until the converter is charged to the voltage levels described in Section 4.1.3 leads to longer charging times for higher PIR values. This leads to PITs of 0.25 s for the 100 Ω resistor up to 0.65 s for the 400 Ω resistor, during which the PIR is required to dissipate heat for the duration accordingly. The effect of the PIR on the MMC reducing the instantaneous power required to charge the capacitance of the MMC significantly, especially for higher PIR (Figure 4.10 (c)). This results mainly due to extending the charging time constant τ, dependent on the MMC capacitance and PIR according to 4.1.

$$\tau = R * C \tag{4.1}$$

In order to investigate required cooling and down times of the PIR, the energy dissipated at the PIR should be calculated. To get an estimate of the required energy equation 4.2 can be used, with I being the root-mean square current flowing through the PIR [JSS21a]:

$$E_{\mathrm{PIR}} = 3 \int_{t_{\mathrm{BRK}}}^{t_{\mathrm{BRK}}+PIT} I^2 * R_{\mathrm{PIR}}\, dt \tag{4.2}$$

This accounts for an energy of approximately 7.3 MJ for the 100 Ω resistor up to 12.3 MJ for the 400 Ω resistor due to the extended wait time until the converter is fully charged. Therefore, the PIR should be designed depending on the available power to charge the offshore MMC, platform space and cooling.

4.2.3 Onshore load connection

For a block load energization, a U/f control is required for the onshore MMC. The voltage is ramped up to 400 kV to provide the power for the connected 300 MW load, as seen in Figure 4.8 (f,g). Soft starting the load avoids inrush transients, leading to higher system stability. Similar to the OWPP energization investigations, load steps are performed so

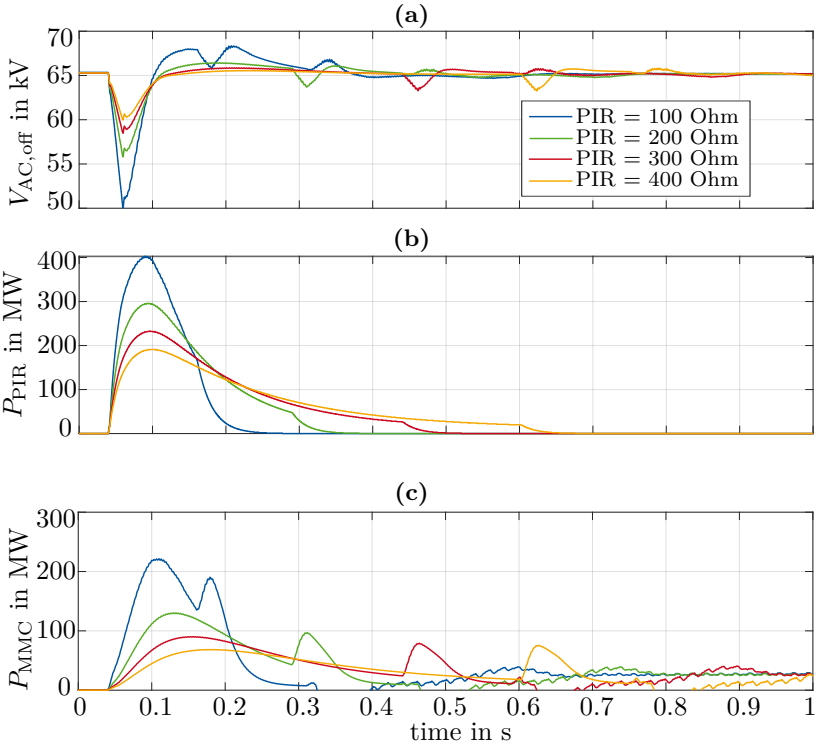


Figure 4.10: Load steps: (a) HV-side voltage WTG1 (b) Active power WTG1, (c) AC voltage onshore, (d) Active power onshore [KDO23, KDO25]

that the WTGs can follow these steps through the power transfer of the HVDC system (see Figure 4.11 at t = 7.5 s). The U/f control provides a stable onshore grid voltage. After 2.5 s, a load step of 190 MW is performed to test the response of the offshore wind farm. The OWPP can follow the load step almost immediately, but with oscillations to stabilize, mainly resulting from the machine side requiring it to adjust its power via the pitch control. A larger capacitance may dampen these oscillations [KDO23].

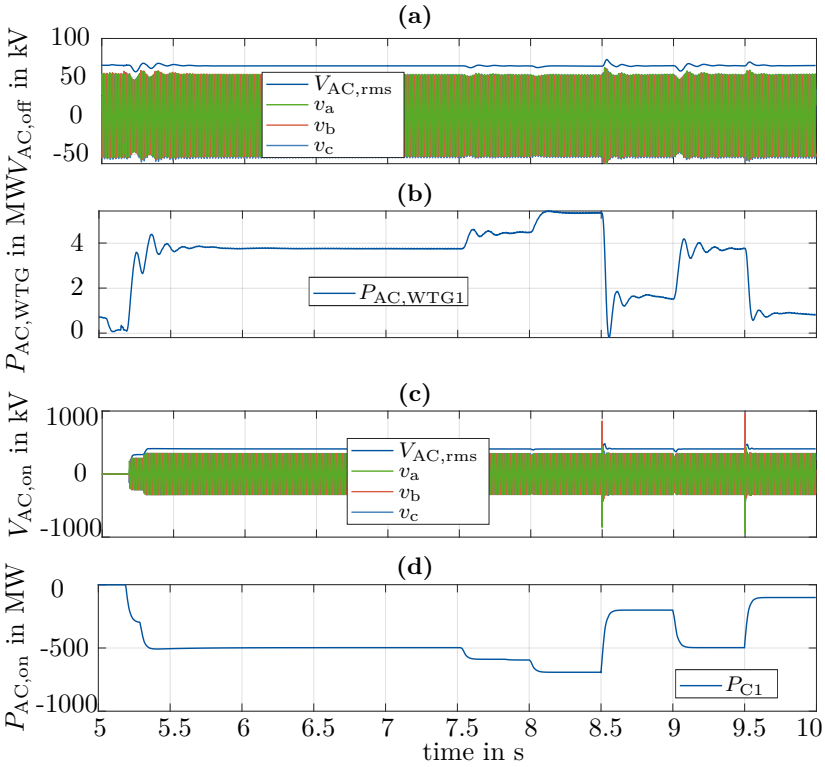


Figure 4.11: Load steps: (a) HV-side voltage WTG1 (b) Active power WTG1, (c) AC voltage onshore, (d) Active power onshore [KDO23, KDO25]

4.2.4 Synchronization to a pre-established AC System

As wind conditions are not always stable for the duration of the full black start fulfilling the requirement of black start provision for over 10 h, an alternative solution is the black start of the HVDC system up until the onshore converter when wind conditions allow, and to integrate the HVDC-connected OWPP into an already partially black

started system. To analyze the synchronization capabilities, the load from the previous cases is replaced by a three-phase source behind an impedance to simulate different grid strengths (30 GVA, 10 GVA, and 3 GVA) which energizes a 500 MW load prior to the connection of the onshore MMC. To avoid unnecessary transients upon breaker closing connecting the HVDC system to the black start grid a synchronization unit similar to the one described for the wind turbines in Section 4.1.2 is used. The voltage and frequency feed forwards are fed into the grid-forming control of the onshore MMC, and the phase angle of the voltage is adjusted accordingly. As a result, reduced power transients are present and can be even more reduced through the use of a smaller phase and voltage margin for synchronization. For all grid strengths under study, a synchronization with minor transients can be achieved with the desired power supply setting of 250 MW, with the rate of change after connecting controlled through the droop between the source and the investigated system. An increased grid strength leads to increased transient excursions of voltage and power, due to the control behavior working against the source (Figure 4.12). The transients in the active power, occurring with grid strength of 30 GVA, amount to 200 MW and must to be dissipated by the HVDC-chopper. The power set point of the converter then has to be chosen according to the available wind power. The reference values, therefore have to be transferred from the offshore system either through communication, droop cascade (i.e. P/f, V_{DC}/P, P/f offshore), or via accurate forecasting. For an integration into larger energized systems with multiple sources it could be beneficial to also use a VSM or similar grid-forming control for the onshore converter as well.

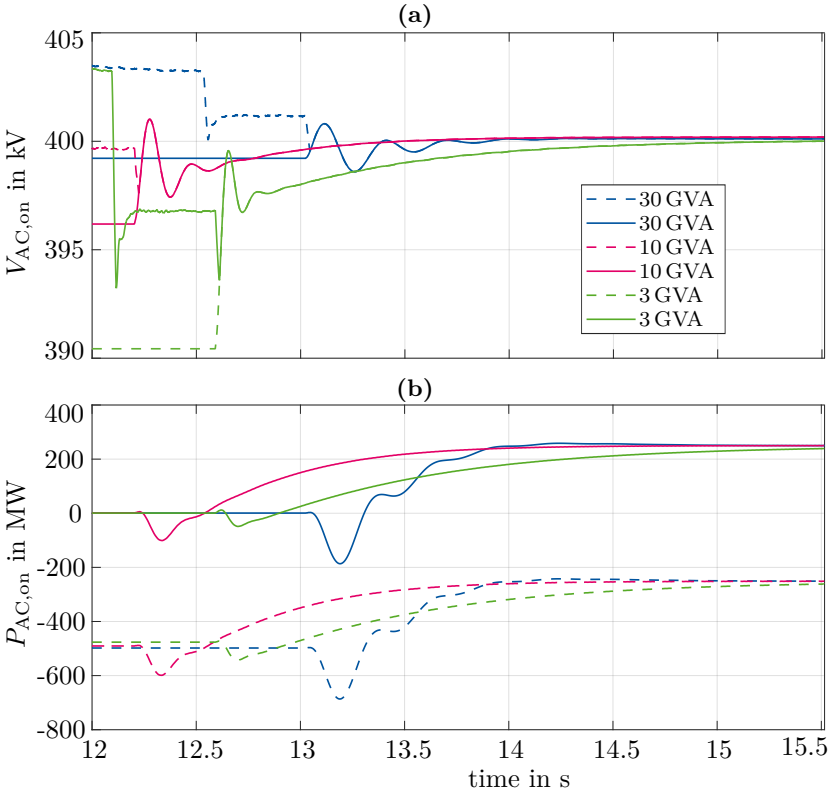


Figure 4.12: Synchronization with a grid source equivalent (dashed: source, solid: converter): (a) Onshore voltage, (b) Active power [KDO25]

4.3 Results - Soft energization

As previously discussed, the soft energization is a start-up alternative to the hard energization eliminating the PIR placed in the offshore system reducing overall component requirements. With the smallest voltage ramp of 0.2 pu/s, lower active power requirements can be achieved than with the hard energization (blue curve in Figure 4.13 at $t = 5.5\,s$). A steeper ramp leads to an initially higher active power peak, similar to the investigation performed for the DC-side charging (red and yellow curves in Figure 4.13, at $t = 5.5\,s$). The voltages in Figure 4.13a show that the transformers and with it the MMC, are smoothly energized without the need for a PIR. However, the deblocking of the offshore converter requires the largest active power of the overall charging process in accordance with the previous investigations. Nevertheless, it can be stated that a soft start can eliminate the PIRs while enabling a stable startup. The power requirement within the simulation accounts for a lower power requirement than the hard energization. However, as previously shown, the active power depends on the ramp rates used for the soft energization and PIRs used within the hard energization as well as the converter model for both. It should be noted that for the deblocking, the values from Section 4.1.2 were used, leading to the deblock only when the AC voltage reached its set value of 340 kV. A further power decrease could be achieved if deblocking occurs at a lower voltage level in the ramp of the OWPP.

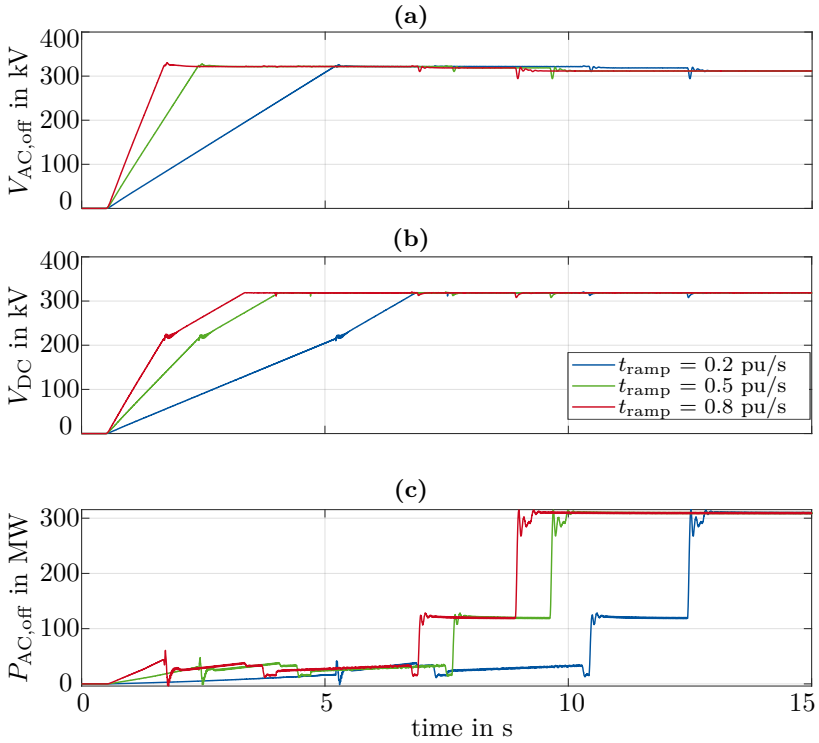


Figure 4.13: Soft energization of the overall system for different ramp rates: (a) RMS voltage at C2 (b) DC voltage at C2 (c) AC active power of C2 [KDO25]

4.4 Technical requirements and sensitivity analysis

This Section derives technical and functional requirements for black start through HVDC connected OWPPs from the previously discussed results.

4.4.1 Hard vs soft energization

Choosing hard or soft energization poses different requirements on equipment, start-up procedures, and testing capabilities of future OWPP-HVDC systems. The main advantage of a hard energization is that it provides a clear boundary between the energization of the OWPP and the HVDC system. Indeed, GFM WTG can remain in islanding operation until the energization of the HVDC link is initiated by closing the breaker at the offshore MMC. Furthermore, the auxiliaries required on the offshore platform could be charged beforehand through a tap on the busbar in front of the main breaker. As a result, testing and designing of OWPP and HVDC system for black start readiness can be done independently. The main downside of the hard energization is the requirement of three PIRs (ignoring redundancy for the other strings) to securely energize the system and avoid large active-power peaks due to inrush currents. The PIRs must be designed to allow for multiple consecutive black starts, requiring sufficient cooling. An alternative that was presented in [JSS21b] is the use of a virtual resistance control in the WTG control to reduce the inrush by voltage reduction. However, this control has to be tested for the setup described in this study, where the turbines are decoupled by the transformers. The other alternative, to eliminate all PIR, is to use the soft energization method studied in Section 4.3. This method leads to a lower active-power peak during energization compared to the hard energization. The downside of the soft start is the absence of a clear boundary between HVDC and OWPP system, due to the closed state of the breakers from the initiation of the black start process. This requires a coordinated black start/ master controller and fast communication between HVDC system and WTG controls. Furthermore, additional charging for the auxiliaries is required (i.e., diesel generator on the offshore platform) since otherwise the auxiliaries would be charged simultaneously with the submodules of the MMC, while in a hard energization the tertiary winding can be used. Furthermore, due to the lack of boundaries, fault detection and separation has to be desensitized to the system's low voltage to avoid total outage of the system during the start-up. While a detailed investigation on protection and fault scenarios during the start especially for the soft start, where out of scope within this investigation and should be investigated in the future.

As an overview, the identified pros and cons are listed in Table 4.3.

Table 4.3: Pros and Cons of Soft and Hard Energization

	Hard energization	**Soft energization**
Pro	• Clear interfaces between WTG, OWPP and HVDC system • Independent testing of OWPP and HVDC black-start capabilities • Operation at full voltage: Control and Protection adapted accordingly	• No PIR required, reducing platform costs (space and weight requirements) • Reduces transients • All PIR operate simultaneously, reducing requirements on a single turbine
Contra	• PIR required to limit transients during transformer and submodule energization • Transients put extra stress on system components	• No clear boundaries between OWPP and HVDC due to closed breaker (Master controller required to ensure all systems are ready for operation) • Separate energization of auxiliaries prior to start-up • Ensuring control capability and desensitizing protection for low voltage

4.4.2 Black start requirement for WTGs

Within this study, it is assumed that each turbine is capable of black starting and charging of its own DC-link. This requires the turbines to

have a synchronization unit with a feedforward control to synchronize to the voltage and phase angle of the AC offshore system. When using a sequential black start of the subsystems B-D, as performed in this study, not every WTG needs a black start capability (but still a grid-forming control) and could be energized by those turbines in subsystem A for the presented case. The WTG transformer is always charged via the already connected turbines to prove that the turbines can indeed be charged from the initial black start capable turbine and do not have to be black start capable themselves. The energy required to charge the DC-link is mainly dependent on the capacitor size used. Using no specific charging strategy for the DC-link within the study, for the chosen capacity the maximum power drawn is 1 MW, which suggests that the turbine could always be black started for any wind condition higher than the cut-in wind speed. The assumed power at cut-in wind speed of 3 m/s is 1 MW. To ensure a black start capability in any system configuration, each subsystem or each string should have at least one black start capable WTG.

4.4.3 Requirement on system design and modeling

As described in the simulation results (cf. Section 4.2.1), additional equipment or a specific system layout may be required to perform the black start. The length and design of the strings and their connecting cable play a crucial role due to the required reactive power to charge the cables. Depending on the size, the strings must be split by additional breakers and connected during the black start process to keep the reactive-power demand within the limits of the WTGs. Furthermore, the level of aggregation combined with the start-up strategy for the OWPP can lead to power transfers from the aggregated systems into the detailed strings, which eventually overload the turbines. While the phenomenon described in Section 4.1.2 occurs mainly due to a phase and voltage shift resulting from the start-up times due to aggregation, the effect should not be neglected for real systems. The required power for the energization of the HVDC system is largely dependent on the following factors: Submodule reference voltage and ramp rates, PIR at the offshore MMC combined with the AC voltage and the charging process for the controlled energization. As seen in Section 4.2.2, changing these factors results in largely different power requirements and should

therefore be adjusted accordingly when designing and modeling a black start capable system to achieve correct results [KDO23].

4.4.4 Voltage and frequency stability

Voltage stability during black start is mainly determined by the combination of breaker operation and transformer energization due to the initial high demand for reactive power due to cable energization. Additionally, to ensure a stable and fast black start, a pre-synchronization unit for each WTG is inevitable (cf. Section 4.1.1). Without pre-synchronization, the WTG transformer saturation and phase differences lead to an unstable system, resulting in a failed black start or high stresses on the WTGs and system components due to harmonics. A sequential energization compared to simultaneous energization avoids a required synchronization through the transformers leading to a higher system and voltage stability. With the elongated start-up, it can be seen (cf. Figure 4.6 and Figure 4.7) that the impact of cable connections, turbines, and transformers, on the overall system stability reduces gradually the more turbines are connected (i.e. large reactive power provision by a single or few turbines for the initial energization). Therefore, the black start imposes the highest requirements on the first turbines. Depending on the overall OWPP design and redundancy factor turbines could be rated according to their placement inside the OWPP. Currently, it is assumed that all WTGs have the same control and equal setpoints to ensure the stability. Further investigations with share of GFL WTGs or alternative GFM controls should be conducted to identify stability issues in alternative scenarios. Additionally, it should be benchmarked if the design for a black start capable system ensures conformity with network requirements such as the Verband der Elektrotechnik Elektronik Informationstechnik 4131 and the complimentary Forum Netztechnik/Netzbetrieb guideline for GFM-controlled HVDC systems [KDO23, VDE19, VF20a].

4.4.5 Onshore grid synchronization

Synchronization to a pre-established system is shown to be generally feasible even without a dedicated grid-forming control (Section 4.2.4). A synchronization with a feed-forward to the converter controls is required,

needing measurements on both sides of the connecting breaker. The power is shared according to the droop-settings of the converter, leading to the requirement that droop settings and wind availability must be monitored to avoid power demands exceeding available active power. Systems based on GFM WTG can be integrated at any stage of a black start, as soon as sufficient wind power is available. This reduces the requirement on the black-start process as a whole, because OWPPs do not have to be energized from the onshore system as in the current state of the art. As a result, OWPPs can contribute active power much earlier in future black start processes.

4.4.6 Required interfaces/ communication

Hard energization: Assuming all turbines are blackstartcapable, within the OWPP, the startup can rely purely on local measurements. The synchronization unit within the turbine control ensures a sufficiently stable AC offshore system upon connection (assuming a small connection margin). Only the large transformer connection has to be timed according to the required time for each subsystem energization to ensure that all turbines within a subsystem are active prior to connecting either via local measurements or existing communication channels. Via these communication channels, information such as the number of connected turbines, can be provided to ensure that the necessary power to charge the MMC is connected. A master controller can also achieve this functionality, provided that it receives all the start-up signals of the turbines as binary signals. Due to the islanding capabilities of the OWPP, communication has a very low speed requirement, impacting only the maximum black start time of the overall system. Soft energization: A voltage master controller as well as fast communication between offshore MMC and WTGs are required to ensure a simultaneous ramp up of the system to avoid power peaks or imbalances due to different voltage outputs during the start-up. Once the whole system is in operation, only a basic communication comparable to existing systems is required. Due to the nature of the grid-forming control and the resulting control operations of the MMC (i.e., also the DC voltage control of the offshore MMC), no communication is required to follow the power demand of the black-started load. If due to wind conditions the power cannot be met, indications through DC voltage or offshore underfrequency can be

used to trigger a load reduction onshore [KDO23].

4.4.7 Black start availability

Due to the close proximity of the WTGs within the OWPP, for a monopolar HVDC link, it can be assumed that the wind conditions are equal (with minor turbulent differences) throughout the entire OWPP, which results in an equal power available to each turbine [HN23]. Grid codes generally specify the black start availability (e.g., 90% provision in all blackout cases) and resiliency of supply (e.g., 72 h power provision after restart) as two black start requirements for power plants. For offshore wind the former is mainly dependent the power required for the energization process and the required power provision by the grid under the respective wind conditions in the specified time duration. It is shown that the highest active power peak occurs during the deblocking of the onshore MMC, drawing around 70 MW with the chosen PIR as shown in Figure 9. This power can be reduced further with larger PIR. For the soft start, the active power can be reduced even further depending on the ramp rate chosen for the OWPP. Considering 8 MW WTGs, this would require a minimum of 9 WTGs to black start the overall system at rated wind conditions just taking the power into account omitting transient stability requirements. For low wind conditions at a cut-in wind speed of 3 m/s, a power output of 1 MW is assumed resulting in a maximum output of the wind park of 120 MW. Taking into account the yearly wind power available offshore (cf. Figure 4.14), a black start at 3 m/s wind would lead to an availability of around 80 %. If a higher availability is required by the respective grid code a more conservative approach would be to use the HVDC-connected wind farm as a supportive unit during the black start process if wind conditions allow it and synchronize it to the grid as shown in Section 4.2.4. As a result, the HVDC connected OWPP can be black started at any time and remain in island mode until a connection is desired or required. Therefore, wind power can be delivered much faster than in the traditional approach where wind farms are generally connected much later in the restoration process.

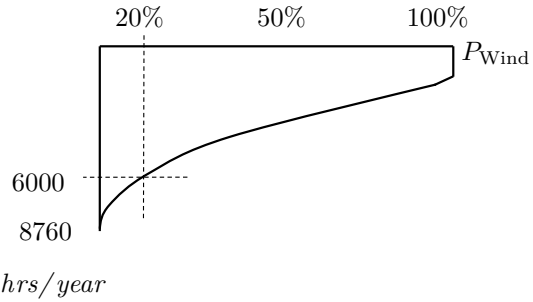


Figure 4.14: Yearly wind power in % per h/year [Cig15]

4.4.8 General discussion on WTG requirements

The steady development of WTGs toward higher ratings raises questions about availability and power requirements for future offshore systems. In the initial energization for the first WTG without any mitigation strategies, 1 p.u. of reactive power in relationship to the first WTG is required. While, for the turbine rating considered in this thesis, this necessitates mitigation strategies (see Section 4.1.2), larger turbine types could allow the first turbine to cover the entire reactive power requirement. Additional research is required because larger turbines also require cables with higher current capacity, depending on the OWPP design. The active power peak is 8.75 p.u. in relationship to the full OWPP capacity, for energizing the HVDC system. With higher turbine ratings, this greatly reduces the number of WTGs required at nominal power. However, independent of the turbine size, the cut-in wind speed of WTGs is typically around 3 m/s with a power output of about 1 MW before power increases to nominal power at approximately 11 m/s. If the total power of the wind park would not change, the amount of WTGs would the be reduced. Therefore, if the number of WTGs falls below the minimum required to meet the power at cutin wind speed, the availability would be reduced compared to the result in the previous section. Additionally, the active power peak is highly dependent on the HVDC and MMC design. If, for example, the submodule voltage changes or the system is build in bipolar configuration, the active power requirement could equally affect the availability, depending on the WTG

rating.

4.5 Conclusion

Black start of HVDC-connected OWPP can be achieved by fulfilling a set of technical requirements, of which the most important are black start availability, black start capability of the first turbine, and energization method. The time-domain simulations, including all details of the energization process, show that for both soft and hard energization, the energization of the HVDC link poses the largest active power demand. The hard start requires a minimum of one turbine to be black-start capable. For soft start, it is recommended that all turbines are black start capable to provide sufficient voltage stability. By contrast, soft start poses less demands on active and reactive power compared to hard start. Especially, the reactive-power demand, which is design-relevant for the hard energization, can be neglected for the soft energization. It was shown that to achieve accurate results, the converter model and charging process should be modeled in detail. In future work, alternative deblocking sequences can be developed to achieve lower active power requirements, especially for the case of soft start.

5 Post DC-side fault HVDC system energization

This chapter evaluates the reenergization of the HVDC system after a DC-side fault, to provide fast and efficient return to operation in future MTDC systems. The focus lies on the faulty zone of the in a partially selective protected MTDC system. Compared to the black start, the system state can differ depending on the fault isolation. Therefore, it is required to analyses these states in combination with different energization methods i.e., hard and soft energization.

Section 5.1 describes the proposed energization methodology, focusing on each of the distinct steps of offshore converter energization, system energization and return to operation. In Section 5.2 the methodology is tested with EMT simulations and evaluated based on the previously defined evaluation criteria.

This chapter is based on an unpublished manuscript that had been submitted for publication before this dissertation was made publicly available [KHL25].

5.1 Fault clearing and energization methodology

5.1.1 Fault isolation

Within the faulted zone (Figure 5.1, grey), the fault has to be cleared via the AC circuit breaker. Due to the fault and its subsequent current increase caused by the capacitive discharge of cables and submodules into the fault, the offshore converter C2 blocks after its over-current protection threshold is violated. After blocking, the converter acts like a diode-rectifier with the fault current contribution consisting of the fault current provided by the OWPP. The offshore system experiences a voltage drop due to the current contribution.

In today's systems this would lead to a shutdown of the OWPP since the connection to the offshore converter is lost. Therefore, the system would be required to be restarted either from the onshore AC-grid or from the neighboring HVDC system, depending on the fault location [Nor25]. A restart from the onshore AC-grid would put additional stress on the system already being impacted by the fault and loss of active power. A restart from the neighboring DC-system, requires additional equipment at the DCCB in form of a PIR to reduce the inrush currents into the de-energized system upon DCCB closing. This would increase the weight and cost of the offshore platform. Additionally, restarting the OWPP is a lengthy process, in which the onshore system has to provide power to the HVDC system for energization rather than receiving power.

By changing the control to GFM-controlled WTGs, the WTGs have to sustain a low-voltage ride-through (LVRT) until the AC circuit breaker (ACCB) opens. After the ACCB opens, the WTG can stabilize the offshore voltage and remain islanded, until the fault is cleared and the reenergization process can be started. During the fault isolation process, the active power output of the WTGs is reduced to zero. After the fault current is decayed, the fault can be isolated via the DC disconnectors (Figure 5.2, green). Afterwards, the offshore AC breaker can be closed and the system is reenergized from the OWPP. Therefore, the additional burden on the AC-system can be eliminated.

5.1.2 Converter energization

For the restart of the offshore MMC, the two start-up methods discussed in Section 2.3, hard and soft energization are investigated. After fault isolation, the first step is to energize the offshore MMC. The submodule charging of the MMC can be split into two stages, that need to be investigated independently. The uncontrolled (submodules are in blocked state) and the controlled (converter control is active) charging phase (cf. Figure 5.2). Both options are generally refereed to as the soft or hard energization respectively. Within the hard energization, the ACCB is closed immediately after the system stabilizes again. Due to the aforementioned partial discharge and two charging stages, the submodule voltage can result in two states. If the voltage was lower than (2.28), the submodules will be charged to the theoretical maximum

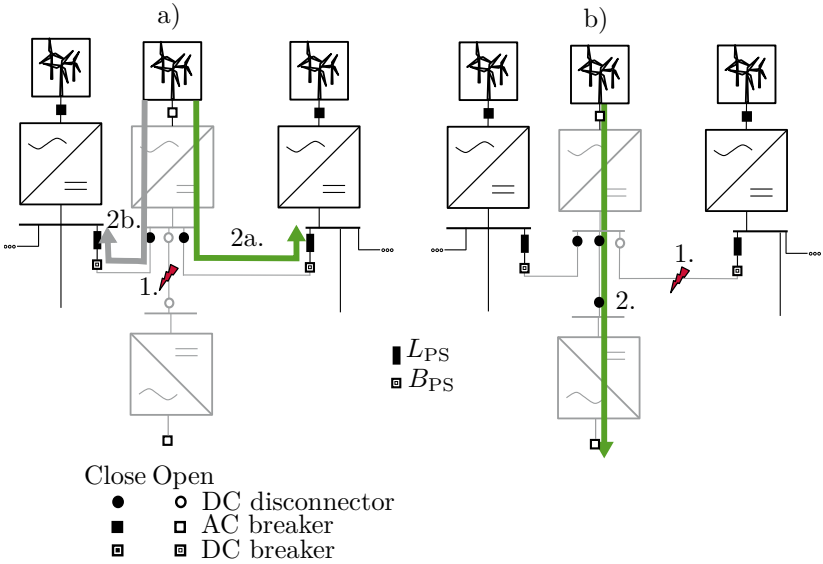


Figure 5.1: DC-side fault isolation (1.) and possible restoration (2.), a) Fault on onshore connection, b) fault on interconnection [KHL25]

of $V_{SM,pre,AC}$. If the submodule voltage is higher than the theoretical maximum, the submodules retain the voltage and are energized from the higher value $V_{SM,pu}$ (cf. Figure 5.2, orange). In that case, the charging will be mostly dominated by the DC-cable capacitance.

Based on the equation for the energy of capacitors, the energy required to charge the submodules and the DC cables can be derived and, from it, the resulting activepower demand can be estimated.

$$E_{SM,tot} = \frac{1}{2} C_{SM,tot} {V_{SM}}^2 \tag{5.1}$$

$$P_{SM,charge} = E_{SM,tot}/t \tag{5.2}$$

To increase the charging time and flatten the active power peak a PIR can be used. The PIR is inserted with the closing of the ACCB and bypassed as soon as the value for $V_{SM,pre,AC}$ is achieved. While for lower submodule charges the PIR can be beneficial. For charges higher than

$V_{\mathrm{SM,pre,AC}}$, it could potentially be omitted.

Instead of increasing the time constant by integrating a PIR, the voltage can be reduced interconnecting the components at low voltage. Compared to the black start scenario, the OWPP is already at nominal voltage, requiring a ramp down of the voltage prior to closing the ACCB (Figure 5.2, blue). Similar to the hard energization, the submodules will be gradually charged to $V_{\mathrm{SM,pre,AC}}$ for lower remaining voltages and kept constant for higher voltages, while simultaneously charging the DC system.

Prior to deblocking, the reference voltages for the submodules are adapted to the current voltage states to avoid control interactions or fast charging curves, enabling controlled energizing the system (cf. Figure 5.2, pink). Once the MMC is deblocked, the reference values are gradually increased to 1 p.u., achieving a smooth charging curve for the submodules and the DC voltage. Afterwards the remaining system can be energized depending on the fault location.

5.1.3 System energization

Fault L1-2

For faults on the export line to the onshore system (cf. Figure 5.1 a), restarting the the full system and transferring power via MMC 1 is impossible. Depending on the wind conditions, the reenergized MMC 2 can be reconnected to the healthy part of the MTDC system, which remained in operation to re-establish the power flow. To achieve a stable connection, the DC voltage should be within a 1 % margin on either side of the DCCB prior to closing. Therefore, the voltage is measured on either side of the breaker and the difference is added in the control loop for the DC voltage reference. Once the required margin is achieved, the DCCB is closed and both OWPPs can provide active power to the onshore system. If the pre-fault power is to be achieved, the setpoints of the onshore converter MMC 3 would have to be adapted (cf. Figure 5.3).

Fault L2-4

For a fault on the interconnecting line between the systems (cf. Figure 5.1 b), the system can be restarted as a point-to-point link. The onshore converter is charged via the offshore converter. When the DC system is energized via the offshore converter increasing the DC voltage, the submodules of the onshore converter are charged according to (3.4). Identical to the offshore charging the final charge is dependent on the post-fault voltage being higher or lower than $V_{\mathrm{SM,pre,DC}}$. After the uncontrolled charging phase of the onshore converter, being energized with a soft energization due to the voltage ramp, the reference values for the control are then adapted to either the value in (3.4) or the current state of charge. After the onshore MMC is deblocked, the AC voltage is established. Once the onshore voltage is stable, the system can be reconnected to the onshore AC grid. For that the voltage and phase difference between grid and converter are measured and the difference fed into the converter control (cf. Figure 5.3). That way, the converter control can match the grid voltage and phase angle to avoid transients or in the worst case a full shutdown due to phase opposition. After reconnection, the active power flow is reestablished.

5.1.4 Evaluation criteria

The evaluation criteria are are based on system values, that are influenced by the different system states.

- $P_{\mathrm{AC,off}}$: The active power during each of the phase of the startup, is an indicator, to determine the requirements for components, control and available wind power. The active power will be shaped by the PIR sizing, voltage ramp and the remaining submodule voltage.
- $V_{\mathrm{AC,off}}$: While, the OWPP, once disconnected from the MMC is an islanded system, the LVRT and voltage ramp is compared to current grid code requirement.
- $t_{\mathrm{P,AC,rec}}$: The total time required for the system to return to 90% of the pre-fault power transfer.

- V_{DC}: The DC voltage plays a major role during the re-connection of the healthy with the faulty system after the fault on L1-2, to reduce requirements on the DCCB during re-connection.

5.1.5 Offshore MMC re-energization

Independent of the fault location, the islanded OWPP first has to re-energize the offshore MMC. As described in Section 5.1.2, three sensitivities will have a main impact on the energization behavior. For the submodule voltages three levels 0.3 p.u. (lower than the uncontrolled voltage level), 0.6 p.u. (similar to the uncontrolled voltage level) and 0.9 p.u. (close to full charge) are investigated. The submodule charge is combined with the hard and soft energization. For the hard energization unlike the black start no PIR is considered to better visualize the impact of the remaining charge [KDO25]. Considering (5.1) and the given ratings in Table 3.2 an estimate on the required power at 0.3 p.u. and a total amount of 1800 submodules can be calculated

$$\begin{aligned} E_{\mathrm{SM,tot}} &= \frac{1}{2} 0.085\,\mathrm{F} \cdot (1.6\,kV - 0.72\,\mathrm{kV})^2 \cdot 1800 \\ &= 59.24\,\mathrm{MJ} \end{aligned} \tag{5.3}$$

with a charging time of around 150 ms this would result in an active power of 395 MW. However, this value can only be seen as estimate since the inductance values and cable charging are neglected.

$$P_{\mathrm{SM,charge}} = 59.24\,\mathrm{MJ}/150\,\mathrm{ms} = 395\,\mathrm{MW} \tag{5.4}$$

For the soft energization, three different ramp rates of the offshore voltage $V_{\mathrm{AC,off}}$ 5 p.u., 1 p.u. and 0.5 p.u, for which the voltage will be ramped up from 0.1 p.u. to 1 p.u.

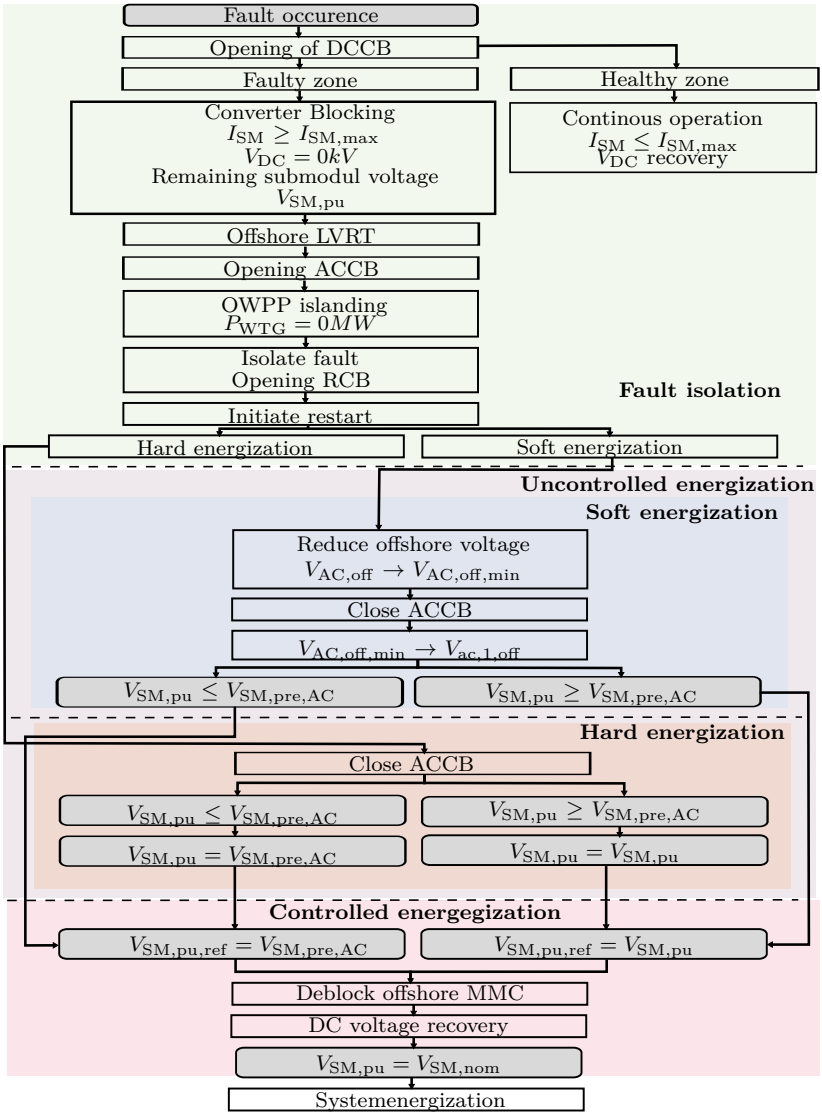


Figure 5.2: Flow chart of the restoration process [KHL25]

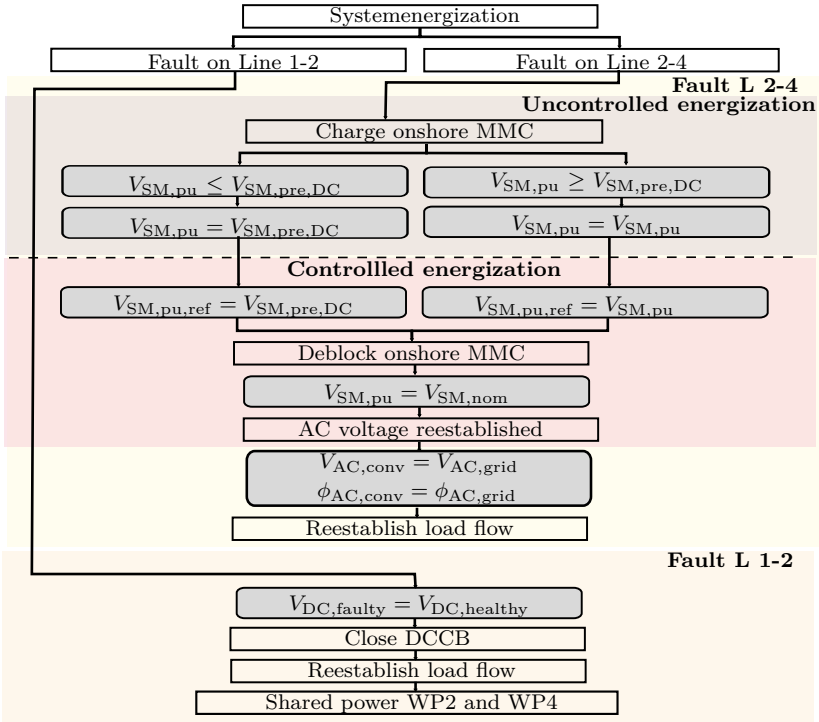


Figure 5.3: Flow chart of the restoration process [KHL25]

5.2 Analysis of the different scenarios

5.2.1 Fault isolation

After fault occurrence, the DCCB opens isolating the faulty zone from the healthy zone, with the healthy zone continuing operation. In the faulty zone, the offshore AC voltage drops to 25 kV until the converter blocks (time depending on the submodule voltage Figure 5.4a t = 0.15 s,0.2 s,0.21 s for 0.9 pu, 0.6 pu, 0.3 p.u. respectively). The offshore voltage remains low (due to the current contribution) until the ACCB opens at t = 0.25 s, 0.3 s , 0.31 s (Figure 5.4a. With the ACCB opening, the offshore voltage increases to 75 kV (Figure 5.4, t = 0.2 s). The voltage settles to 66 kV, after WTG DC-link voltage fully stabilizes, with the machine side power adjusted to the zero active power output (Figure 5.4d, t = 0.1 s - 0.8 s). Overall, the DC-link, sees a disturbance within its limits during the fault, with the DC-link voltage varying between 1.4 and 1.5 kV. The offshore voltage during isolation procedure remains well within the LVRT curve defined in [VDE19], in which a low voltage has to be sustained for 150 ms and returned to 0.85 p.u. within 1.5 s (Figure 5.4a).

5.2.2 Offshore MMC re-energization

Depending on the remaining submodule voltage and start-up method (soft or hard energization), the uncontrolled charging process of the MMC shows significant different behavior (see Figure 5.5 a)-d)). For the hard start without a PIR, the submodule charge has a large impact on active power peak, as well as offshore AC voltage dip. The voltage dip for the lowest submodule voltage of 0.3 p.u. is 20 kV larger than for 0.9 p.u. in which the voltage only drops to 60 kV (cf. Figure 5.5, right a) t = 0.9 s, 0.98 s, 1.01 s). The connection at the lowest submodule charge leads to a power demand of 380 MW, while with the highest submodule voltage around 190 MW. Even though the relative voltage difference between the submodules is identical, the active power difference between 0.6 p.u. and 0.9 p.u. is only 10 MW, while for 0.3 p.u. it is almost double. This is due to the pre-charging value $V_{\mathrm{SM,pre,AC}}$, to which the submodules are charged. While for 0.9 p.u., no charging of the submodules is required and no deviation in submodule voltage can be seen, at 0.3p.u. an

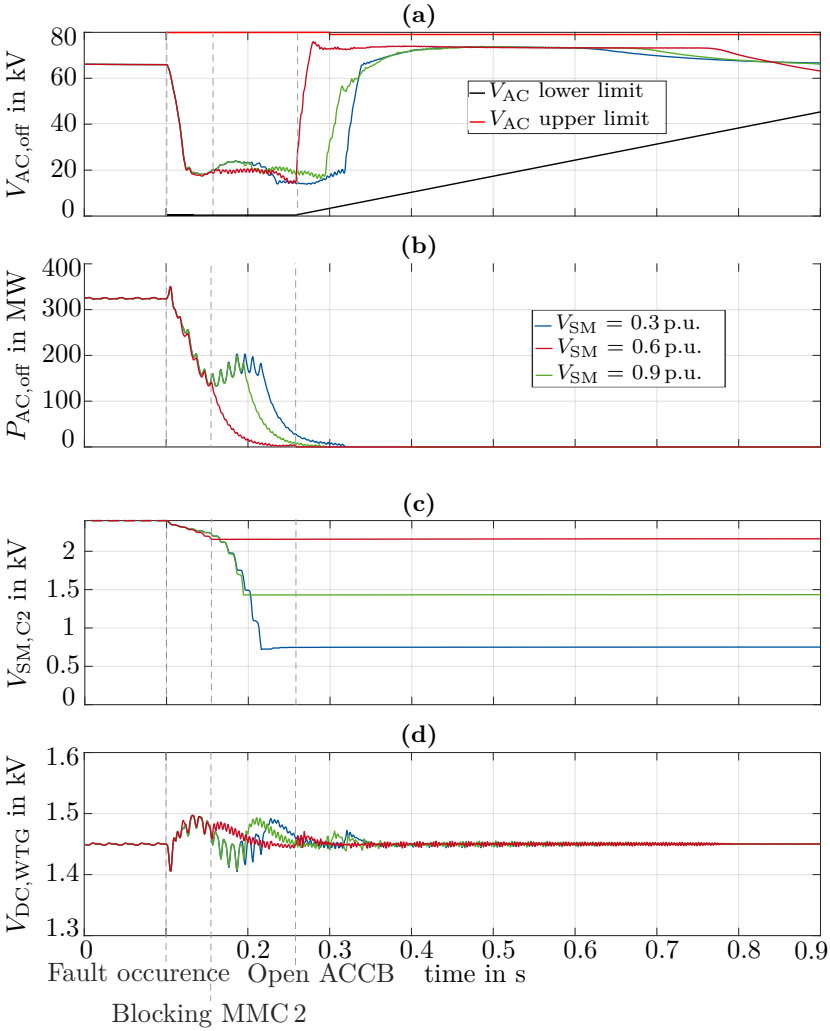


Figure 5.4: Fault isolation (a) Offshore voltage, (b) Active power, (c) Submodule voltage (d) WTG DC-link voltage [KHL25]

increase of more than 50 % is required to achieve the specified level (

Figure 5.5,c) t = 1.1 s). For the higher submodule voltages, the impact on the DC-link of the WTG is comparable to the behavior during the fault occurrence with the voltage drop being 0.05 kV larger. This warrants that no PIR is required for the system restart at submodule voltages close or above the uncontrolled charging level, since system impact is relatively low, and the active power requirement is much lower than the pre-fault power. However, for the lowest submodule voltage, the peak is higher than the pre-fault power requiring a PIR to reduce the transient. With a PIR of either 100 Ω or 300 Ω, the peak can be significantly reduced to 180 MW and 100 MW respectively (Figure 5.5 b) t = 1.1 s). Additionally, the impact on the DC-link can be reduced, from being right at the under voltage limit of 1.3 kV, to 1.4 kV (Figure 5.5 d) t = 1.1 s). While for all cases the PIR shows a positive effect on the system behavior, the effect on active power damping and offshore voltage dip decreases for larger PIR. Taken together, and given that fast converter blocking tends to preserve high submodule voltages, a PIR is likely unnecessary except at very low submodule voltages.

Compared with the hard energization, the soft energization can reduce the maximum active power required even further (cf. Figure 5.5, left b)). Right after the voltage settles back to 66 kV after fault isolation, the offshore AC voltage is reduced to zero, to close the ACCB at 0 kV (cf. Figure 5.5, left a). Since the ramp down shows no impact on either of the presented system values, the voltage ramp down, could always be performed at the maximum permissible rate. At a high remaining submodule voltage of 0.9 p.u. with the ramp rate of 0.5 p.u., the max power peak is around 25 MW (cf. Figure 5.5, t = 5.5 s). However, the start-up time is increased by 4.5 s compared to the hard energization. For lower submodule voltages the difference in active power becomes larger between the ramp rates different between 150 MW, 50 MW and 25 MW at 0.3 p.u. submodule voltage. This shows that for all ramp rates the active power requirement lies within the capabilities of the WTG, and shows almost no impact on the DC-link voltage, with the largest deviation being only 0,02 kV for 10 p.u./s at 0.3 p.u. (cf. Figure5.5 d)). The difference between ramp rates at 0.9 p.u. is very small, justifying a high ramp rate for high submodule charges, since it increases the restart time by 1.5 s, while the power is almost identical. Overall, the soft start enables a fast and stable system recovery, at the cost of restart speed. Therefore, the restart can be especially beneficial for low wind

conditions.

Overall, the soft energization shows higher stability and a much smaller impact on the WTG during the startup compared with the hard energization. However, if a high remaining submodule voltage (such as 0.9 p.u.) is expected, the hard start has only a minor worse performance but can bring the system back to operation much quicker without the added complexity of ramping down the offshore voltage. For the worst case scenario i.e. a depletion of the submodules to 0.3 p.u. or lower prior to the restart, the soft start is the preferred start up method. Within the soft start for 1pu/s and 0.5 p.u./s the active power requirement is less than half that of the hard start with a PIR of 300 Ohm. The soft start ensures, that with the cut-in wind speed of the WTG a restart is always possible.

5.2.3 Results for fault on L2-4

After the offshore converter is charged past the uncontrolled stage it can be deblocked and the DC system fully energized (c.f. Figure 5.2, (3.3)). From this stage onward, the energization behaves identically, regardless of whether soft or hard energization was performed previously, except for the time difference (c.f. Figure 5.2). Therefore, the startup will be only compared based on the different submodule voltages (Figure 5.6).

Once the voltage level in (3.3) is achieved, MMC 2 is deblocked to return the system to nominal DC and nominal submodule voltage (Figure 5.6c, t = 1.9 s, 2 s). Due to the adjusted submodule reference values depending on the remaining voltage level (c.f. Figure 5.2), the active power peak of around 100 MW is similar but the overall energy required reduces based on the submodule voltage. Therefore, at 0.9p.u. the charging only requires around 100 ms while for the other two around 300 ms. Since for the onshore converter 0.6p.u. and 0.9p.u. are higher than the specified value in (3.5), only 0.3p.u. requires additional charging leading to a slightly longer energization than for 0.6 p.u (Figure 5.6c, t = 2 s - 2.5 s). Once the nominal DC voltage is reached, MMC 1 is deblocked leading to an identical active power peak of 90 MW, slightly lower than for the offshore converter (see Figure 5.6b, and Figure 5.6c, t = 3 s). Similarly to the offshore converter energization, the charging time is dependent on the submodule voltage, due to the different energy levels. After MMC 1

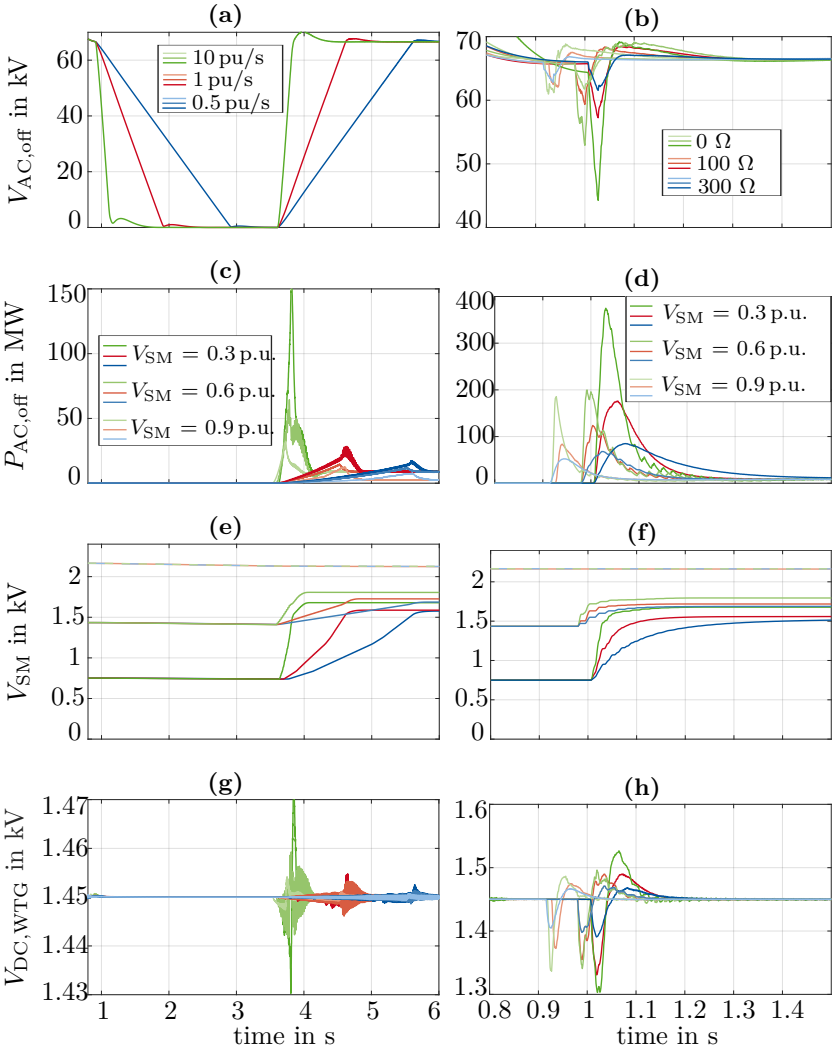


Figure 5.5: Soft (left) and hard (right) energization of MMC 2 (uncontrolled charging) ab) Offshore voltage, cd) Active power, ef) MMC 2 submodule voltage, gh) DC-link voltage [KHL25]

is fully charged, the power flow with the onshore system is reestablished. For the WTG, the controlled charging processes of the offshore and the onshore submodules only lead to minor transients in DC-link voltage. The largest dip occurs once the active power is reestablished, with a dip to 1.4 kV, since the machine side has to adapt to the new power flow (see Figure 5.6b and Figure 5.6c, t = 3.5 s). The dip can be adapted by the chosen onshore active power ramp/droop constants of the MMC control. The overall start-up time for the hard energization to return to full-pre fault power is $t_{\mathrm{P,AC,rec}}$ 3.4 s, 3.8 s and 4 s for 0.9 p.u., 0.6 p.u. and 0.3 p.u. respectively. For the soft energization this time would increase by an additional 4 s.

5.2.4 Results for Fault on L1-2

Since the offshore MMC energization is identical for both fault cases, for this investigation the recovery after 5 s is shown. After the partial system of MMC 2 is energized, the reconnection sequence with the healthy system can be initiated. Due to both parts of the system being in full operation, there are no transients visible due to the close matching of the DC voltage (cf. Figure 5.7c t = 6.15s). After the DCCB is closed, the OWPPs adapt to the new load flow sharing the power between each other each contributing 150 MW. The power adjustment leads to no differences in the DC-link voltage of the WTGs (Figure 5.7b). The power adjustment has a minor impact on the offshore AC voltage of MMC 4, increasing from 66 kV to 66.25 kV (cf. Figure 5.7a t = 6.15 s).

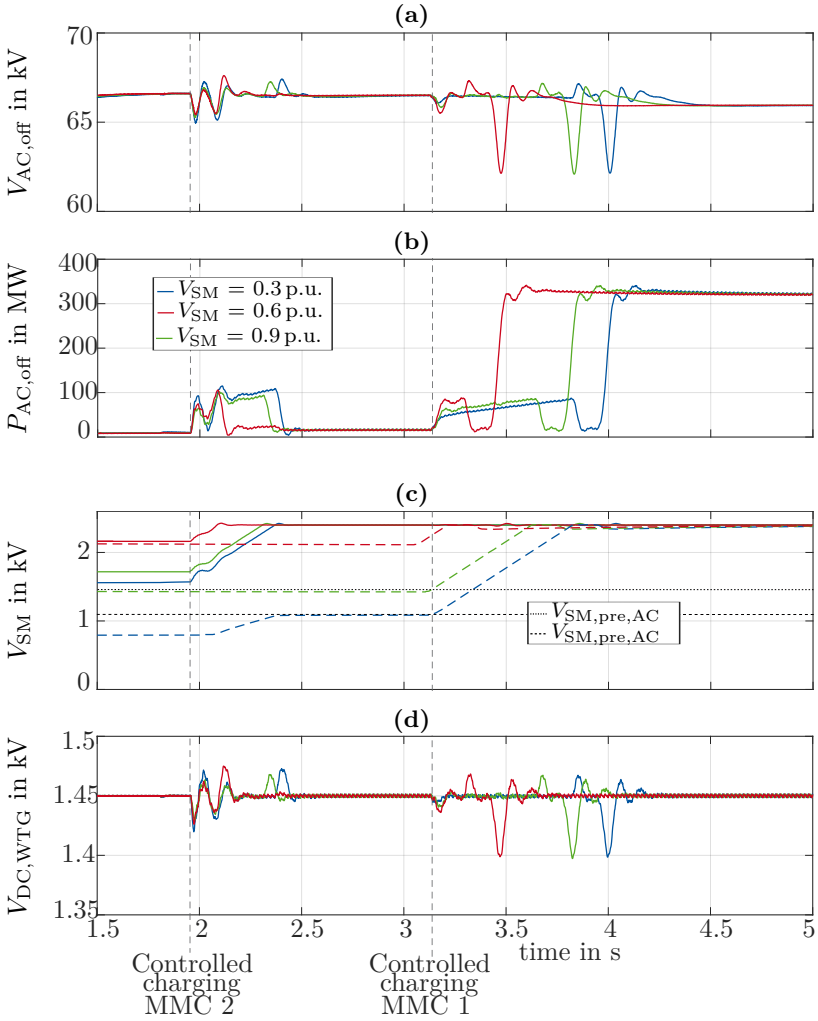


Figure 5.6: Controlled MMC energization and System energization: a) OWPP AC rms voltage, b) AC side active power, c) Submodule voltages (dashed: onshore, solid: offshore), d) WTG DC-link voltage [KHL25]

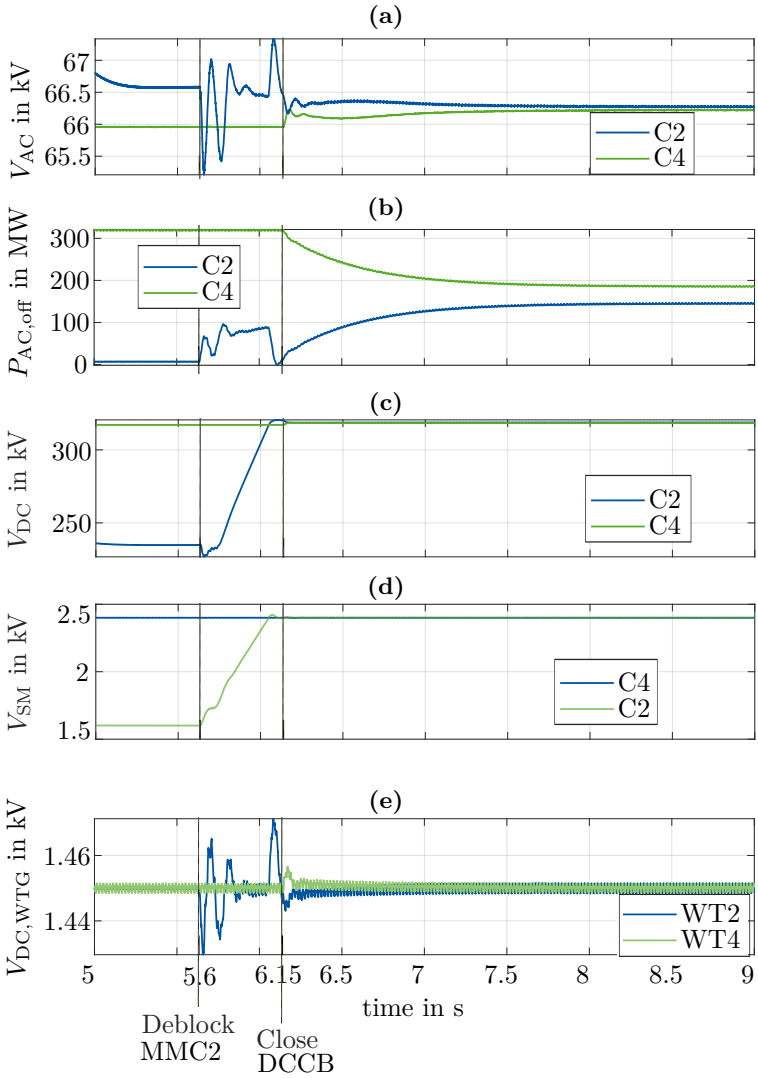


Figure 5.7: Reconnection of MMC2 and MMC4 via the DCCB (a OWPP AC rms voltage, b) AC side active power, c) DC side voltage, d) Submodule voltages (dashed: offshore, solid: onshore), e) WTG DC-link voltage [KHL25]

5.3 Conclusion

GFM WTGs present a suitable alternative for efficient reenergization of the system after a DC-side fault rather than energizing from the onshore side. During the restoration, the remaining submodule voltage after protective blocking of the converter and subsequent fault clearing, plays a crucial role in the requirements for the restart process. While for any remaining voltage, the system can return to normal operation and establish the pre-fault load flow below 5 s. A reduction of 43 % in active power is possible if submodules retain a voltage of 0.9 p.u. instead of 0.3 p.u. Therefore, a faster protective converter blocking can be beneficial for such systems to limit discharging of the submodules. In combination with alternative fault clearing strategies for the healthy zone, such as temporary blocking, protection requirements (e.g., lower reactor sizes, slower DC-side breakers or reduced power-electronic capabilities of the converters) could be greatly reduced. If more than 350 MW (highest active power peak during energization) of wind is available (for the investigated OWPP 35 %), the restart can be initiated without any additional equipment such as PIR or alternative startup methods. To reduce the transient active power peak requirement during the initial energization of the offshore MMC the soft energization was presented. It requires that the WTG are capable of reducing the voltage to a minimum in islanded operation and return to system voltage quickly to limit the outage time. For a fault on the interconnecting line, the faulty part can be seamlessly reconnected via the DCCB between the two separated HVDC system parts, splitting the active power provision for the onshore system between the two OWPPs after reconnection. The method is applicable for all offshore HVDC system designs, since after a DC-side fault, the system can always be broken down to a point-to-point system, requiring the GFM WTGs to energizes only its connected system part before either being reconnected to the onshore system or neighboring HVDC systems.

6 Temporary converter blocking during DC-side fault clearing

This chapter investigates the requirements and system effects of temporarily blocking the offshore converter after a DC-side fault to reduce the required HVDC breaker speed or its series DC reactor sizing. The focus lies on the healthy zone of a partially protected MTDC system. During fault clearing, instead of remaining in continuous operation, the offshore converter blocks, requiring the WTGs to maintain a stable offshore system. Three aspects are of main interested. First, what is the theoretical reduction in the inductance of the series DC reactor between continuous operation and temporary blocking. Second, what role does the temporary blocking duration play on the system behavior. And third, which fault-ride-through (FRT) requirements (offshore AC voltage, DC voltage, onshore active power) are the main constraint for temporary blocking.

Section 6.1 describes the fault clearing methodology applied in the investigations, providing an overview of the different control scenarios. Furthermore, the temporary blocking sequence is described and the evaluation criteria are presented. In Section 6.2, the required inductor sizes for continuous operation are evaluated and a required change to the control of the MMC shown in Section 3.2.1 is presented. The investigatory results to validate the methodology and compare the different control scenarios within EMT are shown in Section 6.3. Afterwards, the results and their impact on current FRT requirements are discussed.

This chapter is based on the publication: Enabling Temporary Blocking of Offshore Converters Through Grid-Forming Wind Turbines to Assist HVDC Grid Protection published in IET Generation, Transmission and Distribution [KTH25]

6.1 Fault clearing methodology

6.1.1 Dimensioning of the DC reactor

As previously described, the DCR needs to be dimensioned accordingly, to avoid protective blocking of the converters. In order to determine the required inductance of the DCR, the prospective blocking time Δt_{BLK} for a set of inductance values has to be determined. The prospective blocking time, is defined as the time from arrival of the traveling wave at the converter terminal until the overcurrent threshold is reached. To provide a worst case assumption, a fault is applied as a pole to pole ground fault, with a $0.1\,\Omega$ resistance, leading to the highest current rise inside the converter [BF13]. This fault is then applied to all cables within the faulty zone at 0 %, 50 % and 100 %, to account for traveling wave behavior [BPS18]. Furthermore, for each fault, multiple point of wave times are chosen, since the AC phase angle can lead to different blocking times [DDM23]. The according DCR size is the chosen, for which the prospective blocking time is larger than the total opening time of the breaker $t_{\mathrm{open}} = t_{\mathrm{DCCB}} + t_{\mathrm{det}}$ consisting of the DCCB opening plus a communication time delay for the fault detection.

6.1.2 Control scenarios

For MTDC systems and a connected offshore wind farm, different control scenario configurations can be possible in the future. Generally, for MTDC systems to avoid dependency on a single converter i.e., DC voltage control, droop controls are implemented on top of the main control modes, which are indicated for each control scenario. Furthermore, for these systems and protections studies, the full-wind infeed, offshore to onshore, is the most relevant and challenging scenario, due to the likely short term power outage and subsequent recovery requirement.

DC-FRT Scenario 1 (DC-FRT 1)

DC-FRT1 serves as a reference case for four different control combinations without temporary blocking. It will be used to, on the one hand, to investigate how the different control combinations impact the

converter protective blocking time t_{protBLK} and, on the other hand, to give an estimate on the system behavior for a state of the art protection design. For each combination the inductance value required to avoid protective converter blocking is determined in accordance with Section 6.1.1. DC-FRT 1.1 serves as the case with a state of the art control architecture (Figure 6.1a, Table 6.1 DC-FRT 1.1-4). GFL WTGs are used, and the offshore converter operates in U/f control to provide voltage and frequency for the offshore system in DC-FRT1.1. It will be compared to DC-FRT 1.2 and 1.3, with the adapted control architecture using GFM WTGs.

DC-FRT Scenario 2 (DC-FRT 2)

For DC-FRT2 the WTGs are controlled as GFM, while the onshore converter continues to provide the DC voltage (Figure 6.1b, Table 6.1 DC-FRT2). The aim of this scenario is to have a base case for the temporary blocking investigation, while replacing the GFL WTGs with GFM WTGs compared to DC-FRT 1.1. Additionally, the offshore converter control changes from GFM to GFL accordingly.

DC-FRT Scenario 3 (DC-FRT 3)

For DC-FRT 3, the control of the MMCs is flipped, with the offshore converter being in V_{DC} control (cf. Figure 6.1b, Table 6.1 DC-FRT3). This scenario serves as main investigation to determine the impact on the DC voltage, when the temporary blocked converter is the DC voltage governor and the onshore converter has to maintain the DC voltage via a $\mathrm{P}/V_{\mathrm{DC}}$ droop and simultaneously reduce the active power output. A too slow adjustment could lead to decharging of the submodules, while a to strong droop could lead to a reversal of the load flow.

DC-FRT Scenario 4 (DC-FRT 4)

For the DC-FRT4 scenario, the onshore converter will provide grid-forming for the onshore grid (cf. Figure 6.1b, Table 6.1 DC-FRT4). As a result, during the temporary blocking, there is no dedicated V_{DC} controller, and the DC voltage will only be maintained via the energy balancing of the onshore converter. Especially, during maximum load

power flows, this could lead to rapid discharge of the submodules, while trying to maintain grid forming capabilities.

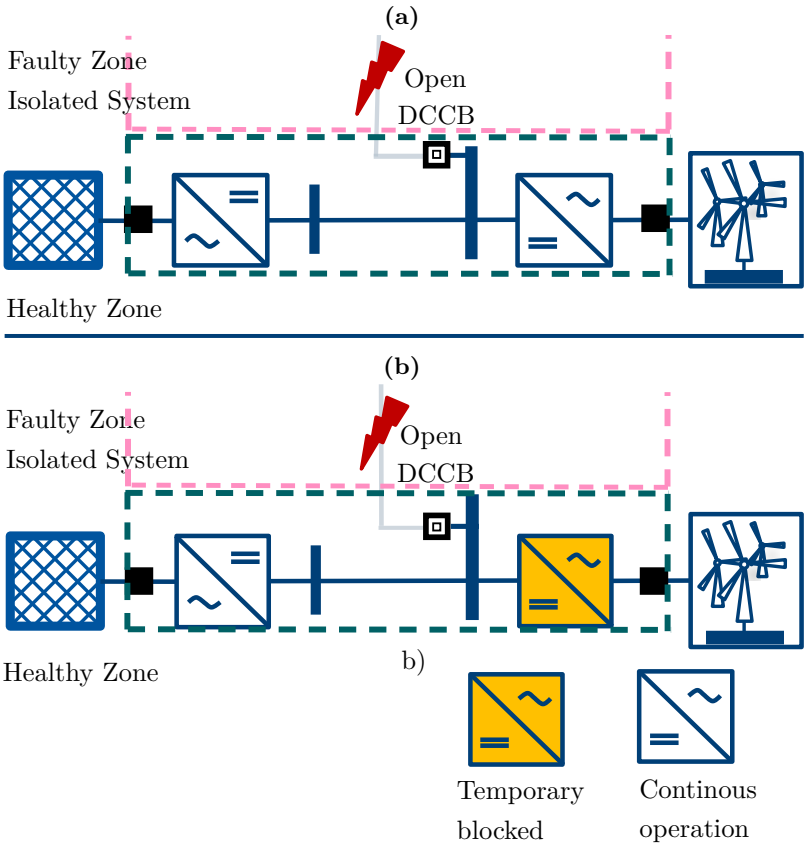


Figure 6.1: System under investigation, (a) Comparison without blocking (b) Temporary blocked converter during fault occurrence [KTH25]

Table 6.1: Control combinations of the FRT scenarios

FRT-Scenario	Onshore MMC control	Offshore MMC control	WTG control	Temporary block
DC-FRT 1.1	V_{DC}	U/f	GFL	0
DC-FRT 1.2	V_{DC}	P	GFM	0
DC-FRT 1.3	P	V_{DC}	GFM	0
DC-FRT 1.4	GFM	V_{DC}	GFM	0
DC-FRT 2	V_{DC}	P	GFM	1
DC-FRT 3	P	V_{DC}	GFM	1
DC-FRT 4	GFM	V_{DC}	GFM	1

6.1.3 Temporary blocking sequence

The temporary blocking is part of the general protection sequence for each converter. The sequence follows two branches: The internal protection branch (Figure 6.2, left) and the DCCB operation branch (Figure 6.2, right). After fault occurrence, an idealized fault detection is used to open the DCCB since the fault location is known within EMT, ensuring accurate opening of the DCCB providing repeatable results. Furthermore, since the DCR sizing is part of the analysis, each DCR would require a new evaluation of the protection algorithm parameters. Therefore, a location specific fault trigger, with a generic detection time delay of t_{det} is used. Depending on the system design detection is possible within a time frame of several hundred microseconds up to a few milliseconds [FRR25]. The detection is triggered by a DC undervoltage criterion $V_{\mathrm{DC,min}}$, usually based on the lower voltage criterion of the dynamic voltage band [Cig16]. In DC systems, it is generally used as main detection requirement, indicating the arrival of the traveling wave due to the fault. Location defining relays, such as directional current relays, can be omitted due to the simplified fault detection. The DCCB has an opening time of t_{DCCB}, which for today's design can range from 2 ms VSC Assisted Resonant Current DCCBs to 3 ms for hybrid DCCBss to 10 ms for mechanical DCCBss [Nor25, TRJ23]. Ultimately, the total time for DCCB operation is $t_{\mathrm{DCCB,open}} = t_{\mathrm{DCCB}}$

$+ t_{\mathrm{det}}$.

Simultaneously, prior to the DCCB operation, the DC voltage drop in the healthy zone caused by the fault results in a discharge of the converter SM capacitors, leading to an increase in the internal current. If this increase is not interrupted by the DCCB in time, the converter will block to protect the submodules. The defined overcurrent threshold is generally based on the maximum DC current rating with an overcurrent factor. The factor is used since the arm current also has an AC component, leading to a larger arm current than the rated DC current. An overcurrent factor based on available IGBT datasheets, generally between 1.35 and 2 times the DC current is used [DDM23, ABB25]. The converter blocks once the overcurrent threshold is reached and the converter remains blocked for a defined temporary blocking time t_{tempBLK}. The recovery sequence is initiated via a DC voltage recovery criterion also based on the DC undervoltage criterion of available DC-FRT curves, indicating that the DC fault is interrupted and the converter is part of the healthy protection zone [Cig16, STV24]. Since the system state changes, the integral parts of the PI-controllers of the blocked converter are reset once the deblock command is initiated, so that values do not end up in its limits making it impossible to return to a stable system operation. The PLL tracking of the offshore converter remains active to ensure the converter staying in phase with the offshore AC voltage and avoid transients upon reconnection.

6.1.4 Evaluation criteria

The performance evaluation and compliance to system requirements when utilizing temporary blocking as support in DC protection can be split into three groups. DC constraints, onshore AC system constrains, and offshore AC system constraints.

DC fault-ride-through (DC-FRT) criteria

For the DC side, the DC voltage is a main connection criterion, with a sustained DC undervoltage leading to a shutdown of the system. Although no DC-grid code exists, DC-FRT curves were developed in [Cig16] and reevaluated in [STV24] (Figure 6.3a). The curve is especially

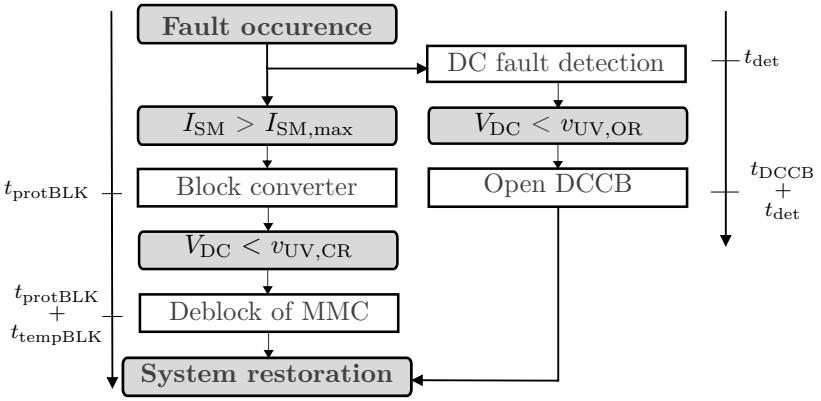


Figure 6.2: Flow chart of the temporary blocking sequence

important for the operational connection requirements of the onshore converter, which would be allowed to block if after fault clearing $t_{\mathrm{rec1,DC}}$, the voltage remains below DC undervoltage threshold $v_{\mathrm{UV,OR}}$. While in [STV24] no explicit times or values are given, in [Cig16] indications are presented as recommendation. The following values with exemplary values are proposed as key performance indicators (KPIs)) for the DC voltage recovery:

- $t_{\mathrm{rec1,DC}}$: DC voltage recovery after to fault separation; twice the opening time of the DCCB t_{DCCB} [STV24]
- $t_{\mathrm{rec2,DC}}$: DC voltage recovery to dynamic voltage band of ±15% ($v_{\mathrm{UV,OR}}$) in 200 ms [STV24, Cig16]
- $t_{\mathrm{st,DC}}$: DC voltage recovery to stationary voltage band of ±5% in 300 ms [STV24, Cig16]
- V_{SM}: SM charge of the onshore and offshore converter.

Onshore AC-FRT criteria

An HVDC system connected to a strong AC grid, modeled as a voltage source, is expected to have a low impact on the onshore AC voltage stability, and therefore AC voltage stability is not considered as a KPI. However, the loss of AC power can lead to frequency deviations in the

AC grid and subsequent shutdown. Therefore, the time of active power interruption will be compared for a the cases with and without blocking. The following KPIs are used for the onshore AC evaluation.

- $t_{\mathrm{P,AC,rec}}$: Active power recovery within a ±10% tolerance band [CEN18]

Offshore AC-FRT criteria

Lastly, for the offshore AC system the AC voltage stability determines the performance of the GFM WTGs and its islanding capabilities, as well as the subsequent reconnection capabilities with the offshore MMC. For the evaluation, the voltage FRT profile defined by the German "Netzanschlussrichtlinien" will be used (Figure 6.3b b)). Additionally, the DC-link voltage of the WTGs will be evaluated to determine the impact of the power loss on the WTG behavior. Therefore, the following KPIs are derived.

- $t_{\mathrm{rec1,AC}}$: AC voltage recovery start due to fault separation after 150 ms [VDE19]
- $t_{\mathrm{rec2,AC}}$: AC voltage recovery to 15 % of pre-fault voltage in 1.5 s [VDE19]
- $t_{\mathrm{st,DC}}$: AC voltage recovery to stationary voltage band in 2 s [VDE19]

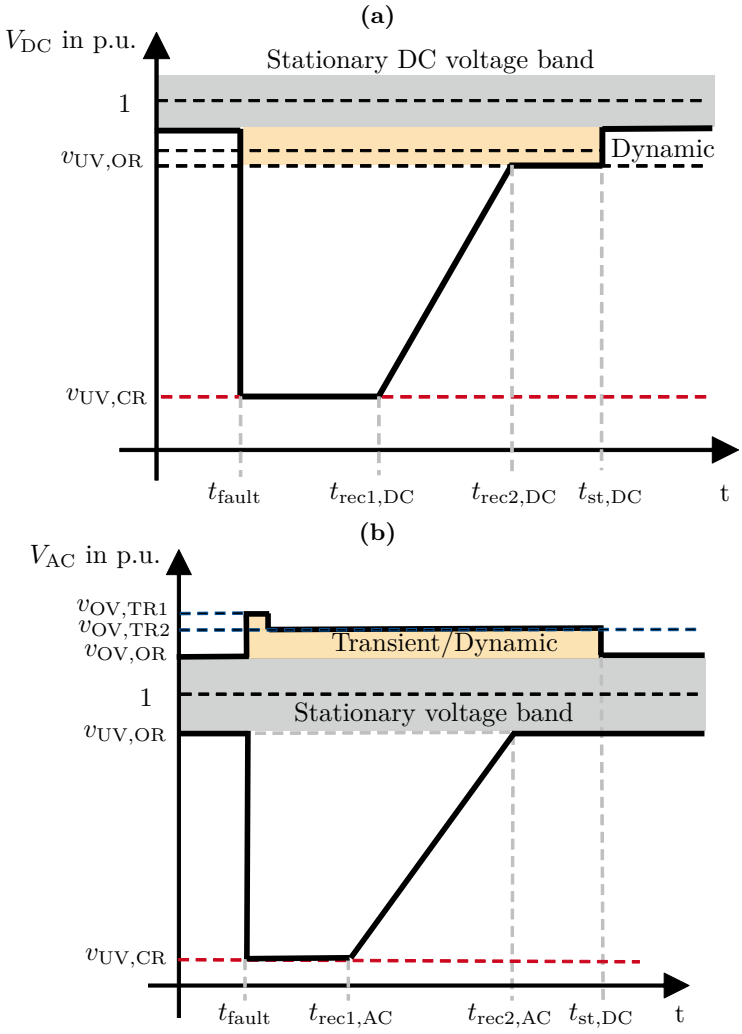


Figure 6.3: DC-FRT profile [STV24, Cig16], AC fault-ride-through (AC-FRT) profile [VDE19] [KTH25]

6.2 Protection implementation

Within this investigation, the primary blocking requirement is set to 2.7 kA overcurrent threshold, which translates to 1.35 times the DC current rating. As discussed in [KDL25], the blocking time is calculated as the $\Delta t_{\mathrm{protBLK}}$ of the traveling wave arrival at the converter terminal until the internal current reaches the blocking threshold. As a DCCB, a hybrid breaker with an opening time of 3 ms is used, and 1 ms protection communication delay is assumed. Therefore, the protective blocking delay needs to be larger than 4 ms for a given inductance. For longer opening times the inductance would have to be even larger, further strengthening the need for temporary blocking. Table 6.2, shows the blocking times of MMC 4, which is the critical converter, for inductance values from 25 mH - 400 mH. The lowest requirement on the inductance is for DC-FRT 1.1 requiring a minimum of 150 mH to protect the healthy zone. Due to the GFM WTGs, the protective blocking time decreases, since they aim to keep the offshore voltage higher resulting in a higher current. When the offshore converter is in V_{DC}, the implemented DC voltage feedforward, leads to a lower internal current rise than for the converter in P-mode (cf. Figure 6.4) [DDM23]. Therefore, the highest resulting DCR is for DC-FRT 1.2 requiring a DCR of 300 mH to avoid blocking within the DCCB opening time. (Table 3.2). For the other two scenarios DC-FRT 1.3 and DC-FRT 1.4 200 mH is sufficient. For the cases with temporary blocking an inductance as low as 25 mH is sufficient. Therefore, temporary blocking could enable an inductance reduction of 6 - 12 times depending on the control scenario.

6.2.1 Adaption to MMC control

During a DC fault, the GFM controlled converter aims to continuously provide AC power, due to keeping the angle reference. As a result, after fault occurrence and the subsequent DC voltage drop, the converter aims to provide the power through the submodule energy. Therefore, it is required to reduce the power output as fast as possible once the fault or a DC undervoltage is detected. In DC-FRT 3 and DC-FRT 4, a $\mathrm{P}/V_{\mathrm{DC}}$ droop is used to reduce the power and enable a return of the DC voltage. For DC-FRT3 this is done via the active power controller, and for DC-FRT 4 by adapting the angle calculated by the GFM control

Table 6.2: Protective blocking times of MMC 4 for DC-FRT 1.1,1.2,1.3,1.4

	Blocking time in ms			
Inductance in mH	1.1	1.2	1.3	1.4
25	1.34	1.32	1.48	1.33
50	1.82	1.98	2.18	1.86
100	3.9	2.66	3.32	2.98
150	**4.6**	3.54	3.87	3.75
200	7.7	3.64	**4.16**	**4.32**
300	11.22	**5.14**	5.42	5.31
400	14.34	5.5	6.76	5.74

(Figure 6.4). The rest of the control remains identical to the control described in Section 3.2.1.

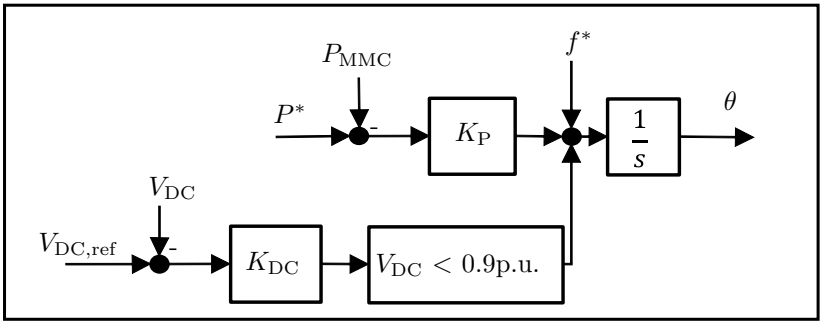


Figure 6.4: Implemented V_{AC}/f droop to adjust P [KTH25]

6.3 EMT-Studies of the different FRT-Scenarios

The temporary blocking of the offshore converter has a major impact on the AC power, DC voltage stability and offshore stability. Therefore, these three aspects are discussed and evaluated with the defined criteria.

6.3.1 System behavior of DC-FRT 1

Depending on the control structure of the different DC-FRT, the time of AC power is fully recovered after 200 ms for DC-FRT 1.1 and 1.2 and after 150 ms for DC-FRT 1.3 and 1.4. As discussed in Section 6.2 the highest required DCR is 300 mH for DC-FRT 1.2, which is used for all scenarios to compare the results of all control combinations. For DC-FRT 1.1 and 1.2, where the onshore converter remains the DC-voltage governor and the main control difference is the change from GFL to GFM WTGs, the AC power behavior is almost identical. After the initial drop to around 600 MW for around 50 ms, the power recovers but overshoots due to the response of the energy balancing control and the subsequent submodule charging. This overshoot settles after another 150 ms. The DC voltage behavior is identical (Figure 6.5 red and blue curves). Contrary, DC-FRT 1.3 and 1.4 behave differently. Due to the onshore converter operating in P or GFM mode, it aims to keep the output power constant independent from the DC disturbance. This results in a significantly larger voltage dip and slower DC voltage recovery, due to the submodules discharging deeper, than in the other two cases, since the onshore converter tries to continuously provide power (Figure 6.5 red and violet curves). This will also have a large impact on the blocking behavior, since the DC voltage return after deblocking will be more challenging.

6.3.2 Analysis of DC-FRT 2

For DC-FRT 2, the active power transfer is interrupted during the time of blocking (Figure 6.6a). It is the main restriction for the temporary blocking strategy, since no other limits are exceeded. For the 3 investigated blocking times 10 ms, 100 ms and 500 ms, the initial DC-voltage drop is higher than the case with no blocking. However, the recovery time is equal to the previous case irrespective of the temporary blocking duration. It is shown that the proposed DC-limit curve is not exceeded. Due to the power decrease, an overvoltage in the offshore system occurs, which remains below the 1.118 p.u. requirement of the AC fault-ride-through (AC-FRT) curve(Figure 6.6c red). After power recovery, a small voltage dip occurs, which does not violate the FRT curve either. The impact on the WTG DC-link voltage is similar

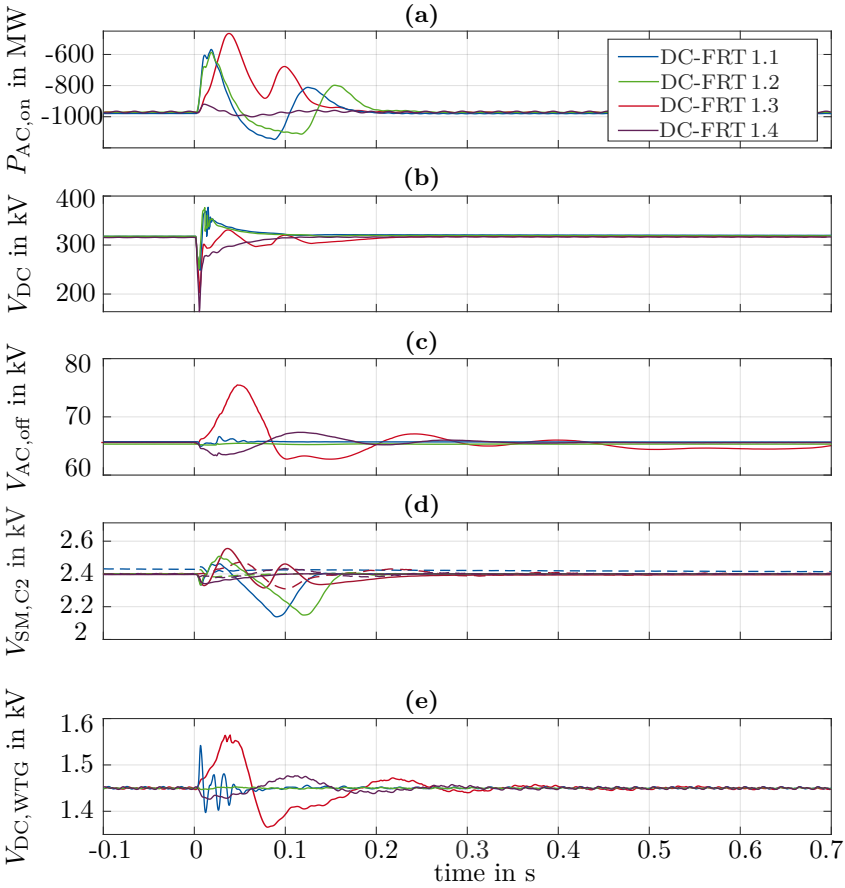


Figure 6.5: Comparison of the different scenarios without blocking: a) Onshore AC power, b) DC voltage, c) Offshore AC voltage d) Avg. submodule voltage C3 (solid) C4 (dash), e) WTG DC link-voltage [KTH25]

for all 3 temporary blocking times. The machine side of the WTG requires around 50 ms to adjust to the new power setpoint leading to an overvoltage in the DC-link. The chopper is activated during that

time (Figure 6.6d) to remove the excess energy until the machine side can reduce the power. However, this phenomenon would also occur during a complete shutdown of the system, which requires the WTGs to go from full power infeed to islanded operation with 0 MW power output in the same time frame. Therefore, it is not required to change the chopper rating of the WTGs to enable temporary blocking. The offshore AC voltage also settles as soon as the DC link stabilizes in its operating voltage. In conclusion, for DC-FRT2 all FRT requirements are met during the temporary blocking phase. If blocking is allowed solely depends if the AC system can withstand a power outage, which in the case of a 4-terminal system would be temporarily 2 GW for the blocking duration.

6.3.3 Analysis of DC-FRT 3

For DC-FRT 3, the temporary blocking shows the highest impact on the DC voltage behavior. Due to blocking the DC-voltage controller, the P-V_{DC} droop of C3 has to drastically reduce the power output to avoid a discharge in the submodules and in turn be capable of recovering the DC-voltage. For the temporary blocking times of 10 ms and 100 ms, the V_{DC} controller is deblocked prior to a full DC voltage return and the DC voltage quickly recovers. For the 500 ms blocking time, the droop is capable of returning the DC voltage within the DC-undervoltage limit (cf. Section 6.1.4). For the power recovery a ramp is used to avoid a deblock during full power and increase system stability (Figure 6.7). The DC-link of the WTGs as well as the Offshore AC voltage show a similar behavior to the previous case, with an overvoltage during the first milliseconds of blocking and a dip upon deblocking of the offshore converter.

6.3.4 Analysis of DC-FRT 4

In DC-FRT 4, the onshore converter continues to provide grid forming for the onshore system and aims to continuously provide active power. However, this results in a rapid discharge of the submodules of MMC 3 (Figure 6.8d). The DC voltage cannot recover until the offshore converter resumes operation and recharges the onshore submodules. As a result,

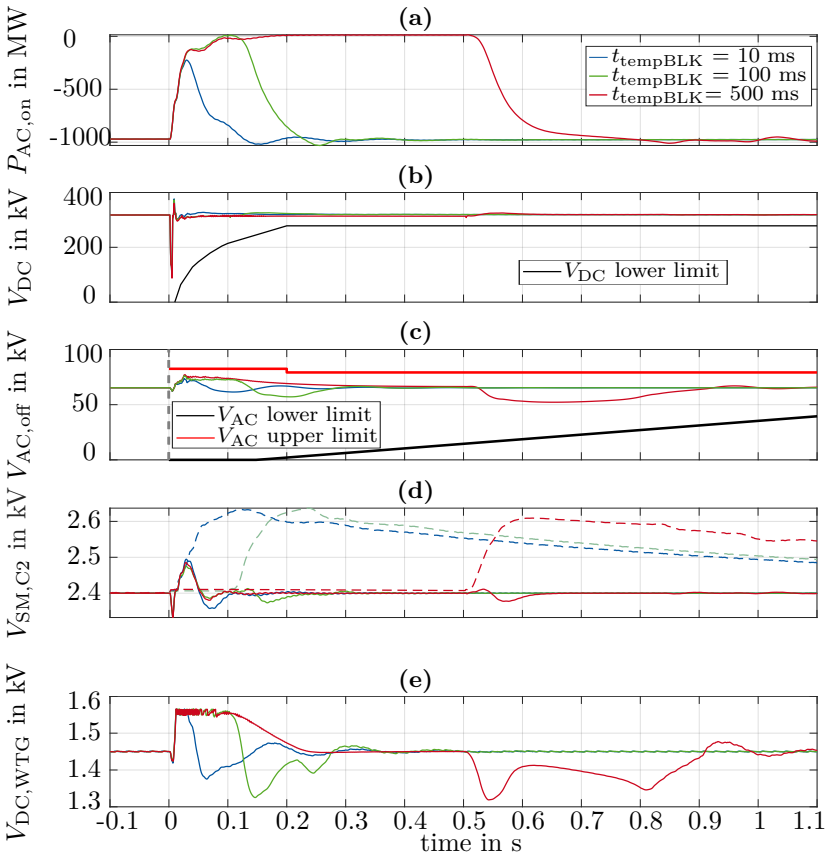


Figure 6.6: Comparison different temporary blocking times of DC-FRT 2: a) Onshore AC power, b) DC voltage, c) Offshore AC voltage d) Avg. submodule voltage C3 (solid) C4 (dash), e) WTG DC link-voltage [KTH25]

the DC voltage violates the DC-FRT requirement. The GFM WTGs keep the offshore voltage within the FRT limits for every blocking duration. The deblock and charging of MMC 3 leads to an additional power fluctuation, which results in a DC-link imbalance of the WTGs

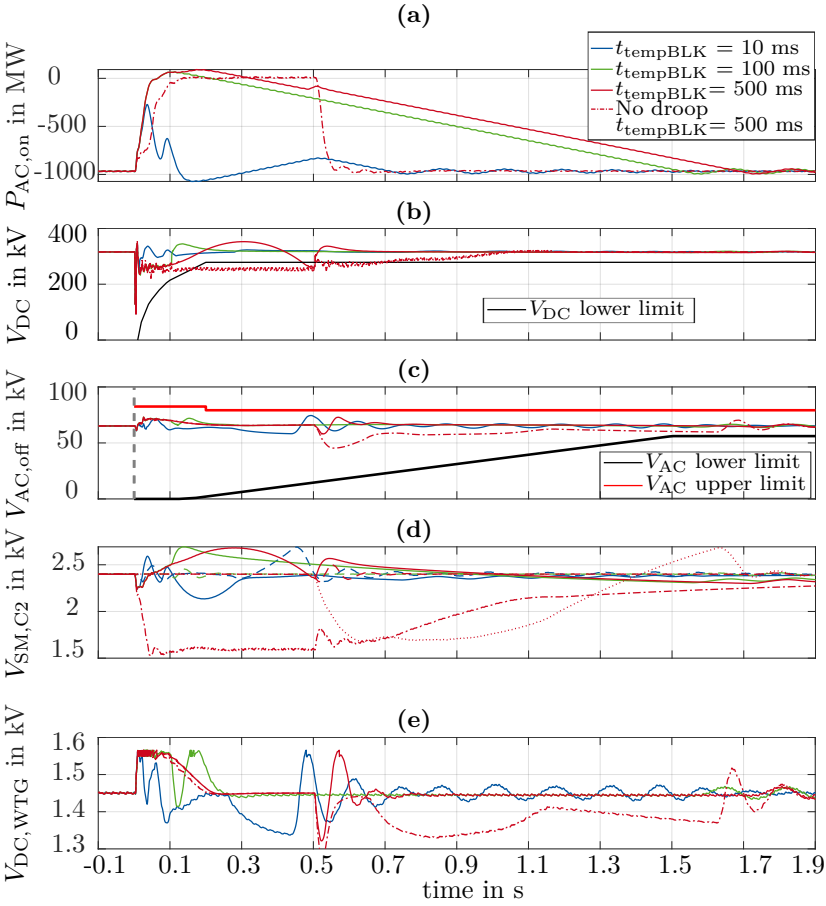


Figure 6.7: Comparison different temporary blocking times of DC-FRT 3: a) Onshore AC power, b) DC voltage, c) Offshore AC voltage d) Avg. submodule voltage C3 (solid) C4 (dash), e) WTG DC link-voltage [KTH25]

(Figure 6.8e). Due to these imbalances and the droop settings, the total power recovery time is also longer than in the previous scenarios

requiring more than 1.9 s to return to full power.For the machine side, the power adjustment leads to an increase of the rotor speed of around 0.04 p.u. and readjusts with the return of power to 1 p.u. (Figure 6.9a). The reactive power provision of the machine side reacts with the system behavior, resulting in a fluctuation during the deblocking and settling to the initial value with the return of power. A more aggressive P/f/V_{DC} droop setting could be chosen, however that can result in synchronization problems with the onshore grid and impede the GFM capabilities.The scenario, where the droop is deactivated shows, that the system can not return to normal operation at all since the submodules of MMC 3 are discharged even further and additional after the deblock of the offshore converter the submodules of MMC 4 discharge as well, since the WTGs cannot adjust to the continuous power demand onshore.

6.3.5 Discussion

Independent of the scenario, temporary blocking will always lead to an AC active-power outage larger than state-of-the-art fault clearing without temporary blocking. Depending on the system inertia, it is shown in [AWT17] that a certain loss of power for any time duration leads to a change in frequency potentially endangering the system stability. A combined investigation of a detailed AC system with temporary blocking is required to estimate maximum blocking times based on resulting frequency deviations. The AC power outage correlates with the temporary blocking duration of converter and resumes quickly (according to the defined power ramp rate) after the offshore converter returns to operation. Current grid codes specify the outage for HVDC connected offshore wind farms to a maximum of 150 ms [VDE19]. For the investigated cases of 10 ms and 100 ms, this requirement is full filled, with the outage for 100 ms being comparable of full-bridge converters [RCB19b]. The 500 ms investigated are currently not permissible. However, the value was chosen to provide general insights on the system stability and possible issues of a long blocking duration. Furthermore, it demonstrates the islanding capabilities of the GFM-controlled WTGs and return to connected operation independent on the time frame. For all control control scenarios the system is capable of clearing the fault and returning to stable system operation. The main difference within the scenarios lies in the impact for DC voltage, AC power and the

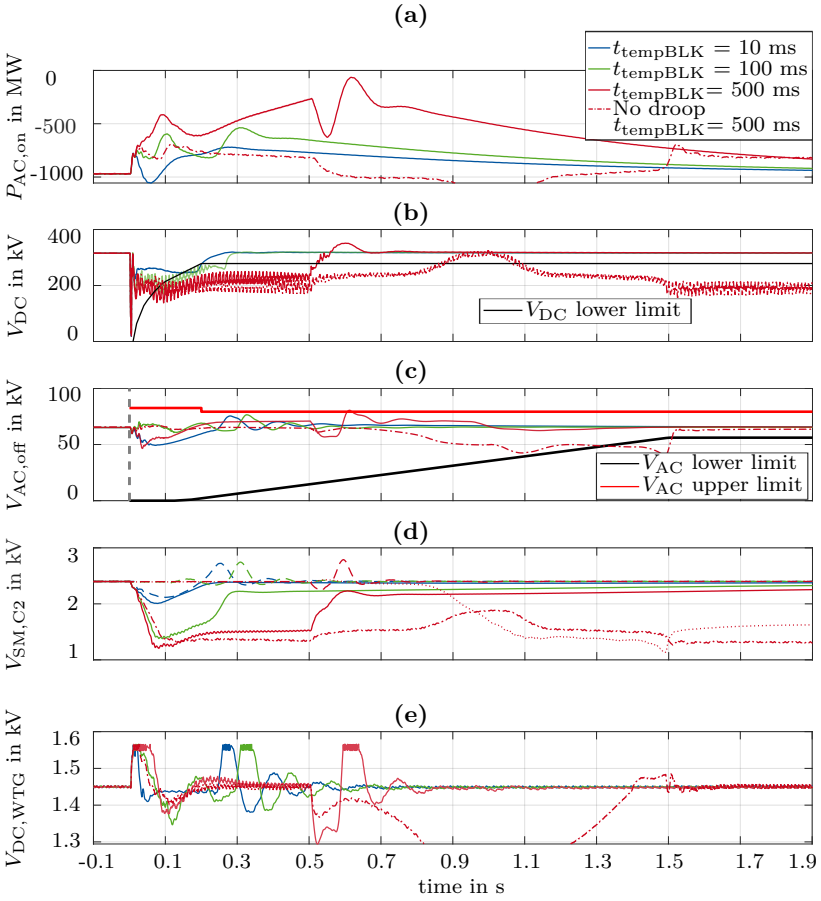


Figure 6.8: Comparison different temporary blocking times of DC-FRT 4: a) Onshore AC power, b) DC voltage, c) Offshore AC voltage d) Avg. submodule voltage C3 (solid) C4 (dash), e) WTG DC link-voltage [KTH25]

onshore converter submodule charge. While for DC-FRT 2, the power is reduced quickly due to the blocked converter controlling the power, for DC-FRT 3 and DC-FRT 4, the active power has to be reduced via

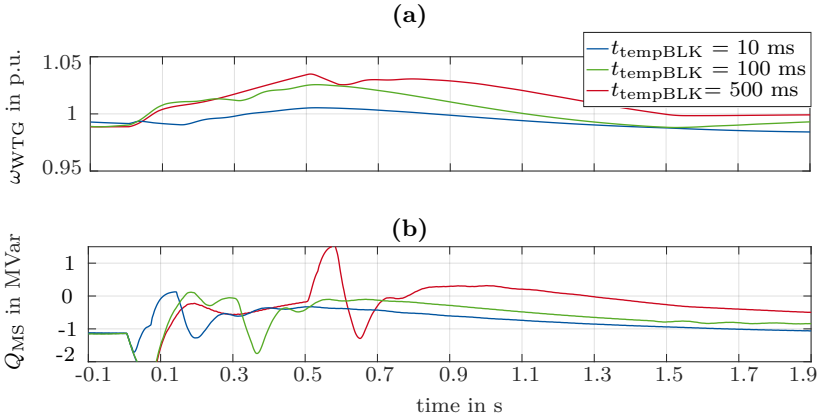


Figure 6.9: Comparison different temporary blocking times of DC-FRT 4: a) rotational speed of the wind turbine, b) reactive power of the wind turbine [KTH25]

a fast enough droop to preserve the state of charge of the submodules. This could then lead to a subsequent shutdown of the onshore converter requiring a full system restart. In [ZJ19b] similar results to DC-FRT 2 for a 10 ms blocking time were obtained for DC voltage and AC power response. However, the results within this publication show, that for the converters remaining in operation it is important to preserve their state of charge as well. Otherwise the submodule depletion leads to a subsequent DC undervoltage violating the DC undervoltage limit, leading to a full system shutdown. Therefore, fast power adaptions are required. The offshore voltage can be maintained stable within the specified AC-FRT limits for all scenarios, adapting to the overload situation due to the power loss. Furthermore, the initial protective blocking and power, has a similar impact on the WTG behavior, as a full loss of the HVDC system. However, the changes between power provision and zero power output, lead to fluctuations in both AC offshore voltage and WTG DC-link voltage, requiring an adaption of the power at the machine side. This leads to changes in the rotor speed of the machine. With the chosen WTG, design, the rotary speed changes are small but could still impact the longevity due to mechanical stresses. For the

WTG, this power adaption is the biggest challenge of the temporary blocking. Especially for very short temporary blocking times, it could be beneficial for the machine and system stability to keep the power output and dissipate the excess energy in the DC-link chopper. The limitation for power adjustment would be the capability of the WTG DC-link chopper.

6.4 Conclusion

GFM WTGs can enable temporary blocking of the offshore converter for a range of temporary blocking durations independent of the control scenario of the HVDC system. The WTGs enable a good transition between protective blocked and operational state due to continuously providing voltage and frequency while maintaining the voltage angle, to which the blocked MMC can reconnect. Furthermore, due to the inherent islanding capabilities, the FRT requirements shift from the GFL, which can maintain the offshore grid indefinitely, towards the HVDC system and onshore grid requirements. While temporary blocking can significantly reduce the requirements on DCCBs and DCRs, it requires evaluation of FRT requirements and MMC control combinations. The temporary blocked state requires a fast reduction of active power transfer, to preserve the submodule charge as much as possible. This is especially challenging, if the onshore converter is in GFM or active power mode, requiring large droop constants. In general, a temporary blocking always leads to a full AC power outage during the temporary blocking time and a subsequent recovery phase. For a short blocking time of 10 ms, the power loss is almost identical to a system with continuous operation, while having the capability reducing the inductance from 300 mH (CO) to 25 mH (TS). For temporary blocking duration >100 ms, the AC power loss for is identical to the duration plus the active power ramp up rate after deblocking, while the offshore FRT voltage limits and DC-FRT voltage requirements are met. Therefore, a closer investigation on the onshore FRT system requirements has to be conducted to determine the impact of a full power loss for the maximum temporary blocking time.

7 Post DC-side fault load flow control via GFM WTGs

This chapter provides insights on the post-fault operation of bipolar MTDC systems, if the poles are coupled on the offshore AC side, connecting both OWPPs to each of the poles. This allows for additional power transfer via the AC-side in a DC-side fault scenario, increasing post-fault power availability. To avoid overloading of the DC-side, the power transfer has to be sufficiently fast balancing the power over both poles.

Section 7.1 describes the three control scenarios to compare the load balancing via GFM WTG compared to the state-of-the-art. In Section 7.2, the post-fault load flow is analytically derived and then evaluated with EMT if the control are capable of adapting the load flow without overloading the HVDC system.

This chapter is part of the paper which was presented at the 23rd Wind & Solar Integration Workshop (WIW 2024) and is subject to Energynautics GmbH Copyright. The copy of record is available at the IET Digital Library https://doi.org/10.1049/icp.2024.3815.

7.1 Control strategy

For this investigation a bipolar system a 4-terminal MTDC system is investigated identical to the study performed in [KDM22] (cf. Section 3.2). The fault clearing strategy used within these investigations is a fully-selective fault clearing since it poses the highest requirements on power flow rebalancing requiring immediate adaption. By contrast, for partially selective or nonselective protection, the reenergization described in Chapter5 would precede the rebalancing requirement. Three different control combinations of onshore MMC control - offshore MMC control - WTG control are investigated to determine the performance of each combination (cf. Figure 7.1).

- Control Scenario A: V_{DC} - Droop Control (GFM) - GFL

- Control Scenario B: V_{DC} - P (GFL) - GFM
- Control Scenario C: Droop Control (GFM) - V_{DC} (GFL) - GFM

The controls for for the MMC are described in Section 3.2.1 and the WTG in Section 3.1.2 for the GFM and GFL controls respectively.

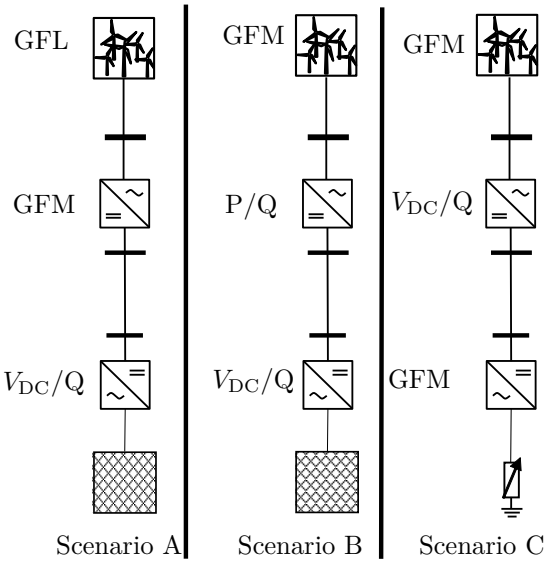


Figure 7.1: Overview of different system control scenarios (Single line diagram) (This figure has been reproduced with permission from Energynautics GmbH, 2024)

7.2 Post DC-side fault power flow

The main purpose of the AC coupling is to balance the power of the P- and N-Pole after a single phase fault as well as to increase redundancy. As discussed in [KDM22], for a decoupled AC-side the maximum post DC fault power for the OWPP of the faulty pole lies at 0.5 p.u. In the post fault state, the 0.5 p.u from the faulty pole can be fully transferred via the DC coupling to the healthy export link. However, this leads to an unbalanced load flow of 1 GW (which represents the limiting converter)

on one affected pole and 0.5 GW on the other. Shown as case 1 for C1 in Table 7.1 for a fault on the N-pole between C2 and C4. As seen in case 2 in Table 7.1 the N-pole of C3 and C4 have to be curtailed to 0.5 GW if the pre-fault power is 0.75 GW per pole. Alternatively the OWPP on C4 could be curtailed to 0.25 GW. To balance the power on the poles and to avoid the previous described curtailment, the system can be coupled on the AC side. The OWPP can be fully operated at 75 % in the post-fault state since the power balancing leads to an output power on the 3 remaining converters of 1 GW each by transferring 0.25 GW via the AC-coupling. This is represented with case 3 in Table 7.1 and in visualized in Figure 7.2. The case is shown, where the OWPP does not have to be curtailed by delivering 0.75 GW prior to fault occurrence. Any wind power output higher than the 75 % would result in the power flow shown in Figure 7.2 b). This is also represented with case 4 in Table 7.1. Technically, the coupling could be closed also after fault clearing. However, this would require to shut down the OWPP first and then restart to the new set points with the coupling closed. Closing the coupling after fault clearing with the OWPP in operation would lead to significant transients due to the phase shift resulting in the blocking of the converter connected to the faulty line. If the OWPP is shut down prior to closing, the requirements on the droop control and resulting active power transfer are relatively low. Therefore, the approach is chosen to close the coupling prior to the fault to achieve an immediate control reaction, with case 3 and 4 of Table 7.1.

In accordance with Table 7.1, the fault will be applied at 50 % on the negative pole of the line that connects the onshore converter C2 to the offshore converter C4. And is assumed to be continuous over the simulation time. In order for the system not to overload both converters need to adjust their power, in order to transfer 250 MW via the coupling at C3 and C4 (cf. Figure 7.2). Two solutions can be proposed when using a GFM controlled MMC. Either through communication initiating a active-power setpoint change for both offshore converters immediately leading to a reaction of the implemented droop control. An alternative option would be to implement an additional V_{DC}/f-offshore droop, which adjusts the offshore frequency, allowing for a DC feedback on the P/f droop [KDM22, DBT22]. To compare these results to the results presented in [KDM22], the communication between C3 and C4 is used, to achieve the set point change with an equal time delay

Table 7.1: Operational examples, Fault C2-N-C4-N (green onshore, blue offshore)

Case	P_{sum} Pre	P_{sum} Post	Pole	Post fault power in GW C1	C2	C3	C4	AC coup
1	2	2	P	-0.5	-0.5	0.5	0.5	Open
			N	-1	0	0.5	0.5	
2	3	2.5	P	-0.75	-0.75	0.75	0.75	Open
			N	-1	0	0.5	0.5	
3	**3**	**3**	**P**	**-1**	**-1**	**1**	**1**	**Closed**
			N	**-1**	**0**	**0.5**	**0.5**	
4	4	3	P	-1	-1	1	1	Closed
			N	-1	0	0.5	0.5	

of $t_{comm} = 10\,ms$. The change is triggered by the opening signal of the breaker changing the offshore converter setpoints from 750 MW per converter and pole to 500/1000 MW for the P and N pole of the offshore converters (cf. Figure 7.2), respectively. During this simulation the onshore converters are connected to a strong AC-grid.

For an investigation without communication, the control structure is adapted from Control Scenario B to Control Scenario C (cf. Figure 7.1). It represents a possible future case, where the onshore converter is required to provide GFM. This investigation stems from the idea, if a DC fault would occur after the HVDC system black started a block load with a bipolar MTDC system. As a result, the DC-voltage is controlled via the offshore converter and the AC grid is established by the OWPP as in the previous case. The investigation performed will determine if through the energy balancing and DC voltage droop the new load flow can be established.

7.2.1 Strong AC-grid

When the HVDC system is connected to a strong AC-grid on the onshore end, both Scenario A and Scenario B achieve a stable post DC

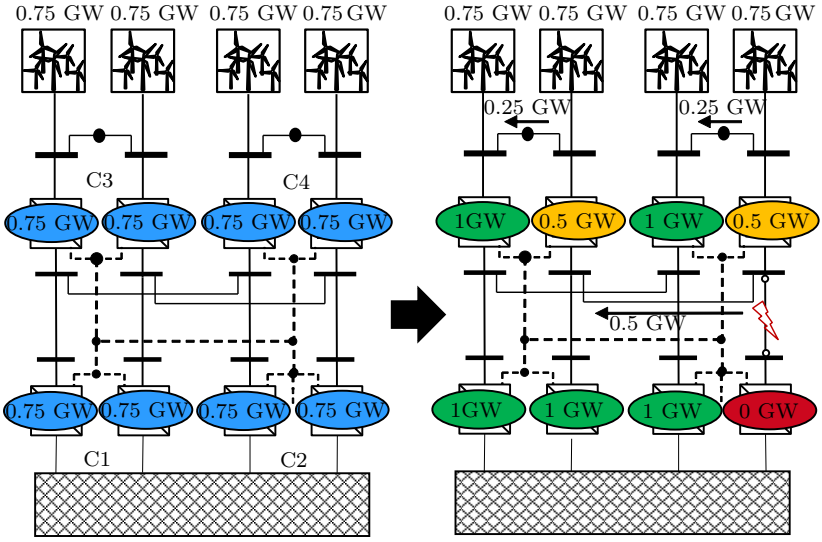


Figure 7.2: Visualization of load flow of Case 3 (cf. Table 7.1) (This figure has been reproduced with permission from Energynautics GmbH, 2024)

fault state with the new required power flow visualized in Figure 7.2. The simulated results are shown in Figure 7.3. Scenario C is shown as indication and will be discussed in the next section. In [KDM22] it was discussed that for different droop constants, the load flow adjustment is not fast enough and leads to blocking of the onshore converter due to overloading of the submodules. A stable post-fault was achieved with a droop constant of $k_\mathrm{p} = 0.08$, which is used as the case for comparison (cf. Figure 7.3 green). The difference in the initial values ($\mathrm{t} < 0\,\mathrm{s}$) results from the changes in control and its respective droop settings on the DC side leading to an 6 kV difference and lower pre-fault power. For clarity, the fault occurrence is set to 0 s for every plot. The initial voltage drop (Figure 7.3a) for C1 is identical for both cases. After around 0.5 s both cases reach the stable voltage band. For the AC active power it can be seen that for mode B the response time is around 0.2 s faster than for mode A reaching the new operational point at around 0.3 s. This is also shown in Figure 7.4. It might be possible to achieve the same speed

for the MMCs original case with a higher droop constant. However, as seen at t = 1 s in Figure 7.4, a k_p of 0.08 leads to a slight overshoot before achieving a new set point, which would be larger for higher droop constants, requiring a trade-off between speed and overshoot. The GFM WTG power balancing shows no overshoot, while achieving the new load flow on the offshore end after 0.2 s(cf. Figure 7.4). The slight difference in the AC active power output, indicate that the V_{DC}/P droop is not 100 % accurate since the output power of C1 is slightly higher than 2 GW (cf. Figure 7.3c t = 1 s) while the output power of C2 is lower than 1 GW (not shown). For the machine side as well as for the DC-link of the WTGs this load flow adjustment is negligible since the power output per string does not change but rather, the required 250 MW are transferred via the coupling as intended.

7.2.2 Block load without curtailment

The connected block load is set to 3 GW to ensure the same pre- and post-load flow as for control mode A and B. Mode C presents a special operational case, with a DC fault occurrence shortly after a black-start of a block load. Like the other modes, the system returns to stable operation and the intended load flow visualized in Figure 7.2. However, the immediate DC post-fault behavior differs from the previous discussed modes. Right after fault occurrence, the power of the affected pole (C4-N) drops to zero before recovering and establishing the new power flow after 0.5 s for the P-pole and after 0.7 s for the N-pole (cf. Figure 7.4 grey). This also has an effect on the DC-voltage, which shows higher fluctuations but no DC-chopper activation. Furthermore, the output power of C1 is reduced to 1200 MW before recovering to the intended output power (cf. Figure 7.3). The loss of power occurs due to an immediate control interaction between the GFM WTGs and the offshore converter, with the disconnection of the pole. Due to the loss of the P-pole the total energy balancing control of the MMC reduces its i_d current reference to 0 for the first ms after the fault. This leads to an i_d reference change in the GFM WTG resulting in a temporary zero current output seen in Figure 7.6c at t = 0.2 s in accordance with the power output seen in Figure 7.4. After around 100 ms the system stabilizes as the power on the P-pole recovers aiming to establish the new load flow. Due to the short term power loss on the affected pole,

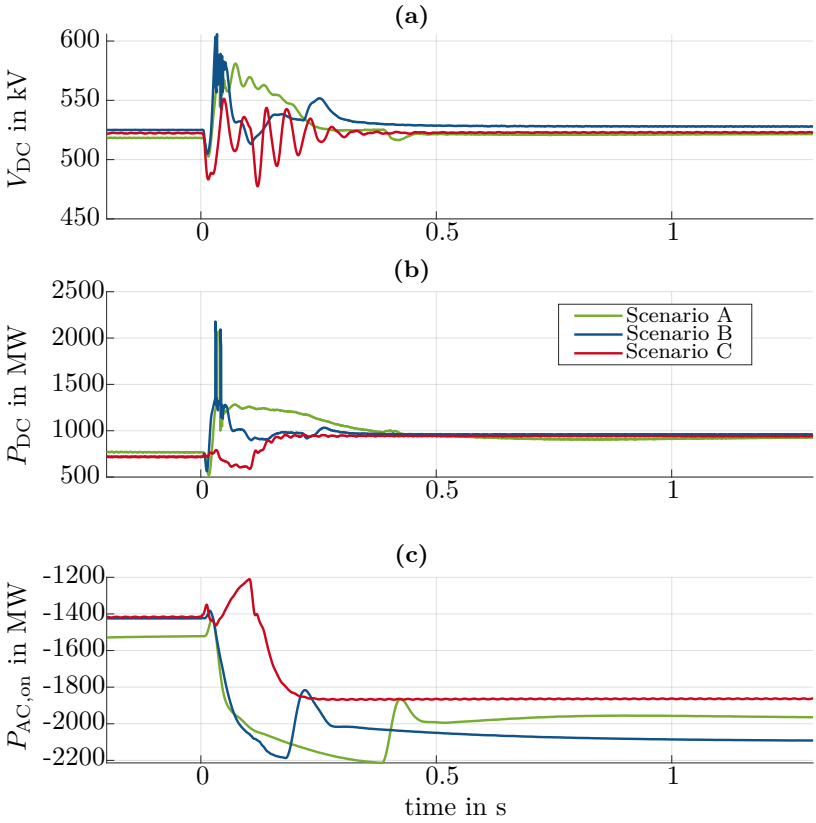


Figure 7.3: Comparison of the three scenarios for values at C1 (a) DC voltage, (b) DC active power, (c) AC active power (This figure has been reproduced with permission from Energynautics GmbH, 2024)

the WTGs DC-link is overloaded since the machine side cannot follow the power change. This leads to an activation of the DC-chopper with an total energy dissipated for all 280 WTGs of 3.92 MJ or 14 kJ per WTG (cf. Figure 7.6a, Figure 7.6b). For the onshore end, during the power drop the voltage sags for the same duration but the frequency can be maintained(cf. Figure 7.6e).

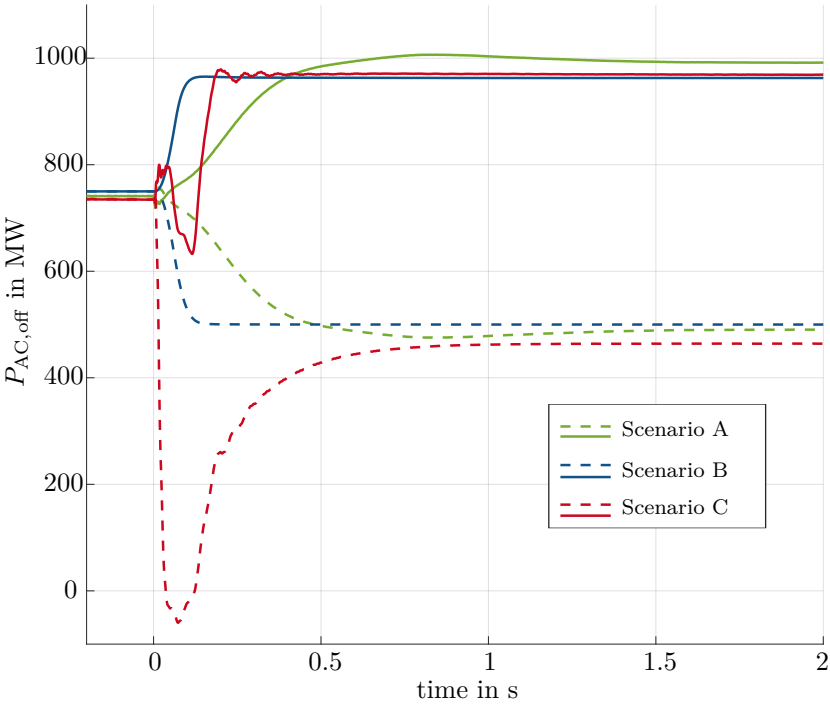


Figure 7.4: Comparison of the offshore AC active power for the three modes: solid Pole P, dashed Pole N (This figure has been reproduced with permission from Energynautics GmbH, 2024)

7.2.3 Block load with curtailment

The immediate fault response of the system with a full active power transfer of 4 GW is identical to the previous presented case. Due to the higher initial active power, the loss of power on the affected pole leads to a higher energy dissipation in the turbines (cf. Figure 7.5a. The total energy dissipated is 10.08 MJ or 36 kJ per WTG. The OWPP then returns to the values shown in case 4 in Table 7.1 essentially curtailing al WTGs to 750 MW and transferring the 250 MW over the coupling as intended. In Figure 7.5 is shown, that case 4 returns to the same operational point as case 3. Due to the initial voltage drop, the

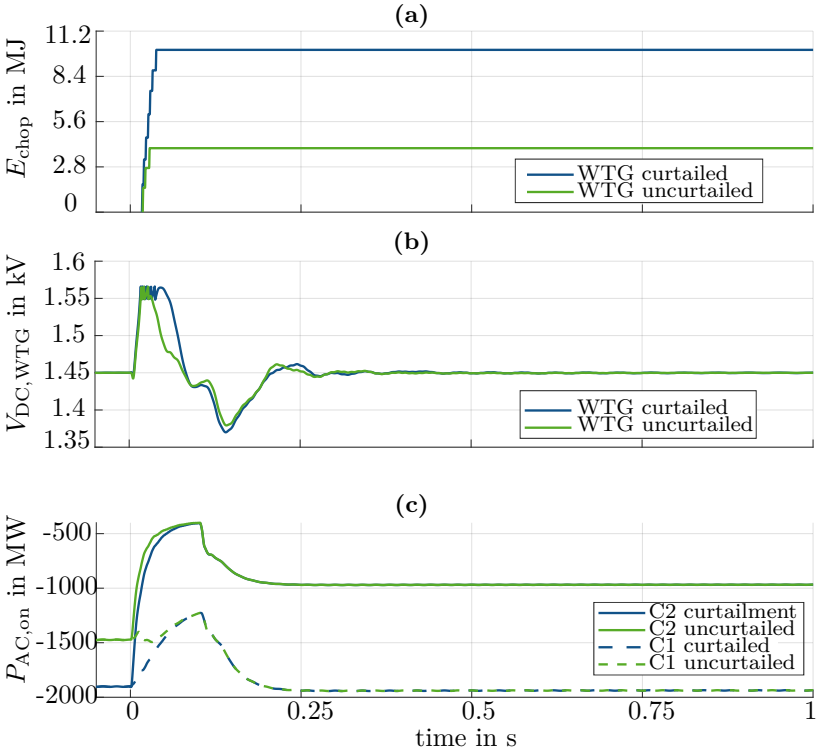


Figure 7.5: System values comparison case 3 and case 4 (a) Sum of Dissipated energy all WTGs of C4, (b) Exemplary DC-link voltageWTG at C4, (c) Active power C1 and C2 (This figure has been reproduced with permission from Energynautics GmbH, 2024)

curtailment does not lead to any additional overloading of the DC-link of the WTGs, but rather the return to the operating point leads to a sag in the DC voltage (cf. Figure 7.5b).

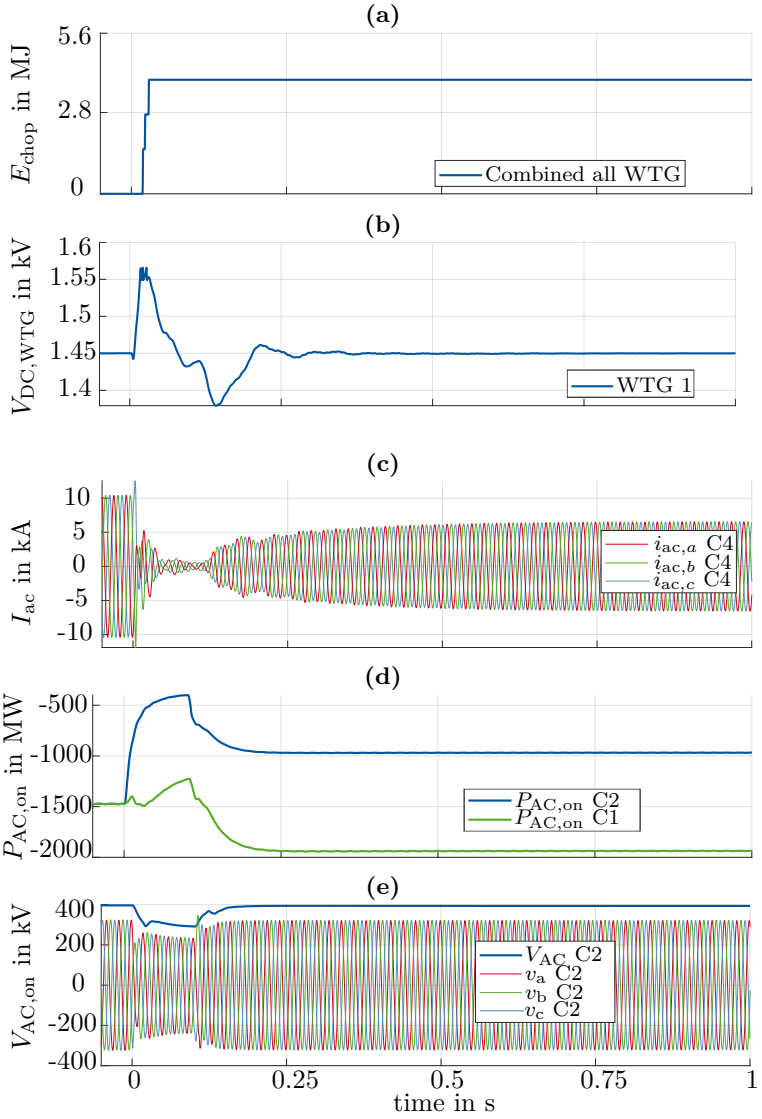


Figure 7.6: System values (a) Sum of Dissipated energy all WTGs of C4, (b) DC-link voltage of a single WTG at C4, (c) AC current at C4-N, (d) Active power C1 and C2, (e) Onshore voltage C2 (This figure has been reproduced with permission from Energynautics GmbH, 2024)

7.3 Conclusion

Similar to a droop control for an offshore MMC in a bipolar configuration, GFM WTGs are capable of providing a post-fault power redistribution via an AC coupling of the HVDC system poles. With the defined control settings, the GFM WTG adjust to the new power setpoint faster than the droop control of the offshore converter. Furthermore, in a post black-start scenario, with an island established by the onshore converters, the onshore voltage can be maintained during the DC-fault, while establishing the new load flow. However, right after fault occurrence the power of the affected pole drops to zero for a few milliseconds requiring DC-chopper activation in the WTGs. Nevertheless, the impact on the overall system stability is similar to the scenarios where the system is connected to a strong AC grid. This highlights the benefits of GFM WTGs and their capability to provide a stable post DC fault load flow for different operating conditions. Further investigations into connection to weak onshore grids can be performed with the same system architecture in the future.

8 Conclusion and Outlook

As the number of HVDC-connected OWPPs increases while the number of synchronous generators decreases, the question arises whether the former should take over the grid services performed by the latter. Furthermore, in case of OWPPs connected to multi-terminal HVDC systems, similar questions on system support arise when facing DC-side faults. Especially in light of GFM controlled WTGs, opportunities emerge during black start and DC-side faults. While existing research has covered the general capabilities of GFM control in WTG, the studies have been limited and simplified, focusing on single aspects mainly in black start scenarios. The overall design implications on energization requirements, adaptations to DC-side fault clearing, such as temporary blocking and required load-flow adaptations due to changed topologies are still missing. Furthermore, the possibility of GFM WTG to reduce protection requirements in HVDC systems due to its inherent islanding capabilities, without requiring a control switch, has not been studied.

This thesis addresses these gaps and contributes to a holistic understanding of the benefits and use of GFM WTG in future OWPP connected via HVDC systems. It provides a control solution for grid-forming controlled WTG in a black-start scenario and translates the design to DC-side fault handling, in multi-terminal HVDC systems. The benefit of using GFM WTG for DC-side fault protection strategies is evaluated in monopolar and bipolar configuration. In the following, the main contributions of this thesis are presented, combining the results obtained from the investigations. Finally, an outlook for future research is provided.

8.1 Contributions and conclusions

System energization by offshore wind power plants

This thesis has proven that active power requirements during black-start through OWPPs with grid-forming WTGs require at most 10 % of the total installed capacity, regardless of the energization method. The

energization methods, hard and soft energization, differ in requirements, where hard energization requires additional equipment in form of a PIR and soft energization relies on communication between offshore converter and OWPP to ensure that all systems are ready for restart and between the WTGs to ensure a simultaneous ramp up of the voltage. These conclusions were achieved through a detailed EMT simulation of the black-start procedure, with an in depth of the start-up procedure of the OWPP itself and the energization of the converters. The findings are important in assessing the availability of wind farms for black start, which, in a preliminary assessment of this thesis, amounts to 80 %. Furthermore, it presents an estimate on the importance of the layout of the OWPP itself and the MMC parameters, which have to be considered in the design phase of the system for black start readiness. For the OWPP to remain within the active and reactive power limits during black start, additional equipment might be required depending on the design to energize cables and transformers. For the MMC submodule and corresponding AC and DC-side voltage have a large impact on the active power drawn during first connection impacting the black start availability.

Post-fault energization by offshore wind power plants

This thesis has shown through simulations that a OWPP should be capable of maintaining a stable islanding within grid code requirements after a DC-side fault and subsequent converter blocking. Afterwards, it should be capable of efficiently re-energizing the offshore converter and the system at even lower active power requirements than during the black start. Both hard and soft energization, show stable restart processes with the latter taking around 4 s longer, due to the initial ramp down of the voltage, while the hard energization can restore the system immediately after fault clearing. These conclusions were achieved through detailed EMT simulations, going beyond the current state of the art in using a dedicated grid forming control for the WTG, and integrating different post-fault state in the energization process, which integrally changes the system behavior. These findings are important for future MTDC system designs, enabling a fast system restart and with it return of active power to the onshore grid, because the OWPP can remain in operation. Not only does it aid in fast power recovery but also improves overall system stability, since no additional power

from the already impacted onshore grid is needed to restore the offshore system. Therefore, the perception of HVDC connected OWPP as power sinks during energization would change drastically.

Temporary blocking of the offshore converter

GFM controlled WTG were found not only beneficial for recovering the faulty zone as described before but also aid in DC-fault clearing in the healthy zone. During a DC-side fault, the converter can temporary block significantly reducing either the opening time of the breaker or the inductance of the series inductor. Within the specified system design a reduction of the inductance from 300 mH (required for continuous operation) to 25 mH was achieved. Furthermore, it was shown that the control of the system has a large impact on the system behavior. While temporary blocking always leads to a temporary active power outage the system integrity can be maintained. These conclusions were achieved through a detailed EMT simulation, going beyond the current state of the art by identifying possible control issues, especially when the onshore converter is required to provide grid forming, and using a modeled OWPP rather than using voltage source approximations. Additionally, these findings provide design possibilities for DC-side fault clearing. With expanding MTDC systems large inductors threaten the DC-side stability of the system. Reducing these to their minimum required size for interrupting the fault current could simplify MTDC system designs in the future. Since protection design and converter design are closely intertwined, reducing the design constraints for both healthy and faulty zones by using GFM WTG facilitates the development of future DC-FRT specifications and multi-vendor designs. Based on the results, temporary blocking is mainly dependent on the AC grid codes, since the WTG are technically capable of maintaining the island indefinitely. Therefore, grid code adaptations allowing for an temporary active power outage < 1s can be beneficial for the overall system operation and design of offshore MTDC systems.

GFM WTG post-fault load-flow control in bipolar systems

Coupling the AC side of the offshore converter in bipolar MTDC systems can increase the operational flexibility and increase the post-fault power by 20 % for a four-terminal MTDC system. After DC-side fault clearing, the GFM can establish the new load flow faster than in current designs

with the converter being controlled in U/f and the WTG in grid following. Furthermore, in overload situations, the grid forming control adapts quickly, reducing the power and avoiding overload of the DC-side. While the machine side is required to follow these adaptations, the impact on the machine side in this case is lower than a required OWPP shut-down in current state-of-the-art-systems, with the DC-chopper working within its limits. These findings were achieved through a detailed EMT simulation, by investigating a bipolar MTDC system with a closed offshore pole coupling. The findings are important for future design choices of bipolar systems, maximizing the immediate post-fault power increasing onshore system stability due to maintaining the active power in-feed.

8.2 Future research needs

While the provided benefits of GFM WTG, for black start and DC-side fault operation are believed to be major contributions to increase the reliability and availability of future offshore systems, this work has only addressed parts of the overall challenge for the operation of future offshore HVDC systems.

Energization of bipolar MTDC-systems

Future systems are planned to be build as bipolar systems, similar to the design used in Chapter 7. With this, control and protection challenges increase and could change the requirements derived for a black-start scenarios due to the coupled operation of the poles. Since two converters are required to energize simultaneously to provide a stable DC voltage, accurate startup coordination of the two poles of the wind farms is required. Especially, since the grounding point is usually planned onshore balancing of the poles offshore could be challenging. Otherwise, it could lead to unnecessary active-power requirements, system instabilities and imbalances between the poles and DMR.

Onshore system impact of DC-side faults

This thesis focused on the interdependence between the offshore converter and the OWPP. However, also the onshore system is undergoing a transition towards a converter dominated system. It was shown that

the system control has a large impact on the system behavior and dynamic response, while using Thevenin equivalents for the grid as network representations of different strengths. With increasing system sizes of MTDC systems and potentially higher resulting outages it needs to be evaluated, how temporary blocking might impact the AC-system stability at the point of connection. Furthermore, the blocking of the offshore converter stays in contrast to the onshore converters capability to provide grid-forming capabilities further impacting the AC-system. A study of the proposed linear MTDC system connected to a detailed modeled AC-grid is required to fully understand, the impact on the AC-system. Furthermore, current AC-grid codes have to be closely investigated and require potential adaption to fully benefit from the use of GFM WTG.

Protection requirements and designs

The use of GFM WTG has different implications on the protection design depending on the investigated protection zone. A post DC-side fault restart from the OWPP benefits from fast blocking of the converter, while the healthy zone currently requires the converter to stay in operation currently posing high requirements either on the converter or protection design. However, combined with the proposed methodology of temporary blocking the overall system could benefit from lower protective thresholds, so that a higher submodule voltage can be preserved. While for the linear design presented the protection specifications can be easily derived, for larger MTDC or bipolar systems DC grid codes would be required to ensure safe operation, while reducing protection requirements and therefore the costs for future systems.

Mechanical impact on the WTG

The changes in active power and with it reduction or increase in the rotational speed of the machine, are expected to have an impact on the mechanical and structural design of the WTG. Therefore, detailed mechanical models of the machine, shaft and ocean wave propagation would be required in combination with the provided electrical results to derive the possibilities and additional limitations of implementing grid forming controls in offshore WTG.

Bibliography

[AAE20] A. Alassi, K. Ahmed, A. Egea-Alvarez, et al., eds.: *Performance Evaluation of Four Grid-Forming Control Techniques with Soft Black-Start Capabilities*. IEEE, 2020.

[AAE23] A. Alassi, K. H. Ahmed, A. Egea-Alvarez, et al.: "Transformer Inrush Current Mitigation Techniques for Grid-Forming Inverters Dominated Grids". In: *IEEE Transactions on Power Delivery* 38.3 (2023), pp. 1610–1620.

[ABB25] ABB Switzerland Ltd: *Data Sheet SMA 3000L450300 StakPak IGBT module*. Accessed: Feb. 02 2025. 2025. URL: https://new.abb.com/products/5SMA3000L450300/5sma3000l450300.

[AK22] A. Alefragkis, S. Kabul: *Next Generation Offshore Grid Connection Systems: TenneT's 2 GW Standard*. https://electra.cigre.org/321-april-2022/technology-e2e/next-generation-offshore-grid-connection-systems-tennets-2-gw-standard.html. Accessed: 2025-05-28. 2022.

[ALv20] M. Abedrabbo, W. Leterme, D. van Hertem: "Systematic Approach to HVDC Circuit Breaker Sizing". In: *IEEE Transactions on Power Delivery* 35.1 (2020), pp. 288–300.

[ASM19] M. Aten, R. Shanahan, F. Mosallat, et al.: "Dynamic Simulations of a Black Starting Offshore Wind Farm Using Grid Forming Converters". In: *18th Wind Integration Workshop*. 2019.

[AWT17] M. Abedrabbo, M. Wang, P. Tielens, et al., eds.: *Impact of DC grid contingencies on AC system stability*. Institution of Engineering and Technology, 2017.

[BB14] A. Beddard, M. Barnes: "HVDC cable modelling for VSC-HVDC applications". In: *IEEE PES General Meeting*. 2014.

[BF13] M. K. Bucher, C. M. Franck: "Contribution of Fault Current Sources in Multiterminal HVDC Cable Networks". In: *IEEE Transactions on Power Delivery* 28.3 (2013), pp. 1796–1803.

[BH07] H.-P. Beck, R. Hesse: “Virtual synchronous machine”. In: *9th International Conference on Electrical Power Quality and Utilisation*. 2007.

[BKD21] C. Brantl, M. Knechtges, P. D"ullmann, et al.: “Requirements on offshore hvdc grid protection: interaction with ac system inertia and fast frequency support”. In: 41st Cigre Symposium, Ljubljana, Slovenia, 2021.

[BMW25] BMWK: *Connecting offshore wind energy to the grid*. https://www.bmwk.de/Redaktion/EN/Artikel/Energy/connecting-offshore-wind-energy-to-the-grid.html. Accessed: 2025-05-08. 2025.

[BPS18] N. A. Belda, C. A. Plet, R. P. P. Smeets: “Analysis of Faults in Multiterminal HVDC Grid for Definition of Test Requirements of HVDC Circuit Breakers”. In: *IEEE Transactions on Power Delivery* 33.1 (2018), pp. 403–411.

[BRM15] C. Buchhagen, C. Rauscher, A. Menze, et al.: *BorWin1 – First Experiences with harmonic interactions in converter dominated grids*. 2015.

[BRP20] C. Brantl, P. Ruffing, R. Puffer, eds.: *The application of line protection relays in high voltage AC transmission grids considering the capabilities and limitations of connected MMCs*. Institution of Engineering and Technology, 2020.

[BSC18] F. Bignucolo, R. Stecca, M. Coppo: “Advantages of the Virtual Synchronous Machine regulation for integrating Low-Inertia Variable Renewable Generation in Transmission Systems”. In: *53rd International Universities Power Engineering Conference (UPEC)*. 2018.

[BVB13] E. Belenguer, R. Vidal, H. Beltran, et al.: “Control strategy for islanded operation of offshore wind power plants connected through a VSCHVDC link”. In: *IECON 2013 - 39th Annual Conference of the IEEE Industrial Electronics Society*. IEEE, 2013, pp. 5254–5259.

[CEN18] CENELEC CLC/TS 50654-1: *HVDC Grid Systems and connected Converter Stations - Guideline and Parameter Lists for Functional Specifications - Part 1: Guidelines*. 2018.

[Cig04] Cigre: *Controlled switching of HVAC Circuit Breakers - TB 262*. CIGRÉ, 2004.

[Cig14] Cigre: *Guide for the Development of Models for HVDC Converters in a HVDC Grid - TB 604*. CIGRÉ, 2014.

[Cig15] Cigre: *Special considerations for AC collector systems and substations associated with HVDC-connected wind power plants - TB 612*. CIGRÉ, 2015.

[Cig16] Cigre: *Guidelines for the preparation of connection agreements or grid codes for multi-terminal DC schemes and DC grids - TB 657*. CIGRÉ, 2016.

[Cig19] Cigre: *Protection and local control of hvdc-grids: TB 739*. CIGRÉ, 2019.

[CLX22] J. Chu, Y. Lv, Y. Xu, et al., eds.: *Coordinated Control Strategy for Improving Frequency Stability of Offshore Wind Farms Connected to the Grid through MMC - HVDC Transmission*. IEEE, 2022.

[CSC22] M. Czernorucki, M. Salles, E. Costa, et al.: "Comprehensive Overview on HVDC Converter Transformer Design: Additional Discussions to the IEC/IEEE 60076-57-129 Standard". In: *IEEE Access* 10 (2022), pp. 40165–40180.

[CW18] V. Crastan, D. Westermann: *Elektrische Energieversorgung 3*. Springer Verlag, 2018.

[CWM18] O. Cwikowski, A. Wood, A. Miller, et al.: "Operating DC Circuit Breakers With MMC". In: *IEEE Transactions on Power Delivery* 33.1 (2018), pp. 260–270.

[DBK23] P. Düllmann, C. Brantl, C. Klein, et al.: "Interdependencies in HVDC grid protection: Impact of converter parameters and controls on DC fault–ride–through capabilities and protection system design". In: *IET Generation, Transmission & Distribution* 17.10 (2023), pp. 2356–2375.

[DBT22] P. Düllmann, C. Brantl, P. Tünnerhoff, et al.: "European offshore grid: On protectionsystem design for radial bipolar multi-terminal HVDC networks". In: *Cigre Paris Session 2022*. 2022.

[DDM23] P. Düllmann, M. Deitert, A. Moser: “Offshore HVDC Grids: Comparison and Sensitivity Analysis forn Fully and Partially Selective Protection System Design”. In: *Cigre B4 Colloquium, Vienna, Austria*. 2023.

[DKW24] P. Düllmann, C. Klein, P. Winter, et al.: “Preventive DC–side decoupling: A system integrity protection scheme to limit the impact of DC faults in offshore multi–terminal HVDC systems”. In: *IET Generation, Transmission & Distribution* (2024).

[DQB15] S. Debnath, J. Qin, B. Bahrani, et al.: “Operation, Control, and Applications of the Modular Multilevel Converter A Review”. In: *IEEE Transactions on Power Electronics* 30.1 (2015), pp. 37–53.

[DRB20] P. Düllmann, P. Ruffing, C. Brantl, et al.: “Interoperability among dc protection strategies based on fault blocking converters and DC circuit breakers within a multi-terminal HVDC system”. In: Institution of Engineering and Technology, 2020.

[DS13] S. D’Arco, J. A. Suul: “Virtual synchronous machines — Classification of implementations and analysis of equivalence to droop controllers for microgrids”. In: *2013 IEEE Grenoble Conference*. IEEE, 2013, pp. 1–7.

[DSF13] S. D’Arco, J. A. Suul, O. B. Fosso: “Control system tuning and stability analysis of Virtual Synchronous Machines”. In: *IEEE Energy Conversion Congress and Exposition*. 2013, pp. 2664–2671.

[EJT16] M. Eremia, J. A. Jardini, G. Tang, et al.: “VSC–HVDC Transmission”. In: *Advanced solutions in power systems: HVDC, FACTS, and artificial intelligence*. Ed. by M. Eremia, C.-C. Liu, A.-A. Edris. Vol. 52. IEEE Press and Wiley, 2016, pp. 125–267.

[Ene19] H. Energy: *Caithness Moray HVDC Link*. https://www.hitachienergy.com/news-and-events/customer-stories/caithness-moray-hvdc-link. Accessed: 2025-05-28. 2019.

[ENT16a] ENTSO-E: “Commission Regulation (EU) 2016/ 1447 - of 26 August 2016 - establishing a network code on requirements for grid connection of high voltage direct current systems and direct current-connected power park modules”. In: (2016).

[ENT16b] ENTSO-E: “Frequency Stability Evaluation Criteria for the Synchronous Zone of Continental Europe”. In: 2016.

[ENT24] ENTSO-E: *Sea-Basin ONDP Report - TEN-E Offshore Priority Corridor: Northern Seas Offshore Grids*. https://eepublicdownloads.blob.core.windows.net/public-cdn-container/tyndp-documents/ONDP2024/web_entso-e_ONDP_NS_240226.pdf. Accessed: 2025-08-27. 2024.

[Eur17] European Comission: “Commission Regulation (EU) 2017/1485 of 2 August 2017 establishing a guideline on electricity transmission system operation”. In: *Official Journal of the European Union* (2017).

[Eur24] European Comission: “Non-binding agreement on goals for offshore renewable generation in 2050 with intermediate steps in 2040 and 2030 for priority offshore grid corridor Northern Seas offshore grids (NSOG) pursuant to Article 14(1) of the TEN-E Regulation (EU) 2022/869”. In: (2024).

[Eur25] European Comission: *Offshore renewable energy*. https://energy.ec.europa.eu/topics/renewable-energy/offshore-renewable-energy_en. Accessed: 2025-05-08. 2025.

[FRR25] J. S. Farkhani, P. J. Randewijk, T. Roosea, et al.: “A novel TQWT based protection and coordination scheme in multiterminal VSCHVDC systems”. In: *Electric Power Systems Research* 241 (2025).

[Gmb24] T. T. GmbH: “Netzanschlussregeln”. In: (2024).

[Gök17] Ö. Göksu: “Black Start and Island Operation Capabilities of Wind Power Plants”. In: *Wind Integration Workshop proceeding* (2017).

[GSP22] D. Gross, E. Sánchez-Sánchez, E. Prieto-Araujo, et al.: “Dual-Port Grid-Forming Control of MMCs and Its Applications to Grids of Grids”. In: *IEEE Transactions on Power Delivery* 37.6 (2022), pp. 4721–4735.

[HAN13] L. Harnefors, A. Antonopoulos, S. Norrga, et al.: “Dynamic Analysis of Modular Multilevel Converters”. In: *IEEE Transactions on Industrial Electronics* 60.7 (2013), pp. 2526–2537.

[Hau17] E. Hau: *Windkraftanlagen: Grundlagen Technik Einsatz Wirtschaftlichkeit*. Springer Verlag, 2017.

[HN23] M. Hjelmeland, J. K. Nøland: “Correlation challenges for North Sea offshore wind power: a Norwegian case study”. In: *Scientific Reports* 13.1 (2023).

[HWZ23] L. Huang, C. Wu, D. Zhou, et al.: “Challenges and potential solutions of grid-forming converters applied to wind power generation system—An overview”. In: *Frontiers in Energy Research* 11 (2023).

[Inf21] Infineon Technologies AG: *Data Sheet FZ1500R33HE3, V3.3*. https://www.infineon.com/dgdl/Infineon-FZ1500R33HE3-DataSheet-v01_10-EN.pdf?fileId=db3a304314dcak389011527dfc61411c3. Accessed: February 02 2025. 2021.

[JDG18] A. Jain, K. Das, Ö. Göksu, et al.: “Control Solutions for Blackstart Capability and Islanding Operation of Offshore Wind Power Plants”. In: *Control Solutions for Blackstart Capability and Islanding Operation of Offshore Wind Power Plants*. 2018.

[Jov19] D. Jovic: *High Voltage Direct Current Transmission*. John Wiley and Sons, Ltd, 2019.

[JSC20] A. Jain, J. N. Sakamuri, N. A. Cutululis: “Grid-forming control strategies for black start by offshore wind power plants”. In: *Wind Energy Science* 5.4 (2020), pp. 1297–1313.

[JSS21a] A. Jain, O. Saborío–Romano, J. N. Sakamuri, et al.: “Blackstart from HVDC–connected offshore wind: Hard versus soft energization”. In: *IET Renewable Power Generation* 15.1 (2021), pp. 127–138.

[JSS21b] A. Jain, O. Saborío-Romano, J. N. Sakamuri, et al.: *Virtual Resistance Control for Sequential Green-start of Offshore Wind Power Plants*. 2021.

[KDL25] C. Klein, P. Düllmann, G. Love, et al.: “Operating point dependent DC-FRT requirements in partially-selective MT-HVDC protection - North Sea Wind Power Hub pre-FEED study”. In: *Cigre Symposium 2025, Trondheim, Norway*. 2025.

[KDM22] C. Klein, P. Düllmann, A. Moser: “Post-Fault Power Flow Control for Multi-Terminal Bipolar HVDC Systems Connecting Offshore Wind Farms”. In: *IEEE 7th Southern Power Electronics Conference (SPEC)*. 2022.

[KDO23] C. Klein, P. Düllmann, L. Osterkamp, et al.: “Black start of HVDC links via grid-forming wind turbines: sensitivity analysis and technical requirements”. In: *22nd Wind and Solar Integration Workshop*. 2023.

[KDO25] C. Klein, P. Düllmann, L. Osterkamp, et al.: “HVDC system energization via grid-forming offshore wind turbines: sensitivity analysis and technical requirements”. In: *IET Renewable Power Generation* (2025).

[KHL25] C. Klein, M. Hagmans, W. Leterme: “Post DC-side fault system restoration via grid forming wind turbine generators”. In: *Unpublished manuscript, submitted for publication at the time of thesis submission* (2025).

[Kle24] C. Klein: *Abschlussbericht: HVDC BLADE, Demonstration der Schwarzstartfähigkeit von über HGÜ-angebundenen Offshore Windparks*. 2024.

[KTH25] C. Klein, H. Thomas, M. Hagmans, et al.: “Enabling Temporary Blocking of Offshore Converters through Grid-Forming Wind Turbines to Assist HVDC Grid Protection”. In: *IET Generation, Transmission and Distribution* (2025).

[LKD25] G. Love, D. T. A. Kho, P. Düllmann, et al.: *Expandable & Compatible HVDC Grid Design*. 2025.

[Lok22] F. Loku: “On converter control interoperability in multi-terminal HVDC networks”. PhD thesis. 2022.

[LSK05] H. Laaksonen, P. Saari, R. Komulainen: “Voltage and frequency control of inverter based weak LV network microgrid”. In: *2005 International Conference on Future Power Systems*. 2005, 6 pp.–6.

[Lv15] W. Leterme, D. van Hertem: “Classification of Fault Clearing Strategies for HVDC Grids”. In: *Cigre Lund*. 2015.

[LXZ15] B. Li, D. Xu, Y. Zhang, et al.: “Closed-Loop Precharge Control of Modular Multilevel Converters During Start-Up Processes”. In: *IEEE Transactions on Power Electronics* 30.2 (2015), pp. 524–531.

[Man18] Manitoba Hydro International: *Type 4 wind turbine model v46*. https://www.pscad.com/knowledge-base/article/227. Accessed: 2025-05-28. 2018.

[Nor25] North Sea Wind Power Hub. 2025.

[NTK98] T. Noguchi, H. Tomiki, S. Kondo, et al.: “Direct power control of PWM converter without power-source voltage sensors”. In: *IEEE Transactions on Industry Applications* 34.3 (1998), pp. 473–479.

[OTO24] D. Orihara, H. Taoka, K. Otani: “Influence of Wind-Turbine-Generator Power Control on the Performance of a Virtual Synchronous Machine”. In: *Energies* 17.1 (2024), p. 234.

[PBB20] D. Pagnani, F. Blaabjerg, C. L. Bak, et al.: “Offshore Wind Farm Black Start Service Integration: Review and Outlook of Ongoing Research”. In: *Energies* 13.23 (2020), p. 6286.

[PKH22] D. Pagnani, L. Kocewiak, J. Hjerrild, et al.: “Control Principles for Island Operation and Black Start by Offshore Wind Farms integrating Grid-Forming Converters”. In: *24th European Conference on Power Electronics and Applications (EPE’22 ECCE Europe)*. 2022.

[PRO16a] PROMOTioN: *Deliverable 2.1: Grid topology and model specification*. 2016.

[PRO16b] PROMOTioN: *Deliverable 5.1: HVDC Network Fault Analysis*. http://www.promotion-offshore.net/fileadmin/PDFs/D5.1_PROMOTioN_Deliverable_5.1_HVDC_Network_Fault_Analysis.pdf. 2016.

[PRO17] PROMOTioN: *Deliverable 4.2: Broad comparison of fault clearing strategies for dc grids*. http://www.promotion-offshore.net/fileadmin/PDFs/D4.2_Broad_comparison_of_fault_clearing_strategies_for_DC_grids.pdf. 2017.

[RCB19a] P. Ruffing, N. Collath, C. Brantl, et al.: “DC Fault Control and High-Speed Switch Design for an HVDC Network Protection Based on Fault-Blocking Converters”. In: *IEEE Transactions on Power Delivery* 34.1 (2019), pp. 397–406.

[RCB19b] P. Ruffing, N. Collath, C. Brantl, et al.: “DC Fault Control and High-Speed Switch Design for an HVDC Network Protection Based on Fault-Blocking Converters”. In: *IEEE Transactions on Power Delivery* 34.1 (2019), pp. 397–406.

[REL20] R. Rosso, S. Engelken, M. Liserre: “Robust Stability Investigation of the Interactions Among Grid-Forming and Grid-Following Converters”. In: *IEEE Journal of Emerging and Selected Topics in Power Electronics* 8.2 (2020), pp. 991–1003.

[RGS20] J. Rimez, K. Geens, L. Schyvens, et al.: “Black start and system restoration utilizing a the NEMO Modular Multilevel Converter – a practical test in the Belgium transmission system”. In: *Session 48* (2020).

[RLB12] J. Rocabert, A. Luna, F. Blaabjerg, et al.: “Control of Power Converters in AC Microgrids”. In: *IEEE Transactions on Power Electronics* 27.11 (2012), pp. 4734–4749.

[RM23] H. Ramadan, Y. Mohamed: “Assessment and Mitigation of DC Breaker Impacts on VSC-MTDC Grid Equipped with Power Flow Controller”. In: *IEEE Open Journal of Power Electronics* PP (Jan. 2023), pp. 1–14.

[Ruf20] P. Ruffing: “HVDC Grid Protection Based on Fault Blocking Converters”. PhD thesis. 2020.

[RWL21] R. Rosso, X. Wang, M. Liserre, et al.: “Grid-Forming Converters: Control Approaches, Grid-Synchronization, and Future Trends—A Review”. In: *IEEE Open Journal of Industry Applications* 2 (2021), pp. 93–109.

[SAL20] L. Shi, G. P. Adam, R. Li, et al.: “Enhanced Control of Offshore Wind Farms Connected to MTDC Network Using Partially Selective DC Fault Protection”. In: (2020).

[SAL21] L. Shi, G. P. Adam, R. Li, et al.: “Enhanced Control of Offshore Wind Farms Connected to MTDC Network Using Partially Selective DC Fault Protection”. In: *IEEE Journal of Emerging and Selected Topics in Power Electronics* 9.3 (2021), pp. 2926–2935.

[SGB19] J. N. Sakamuri, O. Göksu, A. Bidadfar, et al.: “Black Start by HVdc-connected Offshore Wind Power Plants”. In: *IECON 2019 - 45th Annual Conference of the IEEE Industrial Electronics Society*. 2019.

[SHN16] K. Sharifabadi, L. Harnefors, H. P. Nee, et al.: *Design, control, and application of modular multilevel converters for HVDC transmission systems*. IEEE Press Wiley, 2016.

[SLW15] X. Shi, B. Liu, Z. Wang, et al.: “Modeling, Control Design, and Analysis of a Startup Scheme for Modular Multilevel Converters”. In: *IEEE Transactions on Industrial Electronics* (2015), pp. 7009–7024.

[SS11] M. Singh, S. Santoso: “Dynamic Models for Wind Turbines and Wind Power Plants”. In: *Wind Power: Systems Engineering Applications and Design Models* (2011).

[STV24] K. Shinoda, P. Torwelle, P. Verrax: *Functional requirements for HVDC grid systems and subsystems*. InterOPERA project. 2024.

[SVS10] M. Singh, M. Vyas, S. Santoso: “Using generic wind turbine models to compare inertial response of wind turbine technologies”. In: *IEEE Power and Energy Society general meeting, 2010: IEEE PES-GM 2010 ; 25 - 29 July 2010, Minneapolis, Minnesota, USA*. IEEE, 2010, pp. 1–7.

[TLR11] R. Teodorescu, M. Liserre, P. Rodriguez: *Grid Converters for Photovoltaic and Wind Power Systems*. Wiley-IEEE Press, 2011.

[TRJ23] E. Taherzadeh, H. Radmanesh, S. Javadi, et al.: “Circuit breakers in HVDC systems: state-of-the-art review and future trends”. In: *Protection and Control of Modern Power Systems* 8.1 (2023).

[TV07] M. Tarafdar Hagh, M. Valizadeh: "Analysis and comparative study of transient inrush current reduction methods". In: *2007 International Power Engineering Conference (IPEC 2007)*. 2007, pp. 287–291.

[Übe24] Übertragungsnetzbetreiber: *Netzentwicklungsplan Strom 2037 mit Ausblick 2045: German network development plan 2037*. 2024.

[Uni18] United Nations: *Paris Agreement*. 2018.

[UNS20] P. Unruh, M. Nuschke, P. StrauSS, et al.: "Overview on Grid-Forming Inverter Control Methods". In: *Energies* 13.10 (2020), p. 2589.

[VDE19] VDE: "Technische Regeln für den Anschluss von HGÜ-Systemen und über HGÜ-Systeme angeschlossene Erzeugungsanlagen (TAR HGÜ): VDE-AR-N 4131". In: (2019).

[VF20a] VDE, FNN: *FNN-Guideline Grid forming behaviour of HVDC systems and DC-connected PPMs*. 2020.

[VF20b] VDE, FNN: *Spannungseinprägendes Verhalten von HGÜ-Systemen und nichtsynchronen Erzeugungsanlagen mit Gleichstromanbindung*. 2020.

[vGL16] D. van Hertem, O. Gomis-Bellmunt, J. Liang: *HVDC grids: For offshore and supergrid of the future*. IEEE Press and Wiley, 2016.

[Win19] Wind Europe: *Our Energy Our Future*. 2019.

[WTW20] X. Wang, M. G. Taul, H. Wu, et al.: "Grid-Synchronization Stability of Converter-Based ResourcesAn Overview". In: *IEEE Open Journal of Industry Applications* (2020), pp. 115–134.

[YLX18] L. Yu, R. Li, L. Xu: "Distributed PLL-Based Control of Offshore Wind Turbines Connected With Diode-Rectifier-Based HVDC Systems". In: *IEEE Transactions on Power Delivery* 33.3 (2018), pp. 1328–1336.

[ZHN10] L. Zhang, L. Harnefors, H.-P. Nee: "Power-Synchronization Control of Grid-Connected Voltage-Source Converters". In: *IEEE Transactions on Power Systems* 25.2 (2010), pp. 809–820.

[ZJ19a] M. Zaja, D. Jovcic, eds.: *Coordination of Mechanical DC-CBs and Temporary Blocking of Half Bridge MMC*. Institution of Engineering and Technology, 2019.

[ZJ19b] M. Zaja, D. Jovcic, eds.: *Coordination of Mechanical DC-CBs and Temporary Blocking of Half Bridge MMC*. Institution of Engineering and Technology, 2019.

[ZJK20] M. Zaja, D. Jovcic, L. Kunjumuhammed, et al., eds.: *Generic and simplified HV DC circuit breaker models for grid-level studies*. IEEE, 2020.

Glossaries

List of acronyms

AC-FRT	AC Fault-ride-through
ACCB	AC Circuit Breaker
CO	Continous Operation
DC-FRT	DC Fault-ride-through
DCCB	DC Circuit Breaker
DCR	DC Reactor
DMR	Dedicated Metallic Return
EMT	Electromagnetic Transient
EU	European Union
F-S	Fully-selective
FRT	Fault-ride-through
GFL	Grid Following
GFL WTG	Grid Following Wind Turbine Generator
GFM	Grid Forming
GFM WTG	Grid Forming Wind Turbine Generator
HBSM	Half-bridge Submodule
HVDC	High Voltage Direct Current
IGBT	Insulated Gate Bipolar Transistor
KPI	Key Performance Indicator
LCC	Line-commutated Converter
LVRT	Low-voltage Ride-through

MMC	Modular Multilevel Converter
MTDC	Multi Terminal HVDC
N-S	Non-selective
OWPP	Offshore Wind Power Plant
P-S	Partially-selective
PG	Pole-to-ground
PIR	Pre-insertion Resistor
PIT	Pre-insertion Time
PLL	Phase-locked Loop
PMSG	Permanent-magnet Synchronous Generator
PS	Permanent Stop
PtP	Point-to-point
RES	Renewable Energy Source
SM	Submodule
TS	Temporary Stop
VSC	Voltage Source Converter
VSM	Virtual Synchronous Machine
WTG	Wind Turbine Generator

List of symbols

ρ	Air density
θ_{PLL}	Determined phase angle via PLL
θ_{GFM}	Grid power factor for GFM control
$\phi_{\mathrm{AC,conv}}$	AC voltage angle at the onshore converter terminal
$\phi_{\mathrm{AC,grid}}$	AC voltage at angle of the grid behind the breaker
$C_{\mathrm{SM,tot}}$	Total submodule capacitance
C_{f}	Filter capacitance
C_{SM}	Submodule capacitance
C_{DC}	WTG DC link capacitance
C_{p}	WTG power coefficient
I_{GS}	Measured grid side current WTG
I_{f}	Measured filered grid side current WTG
$i_{\mathrm{ac,i}}$	AC current per phase
$i_{\mathrm{ac},a}$	AC phase current a
$i_{\mathrm{ac},b}$	AC phase current b
i_{arm}	Arm current
$i_{\mathrm{arm,max}}$	Maximum arm current
i_{cap}	Submodule capacitor current
$i\mathrm{cc},i$	Circulating current between the arms
i^*_{ac}	MMC control AC current reference
i^*_{cc}	MMC control circulating current reference
i^*_{dc}	MMC control DC current reference
$I_{\mathrm{max,GS}}$	Maximum current limit of the grid-side WTG voltage controller

$I_{\mathrm{max,MS}}$	Maximum current limit of the machine-side WTG voltage controller
$I_{\mathrm{min,GS}}$	Minimum current limit of the grid-side WTG voltage controller
$I_{\mathrm{min,MS}}$	Minimum current limit of the machine-side WTG voltage controller
I_{DC}	DC current
$i_{\mathrm{DC,n}}$	DC current lower arm
$i_{\mathrm{DC,p}}$	DC current upper arm
$i_{\mathrm{dc},i}$	DC current per phase arm
$i_{\mathrm{diff},i}$	Difference current
i_{d}	d-component of the current in the VSM control
I_{ac}	AC phase rms current
$i_{\mathrm{ac},c}$	Ac phase current c
I_{GFL}	Reference current of the GFL control
I_{d}^{*}	d-component of the reference current of the GFL control
I_{q}^{*}	q-component of the reference current of the GFL control
I_{g}	Measured grid current
I_{g}^{d}	Measured grid current d-component
I_{g}^{q}	Measured grid current q-component
$i_{\mathrm{n},i}$	Lower arm current
i_{q}	q-component of the current in the VSM control
I_{SM}	Submodule current
$I_{\mathrm{SM,max}}$	Maximum permissible submodule current
$i_{\mathrm{p},i}$	Upper arm current
D_1	Diode 1
D_2	Diode 2

E_{chop}	Dissipated chopper energy
$E_{\mathrm{SM,tot}}$	Total submodule energy
k_{f}	Frequency factor for feed forward
k_{v}	Voltage factor for feed forward
f	Frequency
f_{FF}	Frequency feed forward
f^*	Frequency setpoint
f_{SW}	Coverter switching frequency WTG
$k_{\mathrm{i,p,GS}}$	Proportional gain of the grid-side WTG current controller
$k_{\mathrm{i,i,GS}}$	Integral gain of the grid-side WTG current controller
K_{Q}	Droop constant Q/V droop
$k_{\mathrm{dc,p,MS}}$	Integral gain of the machine-side WTG DC voltage controller
$k_{\mathrm{PLL,p,MS}}$	Integral gain of the machine-side WTG voltage controller
$k_{\mathrm{pitch,p,MS}}$	Integral gain of the machine-side WTG voltage controller
$k_{\omega,\mathrm{p,MS}}$	Integral gain of the machine-side WTG voltage controller
$k_{\mathrm{PLL,i,MS}}$	Proportional gain of the machine-side WTG voltage controller
$k_{\mathrm{pitch,i,MS}}$	Proportional gain of the machine-side WTG voltage controller
$k_{\omega,\mathrm{i,MS}}$	Proportional gain of the machine-side WTG voltage controller
$k_{\mathrm{dc,i,MS}}$	Proportional gain of the machine-side WTG DC voltage controller

$k_{\mathrm{v,p,GS}}$	Proportional gain of the grid-side WTG voltage controller
$k_{\mathrm{v,i,GS}}$	Integral gain of the grid-side WTG voltage controller
$k_{\mathrm{Vac,p,MS}}$	Proportional gain of the machine-side WTG voltage controller
$k_{\mathrm{Vac,i,MS}}$	Integral gain of the machine-side WTG voltage controller
K_{D}	Damping coefficient of the VSM
T_{J}	VSM inertia time constant
K_{P}	Active power droop constant
K_{DC}	DC voltage droop constant
T_1	Switching state of IGBT 1
T_2	Switching state of IGBT 2
V_{c}	Voltage of the converter
Z_{c}	Impedance of the converter
Z_{g}	Impedance of the grid
L_{f}	Filter inductance
L_{BRK}	Inductance of the DCCB series DCR
X_{F}	Inductance of the converter filter
X	Inductance of the GFL control
X	Inductance of the GFM control
X_{T}	Inductance of the converter transformer
$X_{\mathrm{trafo,WTG}}$	WTG transformer inductance
L_{i}	Inner inductance of the voltage source
L_{arm}	Arm inductance
L_{DC}	DC terminal inductance
L_{T}	Transformer inductance

$l_{\text{cable,AC}}$	length of the AC cable
l_{Pi}	length of the DC cable
M	Modulation index
N_{SM}	Number of Submodules
θ_{G}	Voltage phase angle of the grid
θ_{diff}	Phase angle difference between grid and WTG
θ_{GS}	Voltage phase angle of WTG grid side
ϕ	Grid angle
θ_{pitch}	WTG blade pitch angle
P	Active power
P_{D}	Damped active power
P_{e}	Electrical power
P_{GFL}	Transferred active power in GFL control
P_{GFM}	Transferred active power in GFM control
P_{WTG}	Measured active power output WTG
P_{m}	WTG mechanical power
P_{MMC}	Active power output of the MMC
$P_{\text{AC,WTG1}}$	Active power of WTG1 at HV-side
$P_{\text{AC,WTG}}$	Aactive power of the WTG at HV-side
$P_{\text{AC,off}}$	Total active power at the MMC offshore busbar
P_{DC}	Total active power at the MMC offshore busbar
$Q_{\text{AC,WTG1}}$	Reactive power of WTG1 at HV-side
$Q_{\text{AC,WTG}}$	Reactive power of the WTG at HV-side
$P_{\text{AC,on}}$	Total active power at the MMC onshore AC busbar
P_{r}	Rated active power
P^*_{WTG}	Active power reference WTG

P^*	Active power setpoint
$P_{\mathrm{SM,charge}}$	Active power required for submodule charging
S_{r}	Rated power
$S_{\mathrm{r,WTG}}$	Rated power WTG
Q_{GFL}	Transferred reactive power in GFL control
Q_{GFM}	Transferred reactive power in GFM control
Q_{MS}	Measured reactive power output machine side WTG
Q_{WTG}	Measured reactive power output WTG
Q_{r}	Rated reactive power
Q^*_{WTG}	Reactive power reference WTG
Q^*	Reactive power setpoint
R	WTG blade radius
R_{arm}	Resistance of the arm inductor
R_{DC}	Resistance of the DC-side
R_{PIR}	Resistance of the pre-insertion resistor
R_{var}	Variable resistance at connection point
R_{i}	Inner resistance of the voltage source
R_{T}	Transformer resistance
Ω_{t}	Rotor angle speed
D	System damping
J	System intertia
$T_{1,\mathrm{n},i,j}$	Switching state of IGBT 1 in the lower arm for each SM within the MMC
$T_{1,\mathrm{p},i,j}$	Switching state of IGBT 1 in the upper arm for each SM within the MMC
t_{DCCB}	DCCB opening time

$t_{\mathrm{DCCB,open}}$	Total DCCB opening time
t_{det}	Fault detection time
t_{protBLK}	Time until protective converter blocking
$t_{\mathrm{P,AC,rec}}$	Time for system recovery to 10 % tolerance band of pre-fault power
$t_{\mathrm{rec1,AC}}$	Time until DC voltage recovery has to be started
$t_{\mathrm{rec2,AC}}$	Time until undervoltage operation requirement has to be reached
$t_{\mathrm{rec1,DC}}$	Time until DC voltage recovery has to be started
$t_{\mathrm{rec2,DC}}$	Time until DC undervoltage operation requirement has to be reached
$t_{\mathrm{st,DC}}$	Time until DC stationary voltage band has to be reached
$t_{\mathrm{st,DC}}$	Time until DC stationary voltage band has to be reached
t_{fault}	Time uof DC-side fault occurence
t_{tempBLK}	Time of the temporary blocking
λ	WTG tip speed rotation
T^*	Reference tourque for PMSG
$v_{\mathrm{cap},j}$	SM capacitor voltage of the j-th SM
V_{AC}	AC voltage
$V_{\mathrm{AC,conv}}$	AC voltage at the onshore converter terminal
$V_{\mathrm{AC,grid}}$	AC voltage of the grid behind the breaker
$\epsilon_{\mathrm{ac},i}$	Equivalent AC voltage
ϵ_{ac^*}	AC submodule voltage control reference
$V_{\mathrm{AC,i}}$	AC voltage per phase
$\hat{v}_{\mathrm{ac,sec}}$	Peak secondary side voltage

$V_{\mathrm{AC,rms}}$	RMS AC side voltage
v_{cap}	Submodule capacitor voltage
ϵ_{cc^*}	Circulating current submodule voltage control reference
$V_{\mathrm{max,GS}}$	Maximum voltage limit of the grid-side WTG voltage controller
$V_{\mathrm{max,MS}}$	Maximum voltage limit of the machine-side WTG voltage controller
$V_{\mathrm{min,GS}}$	Minimum voltage limit of the grid-side WTG voltage controller
$V_{\mathrm{min,MS}}$	Minimum voltage limit of the machine-side WTG voltage controller
$V_{\mathrm{DC,ref}}$	DC voltage reference
V_{DC}	DC voltage
$\epsilon_{\mathrm{dc},i}$	Equivalent voltage of i-th submodules
ϵ_{dc^*}	DC submodule voltage control reference
$V_{\mathrm{DC,faulty}}$	DC voltage in the faulty part of the P-S protected system
$V_{\mathrm{DC,healthy}}$	DC voltage in the healthy part of the P-S protected system
$V_{\mathrm{DC,meas}}$	DC voltage measurment
$V_{\mathrm{DC,min}}$	DC undervoltage limit
$V_{\mathrm{DC,n}}$	DC voltage N pole
$V_{\mathrm{DC,p}}$	DC voltage P pole
$V^*_{\mathrm{DC,WTG}}$	WTG DC-link voltage
$V_{\mathrm{DC,WTG}}$	WTG DC-link voltage
$\epsilon_{\mathrm{cc},i}$	Voltage difference between the arms
$V_{\mathrm{diff,WTG}}$	Difference of grid and converter voltage
V_{FF}	Voltage feed forward

V_{MS}	Machine-side voltage WTG
$V_{\mathrm{ref,GFL}}$	Reference voltage for the switching signals
V_{g}^{d}	Measured grid voltage d-component
V_{g}	Measured grid voltage
$V_{\mathrm{g,1}}$	Measured grid voltage primary side
$V_{\mathrm{g,2}}$	Measured grid voltage secondary side
V_{GS}	Grid-side converter voltage WTG
V_{g}^{q}	Measured grid voltage q-component
$v_{\mathrm{n},i}$	Lower arm voltage
$V_{\mathrm{AC,off,min}}$	Minimum AC voltage for soft energization
$V_{\mathrm{AC,off}}$	AC voltage of the OWPP at the MMC offshore busbar
$V_{\mathrm{AC,on}}$	Onshore AC voltage at the MMC onshore terminal
$v_{\mathrm{OV,TR1}}$	Overvoltage transient requirement
$v_{\mathrm{OV,TR2}}$	Overvoltage transient requirement
$v_{\mathrm{OV,OR}}$	Overvoltage operational requirement
v_{a}	Phase voltage a
v_{b}	Phase voltage a
v_{c}	Phase voltage a
$\hat{v}_{\mathrm{av}}$	Peak AC voltage
$v_{\mathrm{ac,prim}}$	Nominal primary side voltage
$v_{\mathrm{ac,sec}}$	Nominal secondary side voltage
$V_{\mathrm{ac,1,off}}$	Nominal primary side offfshore voltage
$V_{\mathrm{ac,1,on}}$	Nominal primary side onshore voltage
V_{GFM}	Voltage reference of the GFM control
V^{*}	Q/V droop voltage reference
$V_{\mathrm{SM,pu,ref}}$	Reference submodule voltage in p.u.

$V_{\mathrm{GS,ref}}$	Grid-side converter reference voltage WTG
V^*_{GS}	Grid-side converter reference voltage WTG
$V_{\mathrm{MS,ref}}$	Machine-side converter reference voltage WTG
V^*_{MS}	Machine-side converter reference voltage WTG
$V_{\mathrm{ac,2,off}}$	Nominal secondary side offfshore voltage
$V_{\mathrm{ac,2,on}}$	Nominal secondary side onshore voltage
V_{G}	Grid voltage WTG type
V^*	Voltage setpoint
V_{SM}	Submodule voltage
$v_{\mathrm{SM,nom}}$	Maximum submodule voltage
$V_{\mathrm{SM,nom}}$	Nominal submodule voltage
$V_{\mathrm{SM,C2}}$	Submodule voltage of covverter C2
$V_{\mathrm{SM,pre,AC}}$	Maximum submodule voltage AC pre charge value
$V_{\mathrm{SM,pre,AC,pu}}$	Maximum submodule voltage AC pre charge value in pu
$V_{\mathrm{SM,pre,DC}}$	Maximum submodule voltage DC pre charge value
$V_{\mathrm{SM,pre,DC,pu}}$	Maximum submodule voltage DC pre charge value in pu
$V_{\mathrm{SM,pu}}$	Submodule voltage in p.u.
$v_{\mathrm{UV,CR}}$	Undervoltage connection requirement
$v_{\mathrm{UV,OR}}$	Undervoltage operational requirement
$\epsilon_{\mathrm{diff},i}$	Upper arm voltage
$v_{\mathrm{p},i}$	Upper arm voltage
ω_{WTG}	Angular frequency
ω	Angular frequency
v_{wind}	Wind speed

List of Figures

1.1 Development of the installed capacities in the North Sea [ENT24] 1
1.2 Sketch of the development of HVDC systems 3
1.3 Change in controls needed to achieve operational flexibility of offshore HVDC system [Kle24] 4
1.4 Overview of different HVDC architectures and topologies a) MTDC system, b) sym. monopole c) asym. monopol d) Bipol (DMR dashed) e) AC coupling 10
1.5 Overview of different protection philosophies a) non-selective, b) partially-selective, c) fully-selective 13
1.6 Overview of the thesis structure 16

2.1 Schematic drawing of two connection topologies for an OWPP a) 66 kV direct connection, b) 33/150 kV connection with AC offshore platforms [Cig15] 20
2.2 Schematic drawing of a type-4 WTG 22
2.3 Schematic drawing of an MMC [SHN16] 23
2.4 Schematic drawing of an HBSM [DQB15] 24
2.5 Block diagram GFL controlled VSC [RLB12, RWL21] . . . 28
2.6 Working principle GFL controlled VSC [RLB12, RWL21] . 30
2.7 Block diagram of a GFM controlled VSC [RLB12, RWL21] 32
2.8 Working principle of GFM controlled VSC [RLB12, RWL21] 32
2.9 Schematic drawing of the initial AC-side energization of the MMC [LXZ15] 36
2.10 Schematic drawing of the initial DC-side energization of the MMC [LXZ15] 37

3.1 Schematic drawing of the OWPP models with a) full aggregation green: 25 WTG aggregation, blue: 35 WTG aggregation, b) partial aggregation 41
3.2 Schematic drawing of the WTG model 42
3.3 Block diagram of implemented VSM control [KDO23] . . . 44
3.4 Schematic drawing of the a) monopolar system b) bipolar system c) MMC model 47

3.5 MMC cascaded control architecture (orange: V_{DC}, green: P, dark green: V_{AC}/f droop (GFM))[Ruf20] 50
3.6 Schematic drawing of the implemented breaker topology [ZJ19b] 51

4.1 System overview for the energization study, red: Initial black started WTG, black: Single WTG, green: 25 WTG aggregation, light green: 35 WTG aggregation [KDO25] . . 54
4.2 Charging of all downstream turbines via WTG 1. a) Machine side power; (b) DC-link voltage; and (c) Reactive power . . 56
4.3 Transient behavior of subsystems A-D upon transformer connection and bypass of PIR (i) Connection through AC breaker ii) Bypass of PIR [KDO25] 58
4.4 PIR placement in the offshore system, grey + black) Full redundancy, black) minimum PIRs for sequential hard start 59
4.5 Start-up sequence of the OWPP with values of WTG 1[KDO23] 61
4.6 Start-up sequence of subsystem A, a) RMS voltage of the WTG at HV-side, b) Reactive power of the WTG at HV-side [KDO25] 63
4.7 Start-up sequence of the subsystems B-D a) RMS voltage measured at the transformer of Cluster A-D, b) Active and reactive power HV-side WTG 1 64
4.8 Overall energization process of the HVDC link: (a) DC voltage, (b) DC current,(c) DC active power, (d) Average submodule arm voltages (e) AC voltage secondary side, (f) AC current, (g) AC side power, (h) AC voltage [KDO23, KDO25] 66
4.9 Start-up sequence of the subsystems B-D a) RMS voltage measured at the transformer of Cluster A-D, b) Active and reactive power HV-side WTG 1 [KDO25] 67
4.10 Load steps: (a) HV-side voltage WTG1 (b) Active power WTG1, (c) AC voltage onshore, (d) Active power onshore [KDO23, KDO25] 69
4.11 Load steps: (a) HV-side voltage WTG1 (b) Active power WTG1, (c) AC voltage onshore, (d) Active power onshore [KDO23, KDO25] 70

4.12 Synchronization with a grid source equivalent (dashed: source, solid: converter): (a) Onshore voltage, (b) Active power [KDO25] 72
4.13 Soft energization of the overall system for different ramp rates: (a) RMS voltage at C2 (b) DC voltage at C2 (c) AC active power of C2 [KDO25] 74
4.14 Yearly wind power in % per h/year [Cig15] 81

5.1 DC-side fault isolation (1.) and possible restoration (2.), a) Fault on onshore connection, b) fault on interconnection [KHL25] 85
5.2 Flow chart of the restoration process [KHL25] 89
5.3 Flow chart of the restoration process [KHL25] 90
5.4 Fault isolation (a) Offshore voltage, (b) Active power, (c) Submodule voltage (d) WTG DC-link voltage [KHL25] . . . 92
5.5 Soft (left) and hard (right) energization of MMC 2 (uncontrolled charging) ab) Offshore voltage, cd) Active power, ef) MMC 2 submodule voltage, gh) DC-link voltage [KHL25] . 95
5.6 Controlled MMC energization and System energization: a) OWPP AC rms voltage, b) AC side active power, c) Submodule voltages (dashed: onshore, solid: offshore), d) WTG DC-link voltage [KHL25] 97
5.7 Reconnection of MMC2 and MMC4 via the DCCB (a OWPP AC rms voltage, b) AC side active power, c) DC side voltage, d) Submodule voltages (dashed: offshore, solid: onshore), e) WTG DC-link voltage [KHL25] 98

6.1 System under investigation, (a) Comparison without blocking (b) Temporary blocked converter during fault occurrence [KTH25] 104
6.2 Flow chart of the temporary blocking sequence 107
6.3 DC-FRT profile [STV24, Cig16], AC-FRT profile [VDE19] [KTH25] 109
6.4 Implemented V_{AC}/f droop to adjust P [KTH25] 111
6.5 Comparison of the different scenarios without blocking: a) Onshore AC power, b) DC voltage, c) Offshore AC voltage d) Avg. submodule voltage C3 (solid) C4 (dash), e) WTG DC link-voltage [KTH25] 113

6.6 Comparison different temporary blocking times of DC-FRT 2: a) Onshore AC power, b) DC voltage, c) Offshore AC voltage d) Avg. submodule voltage C3 (solid) C4 (dash), e) WTG DC link-voltage [KTH25] 115
6.7 Comparison different temporary blocking times of DC-FRT 3: a) Onshore AC power, b) DC voltage, c) Offshore AC voltage d) Avg. submodule voltage C3 (solid) C4 (dash), e) WTG DC link-voltage [KTH25] 116
6.8 Comparison different temporary blocking times of DC-FRT 4: a) Onshore AC power, b) DC voltage, c) Offshore AC voltage d) Avg. submodule voltage C3 (solid) C4 (dash), e) WTG DC link-voltage [KTH25] 118
6.9 Comparison different temporary blocking times of DC-FRT 4: a) rotational speed of the wind turbine, b) reactive power of the wind turbine [KTH25] 119

7.1 Overview of different system control scenarios (Single line diagram) (This figure has been reproduced with permission from Energynautics GmbH, 2024) 122
7.2 Visualization of load flow of Case 3 (cf. Table 7.1) (This figure has been reproduced with permission from Energynautics GmbH, 2024) 125
7.3 Comparison of the three scenarios for values at C1 (a) DC voltage, (b) DC active power, (c) AC active power (This figure has been reproduced with permission from Energynautics GmbH, 2024) 127
7.4 Comparison of the offshore AC active power for the three modes: solid Pole P, dashed Pole N (This figure has been reproduced with permission from Energynautics GmbH, 2024) 128
7.5 System values comparison case 3 and case 4 (a) Sum of Dissipated energy all WTGs of C4, (b) Exemplary DC-link voltageWTG at C4, (c) Active power C1 and C2 (This figure has been reproduced with permission from Energynautics GmbH, 2024) 129
7.6 System values (a) Sum of Dissipated energy all WTGs of C4, (b) DC-link voltage of a single WTG at C4, (c) AC current at C4-N, (d) Active power C1 and C2, (e) Onshore voltage C2 (This figure has been reproduced with permission from Energynautics GmbH, 2024) 130

A.1 Geometric design of the 320 kV DC cable [PRO16a] 177
A.2 Geometric design of the 525 kV DC cable [PRO16a] 178

A.3 Geometric design of the 66 kV AC cable [PRO16a] 179
A.4 Overview of the different cable aggregations [Kle24] 180

List of Tables

2.1 HBSM operational states 24

3.1 WTG parameters 43
3.2 HVDC system parameters 48

4.1 Start-up methods 54
4.2 Start-up methods 60
4.3 Pros and Cons of Soft and Hard Energization 76

6.1 Control combinations of the FRT scenarios 105
6.2 Protective blocking times of MMC 4 for DC-FRT 1.1,1.2,1.3,1.4111

7.1 Operational examples, Fault C2-N-C4-N (green onshore, blue offshore) 124

A.1 DC 320 kV cable parameters 177
A.2 DC 320 kV cable parameters 178
A.3 AC cable parameters 179
A.4 DC cable parameters 180
A.5 WTG GS control parameters 181
A.6 WTG MS control parameters 181
A.7 WTG machine control parameters 182
A.8 MMC control parameters 182
A.9 Three-winding transformer parameters 183
A.10 WTG transformer parameters 183
A.11 Onshore transformer and grid parameters 184

List of publications

Thesis relevant publications

1. **C. Klein**, P. Düllmann, A. Moser: "Post-Fault Power Flow Control for Multi-Terminal Bipolar HVDC Systems Connecting Offshore Wind Farms". In: *IEEE 7th Southern Power Electronics Conference (SPEC)*. 2022.
2. **C. Klein**, P. Düllmann, L. Osterkamp, N. Corte, et al.: "Black start of HVDC links via grid-forming wind turbines: sensitivity analysis and technical requirements". In: *22nd Wind and Solar Integration Workshop*. 2023.
3. **C. Klein**: *Abschlussbericht: HVDC BLADE, Demonstration der Schwarzstartfähigkeit von über HGÜ-angebundenen Offshore Windparks*. 2024.
4. **C. Klein**, P. Düllmann, W. Leterme: "Post-fault laod flow control through grid forming wind turbines connected to bipolar HVDC system with offshore AC-side pole coupling". In: *23rd Wind and Solar Integration Workshop*. 2024.
5. **C. Klein**, P. Düllmann, G. Love, V. Tackenberg, et al.: "Operating point dependent DC-FRT requirements in partially-selective MT-HVDC protection - North Sea Wind Power Hub pre-FEED study". In: *Cigre Symposium 2025, Trondheim, Norway*. 2025.
6. **C. Klein**, P. Düllmann, L. Osterkamp, N. Corte, et al.: "HVDC system energization via grid-forming offshore wind turbines: sensitivity analysis and technical requirements". In: *IET Renewable Power Generation* (2025).
7. **C. Klein**, M. Hagmans, W. Leterme: "Post DC-side fault system restoration via grid forming wind turbine generators". In: *Unpublished manuscript, submitted for publication at the time of thesis submission* (2025).

8. **C. Klein**, H. Thomas, M. Hagmans, W. Leterme: "Enabling Temporary Blocking of Offshore Converters through Grid-Forming Wind Turbines to Assist HVDC Grid Protection". In: *IET Generation, Transmission and Distribution* (2025).

Associated publications

1. P. Düllmann, P. Ruffing, C. Brantl, **C. Klein**, et al.: "Interoperability among dc protection strategies based on fault blocking converters and DC circuit breakers within a multi-terminal HVDC system". In: Institution of Engineering and Technology, 2020.
2. P. Düllmann, P. Ruffing, C. Brantl, **C. Klein**, et al.: "Interoperability among dc protection strategies based on fault blocking converters and DC circuit breakers within a multi-terminal HVDC system". In: *15th International Conference on Developments in Power System Protection (DPSP 2020)*. 2020.
3. P. Düllmann, C. Brantl, **C. Klein**, A. Moser: "Interdependencies in HVDC grid protection: Impact of converter parameters and controls on DC fault–ride–through capabilities and protection system design". In: *IET Generation, Transmission & Distribution* 17.10 (2023), pp. 2356–2375.
4. P. Düllmann, **C. Klein**, P. Winter, H. Köhler, et al.: "Preventive DC–side decoupling: A system integrity protection scheme to limit the impact of DC faults in offshore multi–terminal HVDC systems". In: *IET Generation, Transmission & Distribution* (2024).
5. G. Love, D. T. A. Kho, P. Düllmann, **C. Klein**: *Expandable & Compatible HVDC Grid Design*. 2025.

Curriculum Vitae

Christopher Klein

Ausbildung und akademischer Werdegang

07.2021–now	**Wissenschaftlicher Mitarbeiter**
	Institut für Elektrische Anlagen und Netze, Digitalisierung und Energiewirtschaft (IAEW)
	RWTH Aachen University, Deutschland
08.2020–07.2021	**Junior Electrical Engineer**
	Hardt Hyperloop
	Delft, Niederlande
03.2018–10.2020	**Master of Science**
	Elektrotechnik, Informationstechnik und Technische Informatik Studienschwerpunkt: Energietechnik
	RWTH Aachen University, Deutschland
10.2013–11.2017	**Bachelor of Science**
	Elektrotechnik, Informationstechnik und Technische Informatik Studienschwerpunkt: Energietechnik
	RWTH Aachen University, Deutschland
05.2004–05.2013	**Abitur**
	Kopernikus Gymnasium Niederkassel,
	Niederkassel, Deutschland

List of supervised theses

Master theses

- M. Hagmans: „Untersuchung der Inselnetzbildung von Offshore-Windparks bei temporärem Blockieren von MMCs nach HVDC-Fehlern “. 2024.
- P. Berghaus: „Untersuchung des FRT-Verhaltens von netzbildenden Windenergieanlagen für verschiedene Fehlerklärungsstrategien bei DC-Fehlern“. 2023.
- H. Wu: „Untersuchung der AC-Fault-Ride-Through Eigenschaften von netzbildenden Offshore Windparks angebunden über HGÜ-Systeme“. 2023.
- C. Yurt: „Modellierung und Analyse der Anbindung von netzbildenden Windenergieanlagen über bipolare HGÜ-Systeme “. 2022.

Bachelor theses

- A. Issa: „Schwarzstart eines bipolaren MT-HGÜ Systems durch netzbildende Offshore-Windparks“. 2025.
- C. Siebürger: „Implementierung und Analyse eines Testverfahrens für spannungseinprägende Umrichter von Windenergieanlagen und HGÜ-Systemen “. 2023.
- N. Corte: „Untersuchung des Energetisierungsprozesses von MMCs in HGÜ-Systemen zur Anbindung netzbildendender Offshore-Windparksg“. 2023.
- D. Magdinez: „Untersuchung der Stabilität von Offshore-Windparks für verschiedene Systemkonfigurationen“. 2023.
- M. Hagmans: „Untersuchung des Einflusses der Windenergieanlagen-regelung auf das Systemverhalten von Offshore-Windparks“. 2022.
- R. Kang: „Modellierung und Analyse netzbildend geregelter Windenergieanlagen“. 2022.

I would like to take this opportunity to express my sincere appreciation to all the students whose valuable contributions significantly supported the successful completion of this dissertation.

Appendix

A.1 DC cable

Figure A.1 shows the geometrical design for the 320 kV submarine cable and Figure A.2 the geometrical design for the 525 kV submarine cable. Both are modeled as frequency dependent phase models within EMT. The parameters are given in Table A.1 and Table A.2.

Table A.1: DC 320 kV cable parameters

Layer	**Radius [mm]**	$\boldsymbol{\rho}$ **[Ω*m*]**	$\boldsymbol{\epsilon_r}$	$\boldsymbol{\mu_r}$
Conductor r_1	25.1	$1.7 \cdot 10^{-8}$		1
Inner conduction layer	26.4			
Inner insulator r_2	47.1		2.5	1
Outer conduction layer	48.4			
Inner sheath r_3	50.1	$2.4 \cdot 10^{-7}$		1
Outer insulator r_4	54.1		2.3	1
Armour r_5	59.7	$1.38 \cdot 10^{-7}$		10
Outer sheath r_6	64.7		2.3	1

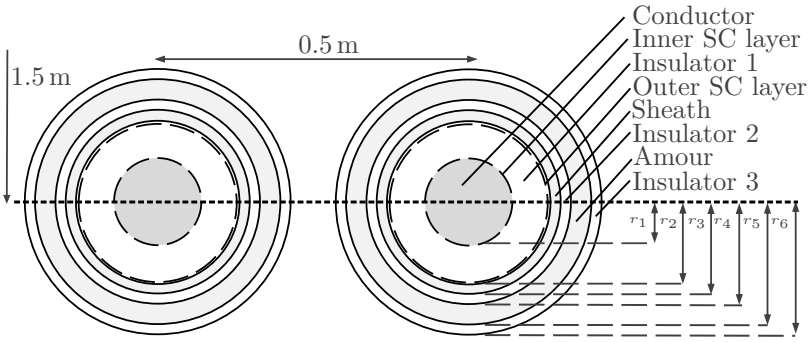


Figure A.1: Geometric design of the 320 kV DC cable [PRO16a]

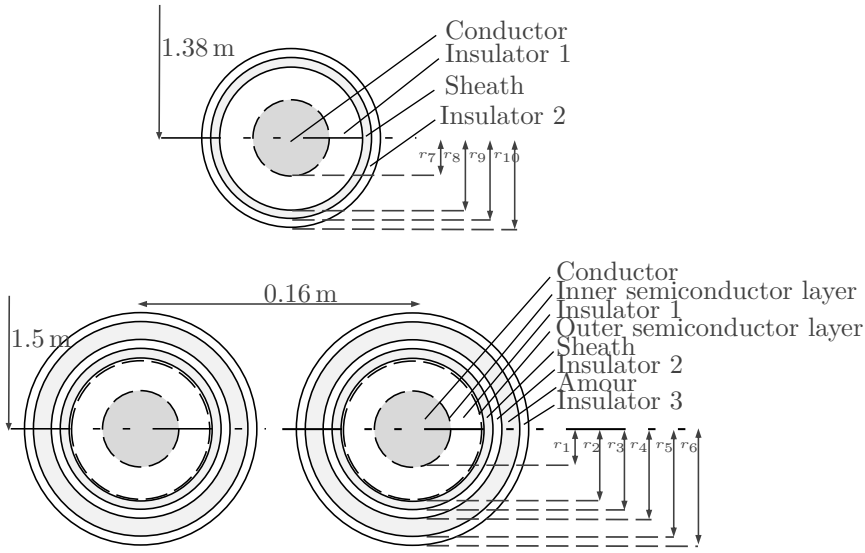


Figure A.2: Geometric design of the 525 kV DC cable [PRO16a]

Table A.2: DC 320 kV cable parameters

Layer	**Radius [mm]**	$\boldsymbol{\rho}$ **[Ω*m*]**	$\boldsymbol{\epsilon_r}$	$\boldsymbol{\mu_r}$
Conductor r_1	25.1	$1.7 \cdot 10^{-8}$		1
Inner conduction layer	26.4			
Inner insulator r_2	47.1		2.5	1
Outer conduction layer	48.4			
Inner sheath r_3	50.1	$2.4 \cdot 10^{-7}$		1
Outer insulator r_4	54.1		2.3	1
Armour r_5	59.7	$1.38 \cdot 10^{-7}$		10
Outer sheath r_6	64.7		2.3	1
Conductor DMR r_7	25.1	$1.7 \cdot 10^{-8}$		1
Inner insulator r_8	47.1		2.5	1
Sheath r_9	50.1	$2.4 \cdot 10^{-7}$		1
Outer insulator r_{10}	54.1		2.3	1

A.2 AC cable

The AC cable is a 66 kV AC cable also modeled as frequency dependent phase model, with the design shown in FigureA.3 and its parameters in Table A.3.

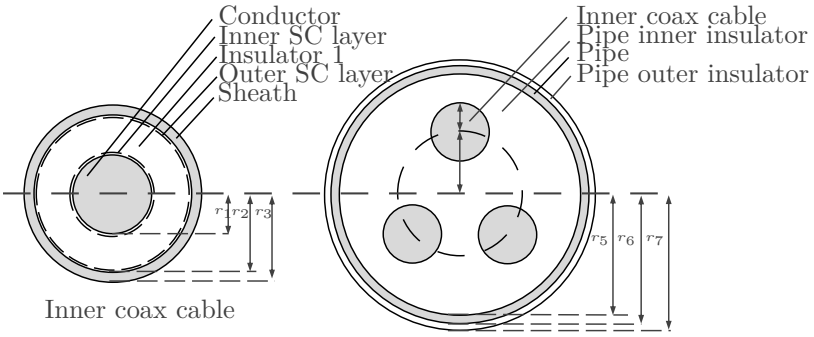


Figure A.3: Geometric design of the 66 kV AC cable [PRO16a]

Table A.3: AC cable parameters

Layer	**Radius [mm]**	$\boldsymbol{\rho}$ **[Ω*m*]**	$\boldsymbol{\epsilon_r}$	$\boldsymbol{\mu_r}$
Pipe inner insulator r_5	55.8		3	1
Pipe r_6	60.8	$13.8 \cdot 10^{-8}$		10
Pipe outer insulator r_7	64.0		2.3	1
Conductor r_1	10.05	$1.72 \cdot 10^{-8}$	1	1
Insulator 1 r_2	23.55		2.3	1
Sheath r_3	24.7	$17.2 \cdot 10^{-8}$		1

A.2.1 Cable aggregation

Compared to the aggregation with the 66 kV cable models, where for each WTG string the cables can be just run in parallel, for the PI-sections, the specific resistivity values have to be calculated. The modeling and parameters are shown in Figure A.4 and Table A.4 respectively.

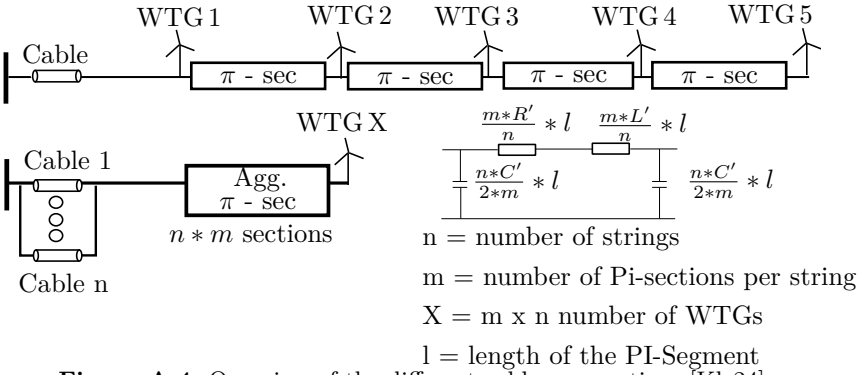


Figure A.4: Overview of the different cable aggregations [Kle24]

Table A.4: DC cable parameters

Parameter	**Value**
Resistance R'	$3.26 \times 10^{-5}\,\Omega/\mathrm{m}$
Inductive reactance X'_{L}	$9.1 \times 10^{-5}\,\Omega/\mathrm{m}$
Capacitive reactance X'_{C}	$7.73\,\mathrm{M}\Omega \cdot \mathrm{m}$

A.3 WTG control parameters

Corresponding to the control diagrams, the parameters for the GS and MS control are displayed in Table A.5,A.6 and A.7

Table A.5: WTG GS control parameters

Parameter	Symbol	Value
Inertia time constant	T_{J}	0.0025
Damping constant	K_{D}	1.25
Q/V droop constant	K_{Q}	0.03
Voltage control	$k_{\mathrm{v,i,GS}}/k_{\mathrm{v,p,GS}}$	1 / 10
Voltage limit	$V_{\mathrm{max,GS}}/V_{\mathrm{min,GS}}$	$\pm$ 1.1 p.u.
Current control	$k_{\mathrm{i,i,GS}}/k_{\mathrm{i,p,GS}}$	0.8 / 8
Current limit	$I_{\mathrm{max,GS}}/I_{\mathrm{min,GS}}$	$\pm$ 1.15 p.u.

Table A.6: WTG MS control parameters

Parameter	Symbol	Value
DC-link control	$k_{\mathrm{dc,p,MS}}/k_{\mathrm{dc,i,MS}}$	4 / 200
AC voltage control	$k_{\mathrm{Vac,i,MS}}/k_{\mathrm{Vac,p,MS}}$	2 / 40
AC voltage limits	$V_{\mathrm{max,MS}}/V_{\mathrm{min,MS}}$	$\pm$ 1.1 p.u.
Current controller	$k_{\mathrm{i,i,GS}}/k_{\mathrm{i,p,GS}}$	0.8 / 8
Current limits	$I_{\mathrm{max,MS}}/I_{\mathrm{min,MS}}$	$\pm$ 1.15 p.u.
PLL settings	$k_{\mathrm{PLL,p,MS}}/k_{\mathrm{PLL,i,MS}}$	100 / 100

Table A.7: WTG machine control parameters

Parameter	Symbol	Value
Pitch control	$k_{\text{pitch,i,MS}}/k_{\text{pitch,p,MS}}$	50 / 10
Pitch angle limits	Minimum/Maximum	0 / 27
Pitch angle change rate		10°/s
Rotational speed control	$k_{\omega,\text{p,MS}}/k_{\omega,\text{i,MS}}$	0.1 / 10

A.4 MMC control parameters

The control parameters corresponding to the MMC control diagram are displayed in Table A.8

Table A.8: MMC control parameters

Parameter	Symbol	Value
AC current	$k_{\text{iac,p}}$ / $k_{\text{iac,i}}$	0.756 / 4.917
CC current	$k_{\text{icc,p}}$ / $k_{\text{icc,i}}$	0.2616 / 0.5232
DC current	$k_{\text{idc,p}}$ / $k_{\text{idc,i}}$	0.335 / 0.139
DC voltage	$k_{\text{vdc,p}}$ / $k_{\text{vdc,i}}$	5.68 / 107.71
Total energy balancing AC	$k_{\text{ebac,p}}$ / $k_{\text{ebac,i}}$	4.89 / 189.43
Total energy balancing DC	$k_{\text{ebdc,p}}$ / $k_{\text{ebdc,i}}$	6.83 / 299.2
Active power control	$k_{\text{P,p}}$ / $k_{\text{P,i}}$	0.1564 / 139.6
Reactive power control	$k_{\text{Q,p}}$ / $k_{\text{Q,i}}$	0.4231 / 96.15
U/f droop control	k_{Uf}	0.05
AC current U/f control	$k_{\text{iac,uf,p}}$ / $k_{\text{iac,uf,i}}$	0.8 / 100
Phase-locked loop	$k_{\text{PLL,p}}$ / $k_{\text{PLL,i}}$	222 / 111

A.5 Transformer parameters

Table A.9: Three-winding transformer parameters

Parameter	Value
Leakage reactance	0.18
Copper losses	0.002 p.u.
Eddy current losses	0.0003 p.u.
Magnetizing current	0.06 %
Air core reactance	0.36 p.u.
Knee voltage	1.2 p.u.
Inrush decay time constant	1 s

Table A.10: WTG transformer parameters

Parameter	Value
Leakage reactance	0.1
Copper losses	0.0067 p.u.
Eddy current losses	0.00027 p.u.
Magnetizing current	0.5 %
Air core reactance	0.2 p.u.
Knee voltage	1.05 p.u.
Inrush decay time constant	0.2 s

A.6 Onshore grid parameters

The onshore grid uses two representations based on a Thevenin equivalent with respective impedance. Addionationally, a variable load can be supplied. The parameter can be found in Table A.11

Table A.11: Onshore transformer and grid parameters

Parameter	Symbol	Value
Weak grid impedance	$R_{\mathrm{i,weak}}/L_{\mathrm{i,weak}}$	$4.68\,\Omega$/ $44.02\,\Omega$
Strong grid impedance	$R_{\mathrm{i,weak}}/L_{\mathrm{i,weak}}$	$0.58\,\Omega$/ $5.28\,\Omega$
Variable load	R_{var}	0 MW - 1 GW